The QCD equation of state under extreme conditions

Ruben Nadir Kara

BERGISCHE
UNIVERSITÄT
WUPPERTAL

Bergische Universität Wuppertal
Fakultät für Mathematik und Naturwissenschaften

Dissertation
eingereicht zur Erlangung des akademischen Grades
Doktor der Naturwissenschaften (Dr. rer. nat.)

Juli 2024

Supervisor: Prof. Dr. Szabolcs Borsányi

Contents

1 Introduction

Phase transitions are key phenomena of our daily life, from the simple process of water boiling or condensation on windows to the formation of ice in a freezer. The corresponding release and absorption of heat associated with these 1^{st} order transitions is fundamental for today's technology such as heat pumps, air conditioners or fridges which are a kind of heat engine. Under specific conditions of temperature and pressure the clear distinction between liquid and vapor phases of a substance can disappear. This phenomenon is also observed in water at its critical point, which marks the end of the 1^{st} order transition line, where the release of latent heat vanishes. Beyond this critical point, only smooth transitions - the so-called crossovers - occur whose corresponding thermodynamic quantities are free of divergences and discontinuities. Crossover transitions can even be observed in everyday scenarios, such as the melting of butter at room temperature. Due to its complex composition of various fatty acids, butter does not have a single transition temperature but rather a range within it softens. Supercritical carbon dioxide, which exists above its critical temperature and pressure, provides a practical demonstration of these concepts in industrial applications. It shares properties of a gas and a liquid such as high density and low viscosity, qualifying it for chemical extraction processes as for example the decaffeination of coffee. Apart from these everyday and industrial scenarios, magnetic systems described by the Ising model feature critical phenomena driven by the spontaneous breaking of the underlying Z_2 symmetry. As the system is cooled from temperatures above the critical Curie temperature T_c to temperatures below T_c, the system undergoes a transition from a disordered to an ordered ferromagnetic state in which the spins spontaneously align along one direction.

Phase transitions are not limited to these daily and industrial settings but also occur under extreme conditions as were present in the early universe. Up to $\sim 10^{-12}$ s [1] after the Big Bang the electroweak interaction was a unified fundamental force [2–4] undergoing spontaneous symmetry breaking (SSB) as the universe expanded. Unlike real phase transitions with sharp transition temperatures, the change between the symmetric high temperature to the broken low temperature phase was an analytic crossover as confirmed by lattice simulations [5, 6]. During this process, the gauge bosons $W^{\pm}$ and Z as well as the quarks and leptons (except neutrinos according to the Standard Model) acquired their masses through the Higgs mechanism [7–9]. The density and temperatures were still too high for the existence of ordinary matter in form of hadrons such as protons and neutrons. Instead, the following epoch up to $\sim 10^{-5}$ s was dominated by the highly self-interacting quark gluon plasma (QGP), in which the fundamental constituents of matter - the quarks - can be delocalized and freely move. Their interactions are described by quantum chromodynamics (QCD) - the quantum field theory of the strong force. This theory features asymptotic freedom [10, 11], which leads to a decreasing strength of the interactions at high energies. This implies another cosmological transition from the QGP to the confinement of quarks into hadrons as the universe further expanded and cooled. Similarly to the electroweak transition, this shift was an

analytic crossover as confirmed by non-perturbative ab-initio lattice QCD simulations [12]. Such simulations at vanishing chemical potential reflect the conditions of the early universe, marked by a negligible asymmetry between matter and anti-matter [13]. In contrast to these high temperature environments, "cold" QGP phases might exist at low temperatures and high densities in astronomical dense objects such as the inner cores of neutron stars [14]. Gravitational wave astronomy offers a new possibility to study neutron stars and their mergers [15], providing a natural laboratory for exploring QCD at high densities. On Earth, measurements of the QGP have been performed for more than 20 years at LHC [16] and RHIC [17], probing the features of strongly interacting matter. Together with experiments at FAIR and NICA in the near future, they map out regions of the QCD phase diagram at high temperatures and moderate densities and potentially disclose the secret of the existence of a critical endpoint. I refer the reader to Section 2.6 for a detailed discussion of the phase diagram for QCD at finite density and temperature.
Phase transitions observed in various systems close to their critical points exhibit a universal behavior which is independent of the microscopic details of the system. Wilson's work on the renormalization group (RG) approach [18–20] explains the remarkable scale invariance of 2^{nd} order phase transitions by integrating out (thermal) fluctuations in sequence from small to larger scales. If the corresponding flow of the coupling constants reaches a (non-trivial) fixed point, the system became universal and can share the same critical exponents among its universality class [21]. The concept of renormalization is deeply embedded in quantum field theories as the Standard Model - the theory which covers all fundamental forces except gravity - is renormalizable [22]. Within this framework, the coupling constants, masses or charges show a strong dependence on the energy scale. As QCD is strongly coupled at low temperatures due to confinement, perturbative approaches cannot be applied. Lattice QCD provides a non-perturbative systematic improvable technique to solve QCD numerically.

In this thesis, we explore the parameter space of QCD in temperature, chemical potential and quark masses using lattice simulations. In Chapter 2 we discuss some thermal features of QCD and the contributions of the chiral and center symmetry to the structures of the phase diagram. Chapter 3 includes the concepts of finite temperature field theory and state-of-the-art lattice techniques for numerical simulations. In Chapter 4, we apply the parallel tempering algorithm to improve on (super-)critical slowing down associated with 1^{st} and 2^{nd} order phase transitions in the context of the Columbia plot. In Section 4.1, we calculate the transition temperature and latent heat with unreached high-precision in the continuum and infinite volume limit for quenched QCD and study its topological features in Section 4.2. In Section 4.3 we attempt to pin down the critical quark masses at which the latent heat vanishes and the transition is of 2^{nd} order.
In Chapter 5 we calculate the phenomenologically highly relevant equation of state (EoS) for physical quark masses at finite density with a novel expansion scheme. We introduce this method in Section 5.1 using a vanishing chemical potential for the strangeness and extend it to strangeness neutrality and beyond in Section 5.2.
In Chapter 6 we study finite volume effects of the chiral and deconfinement observables at vanishing and finite density.

Lattice QCD has been an established scientific field for almost 50 years and has lead to astonishing discoveries. Therefore, it is important to note that achieving such results as presented in this thesis is only possible within a smoothly running working group. Hence I briefly list my contributions to the projects of the Wuppertal-Budapest collaboration:

Deconfinement transition in quenched QCD
I implemented the multiple histogram method and extended it to the correlated case. Moreover, I performed the reweighting and fitting analysis in β (and θ) to calculate the critical coupling β_c at which the third Binder cumulant b_3 vanishes with the secant method. Furthermore, I calculated the latent heat by separating the configurations in hot and cold phases for which the trace anomaly is evaluated. For this purpose, I determined the minimum of the Polyakov loop potential by reweighting the histograms to β_c, which servers as a cut. I performed the multi dimensional global analysis of the curvature parameter R_θ to extract its continuum and infinite volume limit and to investigate the systematics. Additionally, I calculated the discontinuity of the topological susceptibility $\Delta\chi$ by assigning configurations to the confined and deconfined phase by the histogram method described above.

Determination of the critical mass
I generated configurations on JUWELS Booster at FZ Jülich using the parallel tempering version of the simulation code Janko. I performed the analysis of the Polyakov loop P and its susceptibility χ, determined the peak with high precision fits by expressing $\chi\left(\langle|P|\rangle\right)$ via splines and studied its volume and mass dependence. This enabled me to calculate the critical quark mass in the three flavor theory for temporal extension $N_t = 6, 8$ in the infinite volume limit. Furthermore I checked the latent heat as function of the quark masses and determined the critical exponents, which turned out to be less clean observables compared to the peak of the susceptibility given the current statistics.

Equation of state at finite density from an alternative expansion scheme
I performed the mock analysis which benchmarks various orders of the Taylor method for the EoS. Furthermore, I wrote programs for the 2d continuum extrapolation using basis splines in the low temperature region and high temperature region with polynomials in $1/T$. Based on these analyses, I calculated the thermodynamic quantities at finite density such as the pressure, entropy and energy density in the continuum for which numerical integration and derivatives were mandatory. I also wrote a program for the hadron resonance gas model for all needed thermodynamic quantities. All programs were adjusted for the finite strangeness part.

Finite volume effects
I performed the renormalization of the chiral and deconfinement observables and studied the volume dependence of the chiral transition temperature and its width defined by the peak of the susceptibility. Furthermore, I calculated the transition line of the chiral transition temperature at finite density using simulations at imaginary chemical potentials for various box sizes.

2 Quantum chromodynamics

In this Chapter I give a brief overview of QCD, the theory of strong interactions. The focus is set on the underlying symmetries and their features to highlight the motivation of our thermal studies. Hence, we discuss in detail the chiral and center symmetries, their corresponding explicit, spontaneous and anomalous breaking, some topological aspects and a historical outline of the Columbia plot.

2.1 Strong force

At the end of the 19^{th} and beginning of the 20^{th} century, physicists and chemists discovered the fundamental properties of matter. The gold foil experiment by Rutherford, Geiger and Marsden confirmed that atoms contain a positively charged nucleus carrying most of their masses. Together with the discovery of the neutron by Chadwick, it was clear that an atomic nucleus is not fundamental, but made of protons and neutrons, bound together by a "strong force". A successful attempt to describe the binding of protons and neutrons was made by Yukawa [23], who proposed a force carrier particle - the meson - which is exchanged in a nucleus. Further experimental progress led to the discovery of more and more particles, the particle zoo era, whose relation with each other was unclear. The quark model [24] organized these particles by suggesting fundamental constituents within these hadrons - the quarks. High energy experiments such as those performed at the Stanford Linear Accelerator Center or CERN confirmed this assumption by discovering the non-fundamental properties of protons and neutrons in deep inelastic scattering processes. Together with the indications of three color charges by measurements of e.g. Δ^-, Δ^{++}, Ω^- or the hadronic cross section of $e^+e^- \to$ hadrons, this paved the way for the modern formulation of the strong force: Quantum Chromodynamics.

2.2 Thermal features of QCD

In this Section I give a brief introduction to QCD and discuss its key features with the focus on its thermal properties. For further details I refer the reader to standard textbooks such as [25–28] from which I chose a small selection of topics.
QCD is a quantum field theory based on a non-abelian gauge symmetry $\mathrm{SU}(3)_c$. The corresponding Lagrange density (Lagrangian) reads

$$\mathcal{L} = \sum_f \bar{\psi}_f \left(i\gamma_\mu \partial^\mu + g\gamma_\mu T_a A^a_\mu - m_f \right) \psi_f - \frac{1}{4} F^a_{\mu\nu} F^{\mu\nu}_a \tag{2.1a}$$

$$:= \sum_f \bar{\psi}_f \left(i\not{D} - m_f \right) \psi_f - \frac{1}{4} \mathrm{tr}\, F_{\mu\nu} F^{\mu\nu} \tag{2.1b}$$

with the gluonic field strength tensor

$$F^a_{\mu\nu} = \partial_\mu A^a_\nu - \partial_\nu A^a_\mu + g f^{abc} A^b_\mu A^c_\nu. \tag{2.2}$$

The T_a are the eight Gell-Mann matrices representing the generators of SU(3) and f^{abc} are the corresponding structure constants. The sum over the Dirac spinors ψ_f stands for the summation over the quark flavors, which are color triplets equally treated in strong interactions with coupling strength g. It is worth to note that tr $F_{\mu\nu}F^{\mu\nu}$ results in a gluon self-interaction, caused by the non-abelian feature of $\mathrm{SU}(3)_c$.

Confinement and asymptotic freedom

Similar to quantum electrodynamics (QED), QCD is a theory which has to be renormalized to obtain physical results. This leads to parameters such as the coupling constant which depend on the energy scale. In contrast to QED, QCD does not feature a Landau pole in the high energy regime at which the coupling constant diverges. Instead it vanishes for diverging momenta $Q \to \infty$. This phenomenon is called asymptotic freedom and was discovered by Gross, Wilczek [10] and Politzer [11]. The running of the coupling constant α_s is shown in the following equation

$$\alpha_s(Q^2) = \frac{4\pi}{b_0 \log\left(Q^2/\lambda^2_{\mathrm{QCD}}\right)} \qquad b_0 = 11 - \frac{2}{3}N_f > 0, \tag{2.3}$$

with N_f the total number of flavors and $\lambda_{\mathrm{QCD}} \approx 200$ MeV confirmed by measurements [25] and. It can be understood as a scale at which perturbative QCD breaks down [29], implying that α_s takes on large values. Hence for high momenta or equivalent energy or temperature, the coupling decreases, in contrast to QED. This is a direct consequence of the gluon self-interaction which does not exist for the photons. In Fig. 2.1 the remarkable agreement between experimental (data points) and theoretical results (lines) is shown. Experimentally,

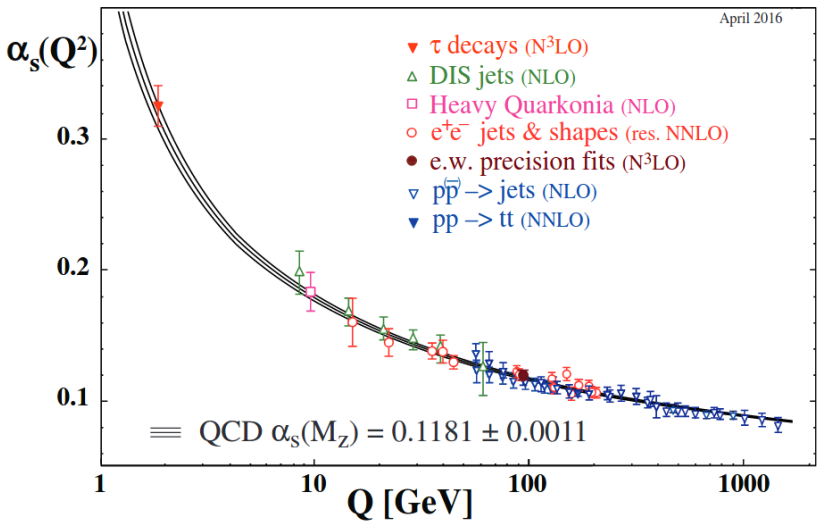

Figure 2.1: Strong coupling constant α_s as a function of the momenta transfer Q measured at different processes including its values at the Z boson mass [30].

it is well known that quarks are bound together and do not appear separately in the low

energy region in which they form color neutral states. This phenomenon is called confinement, whose strict analytic proof is still missing. Wilson gave an explanation of this mechanism by formulating (non-)abelian gauge theories on a discretised space time, laying the foundation of lattice field theory. By investigating the separation of a static quark anti-quark pair, he showed in the strong coupling limit (low energies) that large Wilson loops (phase factor appearing due to the interactions with gluon fields) are heavily suppressed [31]. In Chapter 4, we come back to this point and discuss the thermal properties of the Wilson loop in the form of the Polyakov loop in the heavy quark mass region.

Quark gluon plasma

The asymptotic freedom shows that for high temperatures quarks can liberate from their hadronic bound states due to the decrease of the coupling α_s. This is a hint for a new state of matter - the QGP in which the quarks can almost freely move. A first indication for such a state was found by Hagedorn in 1965 using the statistical bootstrap model [32], predicting an exponential increase of the number of resonances with the hadron mass. This leads to a maximum temperature $T_H \approx 150$ MeV at which the partition function diverges, clearly showing the limitations of the hadronic picture. This value agrees remarkably well with the pseudo-critical temperature $T_c = 158.0(6)$ MeV [33] calculated via lattice QCD based on chiral observables. Experimental studies of the QGP phase have been performed since approximately the beginning of the current century at LHC [16] and RHIC [17]. It turned out that the QGP is a highly interacting plasma whose chemical freeze-out temperature agrees with T_c provided by lattice QCD within errors [34]. Chemical freeze-out refers to the stage in which the composition of the system becomes fixed because inelastic scattering processes stop. Beyond this point, only particle decays and elastic scattering can take place. To clarify whether there is a real phase transition from the hadronic phase to the QGP, the underlying symmetry breaking or restoration pattern of QCD has to be studied.

2.3 Center symmetry

Dropping the fermionic part of QCD, we are left with a pure non-abelian SU(3) Yang-Mills theory. We call $m_q \to \infty$ the quenched limit, in which the creation of virtual quark anti-quarks is suppressed due to their infinite mass. In this case, the theory is symmetric under center transformations $\mathcal{Z}_3$ whose elements Z read

$$Z = z\,\mathbb{1} \qquad \text{with} \qquad z \in \{1, e^{\pm 2\pi i/3}\}. \tag{2.4}$$

To observe this, we start with a gauge transformation of A_μ

$$A_\mu(\tau, \vec{x}) \to \tilde{A}_\mu(\tau, \vec{x}) = g(\tau, \vec{x})\,(A_\mu(\tau, \vec{x}) + i\partial_\mu)\,g^\dagger(\tau, \vec{x}) \tag{2.5}$$

with $g \in \mathrm{SU}(3)$. Both obey periodic boundary conditions in time with periodicity $1/T$

$$A_\mu(\tau, \vec{x}) = A_\mu(\tau + 1/T, \vec{x}), \tag{2.6}$$
$$g(\tau, \vec{x}) = g(\tau + 1/T, \vec{x}). \tag{2.7}$$

As shown by t'Hooft [35, 36], there are also gauge transformations which are periodic up to a constant $h \in \mathrm{SU}(3)$ (twisted gauge transformations) [37]

$$g(\tau + 1/T, \vec{x}) = hg(\tau, \vec{x}). \tag{2.8}$$

Performing such a gauge transformation on $A_\mu(\tau + 1/T, \vec{x}) \to \tilde{A}_\mu(\tau + 1/T, \vec{x})$ leads to

$$\tilde{A}_\mu(\tau + 1/T, \vec{x}) = g(\tau + 1/T, \vec{x}) \left[A_\mu(\tau + 1/T, \vec{x}) + i\partial_\mu\right] g^\dagger(\tau + 1/T, \vec{x}) \tag{2.9a}$$

$$= hg(\tau, \vec{x}) \left[A_\mu(\tau, \vec{x}) + i\partial_\mu\right] g^\dagger(\tau, \vec{x}) h^\dagger \tag{2.9b}$$

$$= h\tilde{A}_\mu(\tau, \vec{x}) h^\dagger. \tag{2.9c}$$

Obeying the periodic boundary conditions of Eq. (2.6), $\tilde{A}_\mu(\tau + 1/T, \vec{x}) = \tilde{A}_\mu(\tau, \vec{x})$ implies

$$\tilde{A}_\mu(\tau, \vec{x}) = h\tilde{A}_\mu(\tau, \vec{x}) h^\dagger \qquad \Longrightarrow \qquad [h, \tilde{A}_\mu(\tau, \vec{x})] = 0, \tag{2.10}$$

restricting $h \in \mathcal{Z}_3$, the center of SU(3). From now on we call the center elements Z. Due to the anti-periodicity of fermionic fields, they transform under twisted gauge transformations according to

$$\psi(\tau + 1/T, \vec{x}) \to \tilde{\psi}(\tau + 1/T, \vec{x}) = g(\tau + 1/T, \vec{x}) \psi(\tau + 1/T, \vec{x}) \tag{2.11}$$

$$= -zg(\tau, \vec{x}) \psi(\tau, \vec{x}). \tag{2.12}$$

Since $z = 1$ to obey anti-periodic boundary conditions, $\mathcal{Z}_3$ is explicitly broken in the presence of fermionic fields.

Order parameter

The Polyakov loop

$$P(\tau, \vec{x}) = \text{tr}\, \mathcal{P} e^{i \int_0^{1/T} \mathrm{d}x_0 A_0(\vec{x}, x_0)}, \tag{2.13}$$

contains a path-ordered exponential, similar to the gauge transporter sharing the same transformation properties [38]:

$$\tilde{P}(\tau, \vec{x}) = \text{tr}\, g(1/T, \vec{x}) \mathcal{P} e^{i \int_0^{1/T} \mathrm{d}x_0 A_0(\vec{x}, x_0)} g^\dagger(0, \vec{x}) \tag{2.14a}$$

$$= \text{tr}\, Z\, g(0, \vec{x}) \mathcal{P} e^{i \int_0^{1/T} \mathrm{d}x_0 A_0(\vec{x}, x_0)} g^\dagger(0, \vec{x}) \tag{2.14b}$$

$$= zP(\tau, \vec{x}). \tag{2.14c}$$

Hence the Polyakov loop remains invariant if $z = 1$, implying that $\mathcal{Z}_3$ is spontaneously broken. McLerran and Svetitsky [39] related its expectation value to the free energy of a single quark F_q [37]

$$\langle P \rangle \sim e^{-F_q/T}, \tag{2.15}$$

and showing its sensitivity to deconfinement. If $\langle P \rangle = 0$ then $F_q \to \infty$, implying a confined phase in which an infinite amount of energy is needed to separate a quark from the system. In the presence of quarks, $\mathcal{Z}_3$ is explicitly broken and the Polyakov loop is no true order parameter anymore. However, it is still suitable to investigate the QCD crossover by its relation to F_q and hence to an entropy. We discuss this in Chapter 6. The spontaneous breaking of $\mathcal{Z}_3$ is associated with a non-vanishing expectation value of the Polyakov loop. In Fig. 2.2 the real and imaginary part of the Polyakov loop in the confined and deconfined phases are shown. Measurements of the Polyakov loop are populated around the center sectors in the deconfined phase.

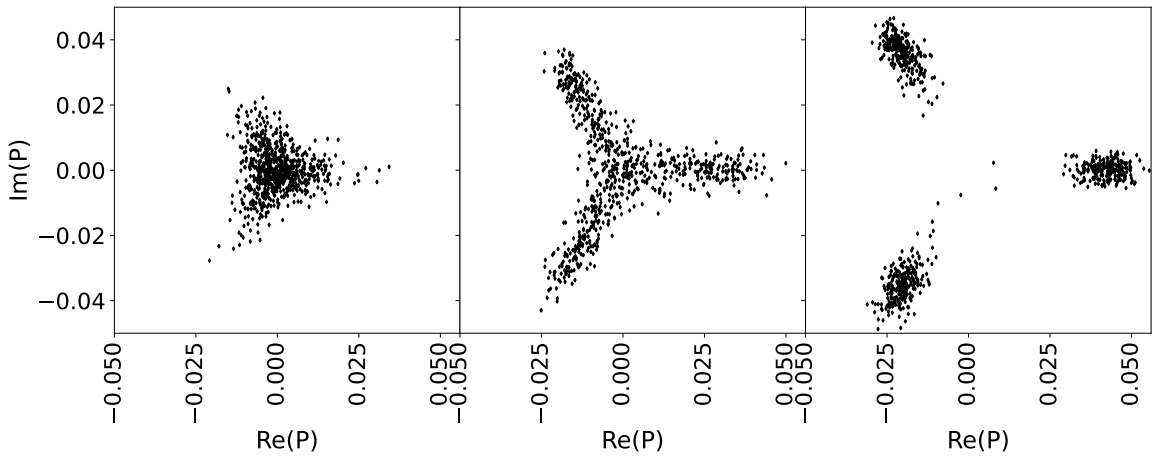

Figure 2.2: Real and imaginary part of the Polyakov loop in quenched QCD on $48^3 \times 12$ lattice. Lef: Confined phase. Middle: At the transition temperature. Right: Deconfined phase. Data from our study [40].

2.4 Chiral symmetry

Processes described by Newton's laws or electromagnetism are invariant under parity transformations since the underlying equations have mirror symmetry. Is this a true symmetry in Nature implying that a mirror-inverted world just shows mirrored processes? The answer is a clear no. The famous Wu-experiment [41] demonstrates that in weak interactions the W bosons prefer to couple to left handed particles or right handed anti-particles indicating parity is not conserved. The handedness of a particle should be distinguished in the concepts of helicity or chirality. They coincide for massless particles but only chirality is Lorentz invariant. In the following we set the focus on the latter which plays a key role for the generation of the hadron masses. Eigenstates of γ_5 with eigenvalue $+1$ are called right-handed and those with -1 left handed eigenstates. Defining the operators

$$P_R := \frac{1+\gamma_5}{2} = P_R^\dagger, \qquad P_L := \frac{1-\gamma_5}{2} = P_L^\dagger, \tag{2.16}$$

it is possible to project a quark field ψ onto its right and left handed components

$$\psi_L = P_L\psi \qquad \psi_R = P_R\psi \tag{2.17}$$

$$\bar{\psi}_L = \bar{\psi}P_R \qquad \bar{\psi}_R = \bar{\psi}P_L. \tag{2.18}$$

Parity transformations P can change the chirality of a quark field as exemplarily demonstrated for a right handed state. It transforms according to

$$\psi_R(t,\vec{x}) \xrightarrow{P} \gamma_0\psi_R(t,-\vec{x}). \tag{2.19}$$

We can check its chirality by

$$\gamma_5\gamma_0\psi_R(t,-\vec{x}) = -\gamma_0\gamma_5\psi_R(t,-\vec{x}) = -\gamma_0\psi_R(t,-\vec{x}), \tag{2.20}$$

showing that it remains an eigenstate of γ_5 but with eigenvalue -1 indicating a left handed state. In the chiral limit the fermionic part of the QCD Lagrangian reads

$$\mathcal{L}_{F,m_f\to 0} = \bar{u}_L i\not{D} u_L + \bar{u}_R i\not{D} u_R + \bar{d}_L i\not{D} d_L + \bar{d}_R i\not{D} d_R + \bar{s}_L i\not{D} s_L + \bar{s}_R i\not{D} s_R \tag{2.21a}$$

$$= \sum_f \bar{\psi}_{f,L} i\not{D} \psi_{f,L} \tag{2.21b}$$

$$:= \bar{q}_L i\not{D} q_L + \bar{q}_R i\not{D} q_R \tag{2.21c}$$

with

$$q = \begin{pmatrix} u \\ d \\ (s) \end{pmatrix}. \tag{2.22}$$

In the following we will take a closer look at a two flavor theory consisting of up and down quarks and a three flavor theory with an additional strange quark s.
Obviously Eq. (2.21c) is invariant under unitary transformations acting on the left and right handed parts separately $\mathrm{U}(N_f)_L\times\ \mathrm{U}(N_f)_R$

$$q_L \to \mathrm{U}_L q_L \qquad \bar{q}_L \to \bar{q}_L \mathrm{U}_L^\dagger \tag{2.23}$$

$$q_R \to \mathrm{U}_R q_R \qquad \bar{q}_R \to \bar{q}_R \mathrm{U}_R^\dagger. \tag{2.24}$$

The symmetry can be split as $\mathrm{U}(N_f)_L\times\ \mathrm{U}(N_f)_R = \mathrm{SU}(N_f)_L\times\ \mathrm{SU}(N_F)_R\times\ \mathrm{U}(1)_A\times\ \mathrm{U}(1)_V$ and is called chiral or flavor symmetry [38]. It is explicitly broken by finite quark masses:

$$\mathcal{L}_{\text{mass}} = \bar{q} \begin{pmatrix} m_u & 0 & 0 \\ 0 & m_d & 0 \\ 0 & 0 & m_s \end{pmatrix} q \tag{2.25a}$$

$$= \bar{q}_R \mathbf{m} q_L + \bar{q}_L \mathbf{m} q_R + \underbrace{\bar{q}_L \mathbf{m} q_L}_{=0} + \underbrace{\bar{q}_R \mathbf{m} q_R}_{=0}. \tag{2.25b}$$

The last two terms vanish according to Eqs. (2.17) and (2.18) since the product of the left and right handed projectors is zero $P_R \cdot P_L = 0 = P_L \cdot P_R$. The first two terms indicate that left and right handed parts are mixed which obviously breaks chiral symmetry. But what happens in the chiral limit, which should be close to the physical point since the light quark masses are small compared to the QCD scale? Is QCD actually invariant under these transformations or is there a spontaneous breaking or any anomalies present?

$\mathrm{U}(1)_V$ transformations

The $\mathrm{U}(1)_V$ is a global symmetry whose transformations are

$$q \to e^{i\alpha} q, \qquad \bar{q} \to \bar{q} e^{-i\alpha}, \tag{2.26}$$

with the rotation angle $\alpha \in \mathbb{R}$ and the corresponding Noether current

$$J^\mu = \bar{q}\gamma^\mu q. \tag{2.27}$$

This is a true symmetry in QCD leading to a conservation of the baryon number

$$B = \frac{1}{3}\int \mathrm{d}^3x J^0(x) = \frac{1}{3}\int \mathrm{d}^3x \bar{q}(x)\gamma^0 q(x) = \frac{1}{3}\int \mathrm{d}^3x \left(q_L^\dagger(x) q_L(x) + q_R^\dagger(x) q_R(x)\right). \tag{2.28}$$

It is important to note that $\mathrm{U}(1)_V$ is not necessarily a symmetry of Nature, due to the significant imbalance of matter and anti-matter in the observable universe.

$\mathbf{SU}(N_f)_L \times \mathbf{SU}(N_f)_R$ transformations

Transforming the left and right handed parts of the quark field q separately, the transformations read

$$q_{R/L} \to e^{i\vec{\alpha}_{R/L}\vec{\tau}} q_{R/L}, \qquad \bar{q}_{R/L} \to \bar{q}_{R/L} e^{-i\vec{\alpha}_{R/L}\vec{\tau}}, \tag{2.29}$$

leading to the Noether current

$$J^a_{\mu,R/L} = \bar{q}_{R/L}\gamma_\mu \tau^a q_{R/L}. \tag{2.30}$$

Depending on the number of flavors, $\vec{\tau}$ corresponds to the Pauli matrices $\vec{\sigma}$ or the Gell-Mann matrices $\vec{\lambda}$

$$\vec{\tau} = \begin{cases} \vec{\sigma}/2 & N_f = 2, \\ \vec{\lambda}/2 & N_f = 3. \end{cases} \tag{2.31}$$

With Eq. (2.30) we can define a vector and an axial current [42]

$$V^a_\mu = J^a_{\mu,R} + J^a_{\mu,L} = \bar{q}\gamma_\mu \tau^a q, \qquad A^a_\mu = J^a_{\mu,R} - J^a_{\mu,L} = \bar{q}\gamma_\mu\gamma_5 \tau^a q, \tag{2.32}$$

and rewrite the transformation as $\mathrm{SU}(N_f)_V \times \mathrm{SU}(N_f)_A$.

$\mathbf{SU}(N_f)_V$ transformations

The $\mathrm{SU}(N_f)_V$ vector transformations rotate the left and right handed parts of the quark fields with the same angle $\vec{\alpha}$

$$q \to e^{i\vec{\alpha}\vec{\tau}} q, \qquad \bar{q} \to \bar{q} e^{-i\vec{\alpha}\vec{\tau}}, \tag{2.33}$$

leading to the vector current V^a_μ of Eq. (2.32). For physical quark masses it is an approximate symmetry arranging for instance the mesons in an octet representation (eightfold way) [43, 44]. In the chiral limit Vafa and Witten [45] showed that the vacuum is invariant under $\mathrm{SU}(N_f)_V$ rotations implying the absence of a spontaneous breaking. In the case of $N_f = 2$ the transformation mentioned in Eq. (2.33) can be understood as an isospin rotation:

$$\pi^a : \; i\bar{q}\sigma^a\gamma_5 q, \qquad \vec{\pi} \to \vec{\pi} + \vec{\alpha} \times \vec{\pi}. \tag{2.34}$$

The transformation of a π-like state corresponds to a rotation of the underlying isospin which explains the approximate mass degeneracy of the isopsin triplet of the π [46].

$\mathbf{SU}(N_f)_A$ transformations

The quark fields transform under $\mathrm{SU}(N_f)_A$ as

$$q \to e^{i\vec{\alpha}\vec{\tau}\gamma_5} q, \qquad \bar{q} \to \bar{q} e^{i\vec{\alpha}\vec{\tau}\gamma_5}, \tag{2.35}$$

since $\{\gamma_\mu, \gamma_5\} = 0$, leading to the axial current A^a_μ of Eq. (2.32). The vector mesons

$$\vec{a}_{1\mu} : \bar{q}\ \vec{\sigma}\gamma_\mu\gamma_5\ q, \qquad \vec{\rho}_\mu : \bar{q}\ \vec{\sigma}\gamma_\mu\ q, \tag{2.36}$$

can be related to each other by axial transformations Eq. (2.35)

$$\vec{\rho}_\mu \to \vec{\rho}_\mu + \vec{\alpha} \times \vec{a}_{1\mu}, \tag{2.37}$$

$$\vec{a}_{1\mu} \to \vec{a}_{1\mu} + \vec{\alpha} \times \vec{\rho}_\mu, \tag{2.38}$$

implying that their mass should be nearly identical [46]. However, the measurements of the masses yield $m_\rho = 770$ MeV and $m_{a_1} = 1260$ MeV. The following questions arise: Where does the mass difference of these mesons come from? Is the main driver the explicit symmetry breaking due to finite quark masses in Nature? It can be shown that this symmetry is just slightly broken by physical quark masses implying that the axial current is almost conserved, also known as Partially Conserved Axial Current (PCAC) [47]

$$\langle 0| \partial^\mu A^a_\mu |\pi^b\rangle = -f_\pi m_\pi^2 \delta^{a,b} e^{-iqx}. \tag{2.39}$$

So the divergence of the axial current depends on the pion decay constant f_π and the pion mass m_π. According to the Gell-Mann-Oakes-Renner relation, the latter can be related to the light quark mass [25, 48]

$$m_\pi^2 \sim \frac{m_u + m_d}{f_\pi^2}. \tag{2.40}$$

Hence, pions are massless in the chiral limit and can be identified as the Goldstone bosons due to the spontaneous breaking of chiral symmetry. Their small masses compared to other hadrons arise from the explicit breaking caused by the finite light quark masses.
To summarize: The significant mass difference of the $\vec{\rho}$ and $\vec{a}_1$ cannot be understood by the explicit symmetry breaking. Instead it must come from the spontaneous symmetry breaking [46, 49].

$\mathbf{U(1)_A}$ transformations

If $\mathrm{U}(1)_A$ were actually realized in Nature, we should expect a parity doubling of the baryons [26]. This is not the case and hence one could assume that this symmetry is also spontaneously broken, leading to another Goldstone boson similar to the case described in the previous paragraph. Restricting this short discussion to $N_f = 2$, the associated Goldstone boson should have a similar mass as the π. The possible candidate η is too heavy and its mass can be well understood by the explicit breaking of $\mathrm{SU}(3)_A$. It turns out that $\mathrm{U}(1)_A$ is broken by a so-called anomaly, which is another type of symmetry breaking. This gave rise to important discoveries regarding instantons, insights on the structure of the QCD vacuum and the η' mass. The following discussion is based on [42, 50, 51] to illustrate what Callan, Dashen and Gross could mean by suggesting instantons as a driver of chiral symmetry breaking [52]. Under $\mathrm{U}(1)_A$ the quark fields transform according to

$$q \to e^{-i\gamma_5\alpha} q, \qquad \bar{q} \to \bar{q} e^{-i\gamma_5\alpha}, \tag{2.41}$$

with the Noether current

$$J_5^\mu = \bar{q}\gamma^\mu\gamma_5 q. \tag{2.42}$$

This current is conserved classically, but not on a quantum level. In the context of QED, Adler [53], Bell and Jackiw [54] calculated the corrections to J_5^μ perturbatively to understand the neutral pion decay into two photons $\pi^0 \to 2\gamma$. This process should be suppressed as proposed by Veltman [55] and Sutherland [56] using current algebra methods. As demonstrated by Fujikawa [57] the measure of the path integral changes under Eq. (2.41), leading to a non vanishing divergence of the axial current which can be written in the chiral limit as [50]

$$\partial_\mu J_5^\mu = -N_f \frac{g^2}{16\pi^2} \mathrm{tr} F^{\mu\nu} \tilde{F}_{\mu\nu}. \tag{2.43}$$

Integrating this equation gives a non zero value since surface terms are relevant in QCD through its topological distinct vacua which are specified by instantons. In other words, the

QCD vacuum state is not unique, instead it is a superposition of vacua due to the periodicity of the gluonic potential. This has to be taken into account in our analysis of the ground state since tunnel processes between these states could lower its energy. How can we distinguish vacuum states for a given gluonic configuration? They are specified by the axial charge, whose change can be calculated by integrating Eq. (2.43) over the full spacetime:

$$Q_5(t \to +\infty) - Q_5(t \to -\infty) = \Delta Q_5 = -\int \mathrm{d}x^4 N_f \frac{g^2}{16\pi^2} \mathrm{tr} F^{\mu\nu} \tilde{F}_{\mu\nu} := 2N_f Q_t. \tag{2.44}$$

Q_t is called topological charge and has a direct connection to the zero modes of the Dirac operator, a special case of the Atiyah-Singer index theorem. To illustrate this, we start with the following eigenstates of the Dirac operator

$$i\not{D}\psi_\lambda = \lambda\psi_\lambda, \qquad i\not{D}\gamma_5\psi_\lambda = -\lambda\gamma_5\psi_\lambda, \tag{2.45}$$

implying that these states are orthogonal if $\lambda \neq 0$. With Eq. (2.42) they can be used to rewrite the change of the axial charge to [51, 58]

$$\begin{aligned}
\Delta Q_5 &= \int \mathrm{d}x^4 \partial_\mu \langle J_5^\mu \rangle && \text{(2.46a)}\\
&= N_f \int \mathrm{d}x^4 \partial_\mu \mathrm{tr}\left[S(x,x)\gamma_\mu\gamma_5\right] && \text{(2.46b)}\\
&= N_f \int \mathrm{d}x^4 \partial_\mu \mathrm{tr}\left[\sum_\lambda \frac{\psi_\lambda \psi_\lambda^\dagger}{\lambda}\gamma^\mu\gamma_5\right] && \text{(2.46c)}\\
&= N_f \int \mathrm{d}x^4 \mathrm{tr}\left[\sum_\lambda \frac{\psi_\lambda \psi_\lambda^\dagger}{\lambda} 2\lambda\gamma_5\right] && \text{(2.46d)}\\
&= N_f \int \mathrm{d}x^4\ 2\ \mathrm{tr}\left[\ \psi_0\psi_0^\dagger\gamma_5\right]. && \text{(2.46e)}
\end{aligned}$$

First, the expectation value of the axial current for a given gauge configuration can be related to the Dirac propagator $S(x,x)$. Then it is expressed in the spectral representation in terms of its eigenfunctions. Due to the orthogonality shown in Eq. (2.45), only zero modes have a non zero contribution leading to

$$\Delta Q_5 = 2N_f(n_L - n_R) \qquad \Longrightarrow \qquad Q_t = n_L - n_R, \tag{2.47}$$

with n_L as the number of left handed and n_R of right handed zero modes. Zero modes play a crucial role since they are related to the chiral condensate according to the Banks-Casher relation [59]

$$\langle \bar{q}q \rangle \sim \rho(\lambda \to 0). \tag{2.48}$$

Here $\rho(\lambda)$ is the spectral density of the Dirac operator. To summarize: Since $\mathrm{U}(1)_A$ is broken (anomalously), there is a non vanishing expectation value of the chiral condensate which breaks chiral symmetry [58]. It is worth to note that the anomalous breaking of $\mathrm{U}(1)_A$ clarifies why the η' meson does not belong to the octet representation of mesons in $N_f = 3$. It consists of u, d, s quarks, but is roughly 60% heavier than its isosinglet partner η. The Witten-Veneziano equation [60, 61]

$$\chi_t^q := \frac{\langle Q^2 \rangle}{\mathcal{V}} = \frac{f_\pi^2}{2N_f}\left(m_\eta^2 + m_{\eta'}^2 - 2m_K^2\right), \tag{2.49}$$

$$\chi_t^q \overset{m_q \to 0}{=} \frac{f_\pi^2}{2N_f} m_{\eta'}^2, \tag{2.50}$$

with $\mathcal{V}$ indicating the space-time volume, relates the topological susceptibility of quenched QCD χ_t^q to the masses of the η, η' and the K. Eq. (2.50) results from the chiral limit which makes the η and K massless. Both equations highlight that the η' is not related to the meson octet and hence $\mathrm{SU}(3)_A$ is spontaneously broken and not a unitary symmetry which should lead to nine Goldstone bosons instead.
It is important to note that the topological charge contains $\mathrm{tr}F^{\mu\nu}\tilde{F}_{\mu\nu}$, which is a pseudoscalar not invariant under CP transformations. Since there is no reason why (massive) QCD should obey CP symmetry, a term of the form

$$\mathcal{L}_\theta \sim \theta \ \mathrm{tr}F^{\mu\nu}\tilde{F}_{\mu\nu}, \tag{2.51}$$

can be added to the Lagrangian. The present experimental status of the measurement of the neutron electric dipole moment sets an upper limit for $\theta < 10^{-9}$ [62]. Since $\theta \in [0, 2\pi)$, the question arises why θ is so small. This is known as the strong CP problem. In Section 4.2 we study the topological features of quenched QCD and investigate the impact of a CP breaking θ term on the deconfinement transition.

Order parameter

The order parameter to investigate chiral symmetry breaking is the chiral condensate

$$\langle \bar{q}q \rangle = \langle \bar{q}_R q_L + \bar{q}_L q_R \rangle \, . \tag{2.52}$$

In the chiral broken phase it takes on a non-vanishing expectation value induced by the spontaneous and explicit chiral symmetry breaking and by the anomalous $\mathrm{U}(1)_A$ breaking. Recent lattice studies such as [63, 64] try to quantify the contribution of the latter to the chiral observables. A key challenge is the proper implementation of chiral symemtry on the lattice for which staggered fermions seem to be less appropriate causing large cut-off effects compared to Möbius domain-wall fermions (see Appendix of [63]). The effect of the possible $\mathrm{U}(1)_A$ restauration could give insights to the Columbia plot, which is discussed in the next chapter.

2.5 Phase diagram in the mass plane

In the last Sections we discussed the explicit, spontaneous and anomalous breaking of chiral symmetry and the features of center symmetry breaking related to deconfinement. Both are explicitly broken by finite quark masses, which work as symmetry breaking variables in analogy to an external magnetic field in the case of spin models. Depending on their exact values, the order of the thermal transition can change. First attempts to classify the corresponding phase diagram as a function of the quark masses were performed on coarse lattices by the Columbia group [65]. Hence this phase diagram is often referred as Columbia plot in the literature and is still under investigation due to the enormous computational challenges it provides.

2.5.1 Upper right corner of the Columbia plot

For infinite quark masses, QCD is reduced to a pure gauge theory. In the strong coupling limit, early studies showed the equivalence of the pure SU(3) gauge theory to 3d spin systems which are also invariant under Z(3) transformations [66–68]. Mean-field analysis and the absence of renormalization group fixed points indicate that such systems feature 1^{st} order

phase transitions [68, 69]. These are strong arguments for a 1st order phase transition in SU(3) gauge theories, but no strict proofs. Early lattice studies such as [70, 71] supported these assumptions by observing hysteresis of the order parameter. Interestingly, Ref. [72] showed an increasing correlation length with the volume which is a typical sign of 2nd order phase transition. However, finer lattices and larger volumes confirm a weak 1st order nature accompanied by a high correlation length [73,74]. A key feature of a 1st order phase transition is a non-vanishing latent heat. Similar to the work of the WHOT collaboration [75, 76] we could calculate the latent heat in the continuum and thermodynamic limit, and found small values highlighting the weak 1st order nature in the context of SU(N) theories [77].
Finite quark masses explicitly break the global Z(3) symmetry and weaken the transition until the latent heat vanishes at the critical quark masses. These are endpoints of the 1st order phase transition and should be in the same universality class as the 3d Ising model or Z(2) spin systems sharing the same critical exponents [78]. This assumption is supported by [79], in which the authors demonstrate that the Z(3) symmetric 3d three state Potts model with an external ordering field and the 3d Ising model are in the same universality class. Various techniques based on matrix models [80], Dyson-Schwinger methods [81], lattice results by reweighting from quenched QCD [82], hopping parameter expansion [83,84] or using the parallel tempering algorithm [85] have been used to study criticality in the heavy mass region. Severe cut-off effects [84] and critical slowing down pose a numerical challenge, making these investigations computationally expensive. So far a continuum limit of the critical quark masses is missing, but there is a good agreement between the aforementioned studies.

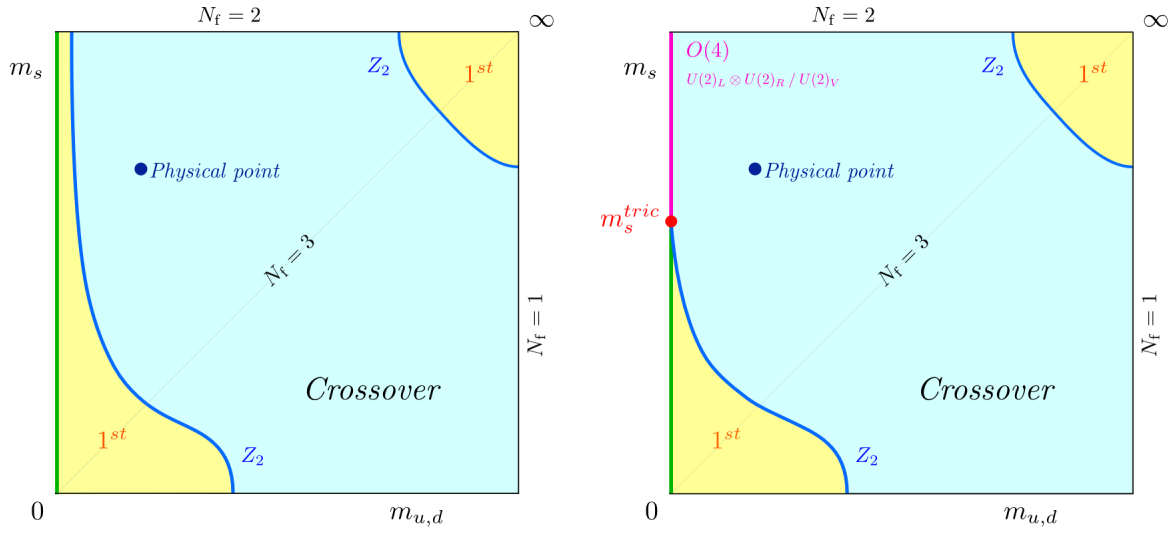

Figure 2.3: Possible phase diagrams of QCD at $\mu_B = 0$ depending on the degenerate light quark mass $m_{u,d}$ and the strange quark mass m_s. Plots from [86].

2.5.2 Left side of the Columbia plot

The linear σ-model is an effective scalar field theory for QCD at low energy describing interactions of pions and scalar mesons. Depending on the exact definition it includes complex scalar fields coupled by quartic interactions and resulting massless π and massive σ fields due to the spontaneous chiral symmetry breaking. Originally proposed by Schwinger [87] and used by Gell-Mann and Levy [88] for nucleon-π interactions, Pisarski and Wilczek applied the most general renormalizable formulation of the linear σ-model to investigate the order

of the thermal phase transition by fixed point analyses [89]. Therefore, the β functions in $4-\epsilon$ dimensions which specify the coupling parameters on an energy scale, are expanded in leading order in ϵ. For $N_f = 3$ in the chiral limit the transition should be of 1^{st} order due to the absence of an infrared stable fixed point. It is important to note that this statement is true for $\epsilon \ll 1$ which is clearly not the case since $\epsilon = 1$ to match a 3d theory. Nevertheless this strategy led to successful predictions of the type of antiferromagnetic phase transition for e.g. Cr and Eu [90]. On the other hand, a recent study [91] based on functional renormalization group (FRG) flow analysis favors a 2^{nd} order phase transition.
The possible restoration of $\mathrm{U}(1)_A$ could have a crucial impact on the phase transition, especially in the case of $N_f = 2$. Here we distinguish the two cases: 1) $\mathrm{U}(1)_A$ is broken (right panel of Fig. 2.3) and 2) $\mathrm{U}(1)_A$ is restored at the chiral restoration temperature $T \approx T_\chi$ (left panel). The order parameter of the chiral symmetry breaking is the chiral condensate which is symmetric under $\mathrm{U}(2)_L \times \mathrm{U}(2)_R$ transformations. In the 1) case, $\mathrm{U}(1)_A$ can be removed by restricting the transformations to $\mathrm{SU}(2)_L \times \mathrm{SU}(2)_R$, which are locally isomorphic to O(4) [92]. Therefore a 2^{nd} order phase transition with O(4) critical exponents is expected or at least possible [92–94].
In the 2) case, $\mathrm{U}(1)_A$ is "effectively" restored. Since it is always broken by the anomaly, it can be only "effectively" restored implying that instantons are suppressed making the η' light. A restoration of $\mathrm{U}(1)_A$ extends the chiral symmetry which could lead to a 1^{st} order phase transition [89]. Similar to the heavy quark case mentioned in the previous section, the 1^{st} order region should be surrounded by Z(2) critical lines [78]. On the other hand, a high-order field-theoretical perturbative study [95] indicates a 2^{nd} order phase transition but not in the O(4) universality class, whereas a FRG study [96] suggests O(4) critical exponents [97]. To summarize, the order of the phase transition for $N_f = 2, 3$ in the chiral limit is still unclear and first principle methods such as lattice QCD are needed to explore its nature.
Direct lattice QCD simulations for vanishing quark masses are hindered due to the appearance of zero eigenvalues which make the inversion of the fermion matrix impossible. Hence a suitable strategy is to simulate at small quark masses and then extrapolating to the chiral limit. Early studies on $N_t = 4$ such as [98, 99] using unimproved staggered and Wilson fermions predict a 1^{st} phase transition for $N_f = 3$. These findings are supported by [100] where improved Wilson fermions and $N_t = 6, 8$ are used and the critical endpoint is determined. A more recent study by the hotQCD collaboration using the HISQ action on $N_t = 6$ lattices does not detect a 1^{st} order region and estimates an upper bound for the pseudoscalar critical mass $m_{\text{PS}} \lesssim 50$ MeV [101].
Similar statements can be drawn for $N_f = 2$, where unimproved staggered such as [102] or Wilson studies [103] see hints for a 1^{st} phase transition and differ for m_{PS}^c by a factor of 10. It is obvious that for $N_f = 2, 3$ cut-off effects are large and distort the picture of the possible phase transitions.
Another approach is to simulate a 2+1 flavor theory as done by hotQCD [104] with a physical strange quark mass and then extrapolate to $m_l \to 0$ using the scaling relations for e.g. the temperature [97]

$$T_c(m_l, m_s) = T_c(0, m_s) + A(m_s) m_l^{1/\beta\delta} \qquad T_c(0, m_s^{\text{phys}}) = 132^{+3}_{-6}\ \text{MeV}. \tag{2.53}$$

As mentioned above, the possible critical scaling is unclear and the corresponding exponents in the case of O(4), O(2) or Z_2 are very close to each other. Hence the authors of [104] investigated the systematics by swapping continuum or chiral limits and using different critical exponents and linear extrapolations for the infinite volume limit.
Let us assume that $\mathrm{U}(1)_A$ remains broken and we face the scenario shown on the right panel

of Fig. 2.3. If the order of the phase transition changes from 2nd for $N_f = 2$ to 1st order for $N_f = 3$ (surrounded by Z_2 critical lines), then there must exist a tricritical strange quark mass m_s^{tric} at which the 1st order and the 2nd order curves intersect. If $m_s < m_s^{\text{tric}}$ then we face 1st order phase transition in the chiral limit. This scenario can be translated in the same manner to $2 < N_f^{\text{tric}} < 3$. Furthermore there is a three state coexistence at T_c, with $\langle\bar{\psi}\psi\rangle = 0$ and $\pm\langle\bar{\psi}\psi\rangle \neq 0$. The latter arises from the possible transformation $m_l \to -m_l$ due to the symmetry of the Columbia plot which causes a sign flip of the condensate [86].
The situation is similar for the left panel of Fig. 2.3 for which $\mathrm{U}(1)_A$ is restored. Due to the absence of a chiral transition for $N_f = 1$ and a 1st order phase transition for $N_f = 2$, a tricritical number of flavors has to exist $1 < N_f^{\text{tric}} < 2$ [86].
Looking for tricritical scaling windows is a promising strategy because the tricritical exponents are known and do not need to be determined. So far the accuracy is not sufficient to distinguish the possible scenarios of Fig. 2.3 [97]. There is no need to restrict the search for tricritical scaling on the quark masses. Instead on the lattice the parameter space $\{\beta, am, N_f, N_t\}$ (implying that the infinite volume limit is taken) can be explored. Due to the rooting of the determinant, simulating a non-integer number of flavors to find N_f^{tric} can be easily done using staggered fermions [105] by keeping N_t fixed. The Frankfurt group provides an extensive study exploring the critical surfaces in this large parameter space for which they find $N_f^{\text{tric}}(N_t = 4) = 1.719(24)$ and $N_f^{\text{tric}}(N_t = 6) = 2.23(8)$ indicating an increase with N_t [86]. This means that on coarse lattices with $N_t = 4$ a 1st order scenario is favored in the two flavor theory $N_f = 2$, whereby finer lattices suggest a 2nd order transition in the continuum. By projecting the critical surfaces on the (am, N_t) plane, they determine $N_t^{\text{tric}}(N_f)$ by investigating possible tricritical scaling. On $N_t = 4, 6, 8$ and $N_f = 5, 6, 7$ using unimproved staggered fermions they find $N_t^{\text{tric}}(N_f) < \infty$ for $N_f \in [2, 6]$ which implies that fine lattices with $N_t > N_t^{\text{tric}}$ show crossover leading to 2nd order phase transitions in the chiral and continuum limit. These findings have a crucial impact on the Columbia plot updating it to Fig. 2.4.

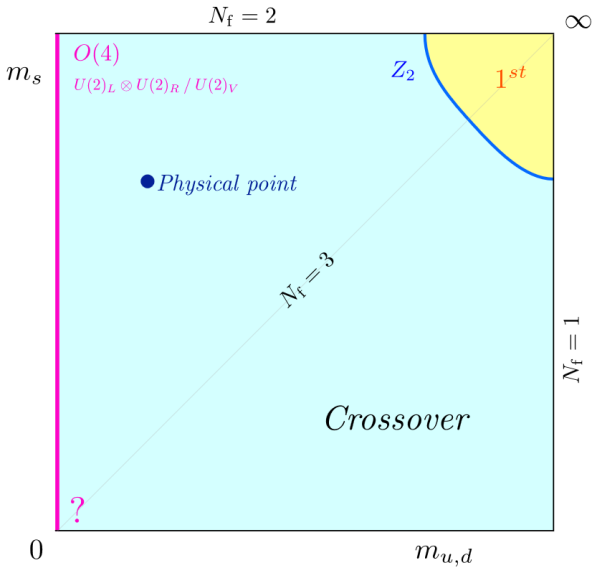

Figure 2.4: Columbia plot as predicted by the Frankfurt group [86]. Figure is also taken from this paper.

So far we can conclude that recent lattice studies favor the scenario with a 2nd order phase transition for $N_f = 2$ and finer lattices indicate a shrinking 1st order region in the case of $N_f = 3$ [86,101,106]. These scenarios are compatible with a 2nd order phase transition along the m_s axis of Fig. 2.4 whose universality class might change.

We realize that first principle methods such as lattice QCD are indispensable to obtain correct and model independent results. For this purpose full control over the systematics such as a reliable continuum limit are mandatory. Nevertheless, effective theories or low energy models remain an important tool, especially for regions which are not yet accessible by lattice QCD.

2.6 Phase diagram in T-μ_B plane

In the last Section we discussed the current status of the QCD phase diagram in the mass plane. Especially the order of the phase transition in the chiral limit remains an open question. However, Nature presents us small but finite quark masses representing a single point in the Columbia plot. Hence neither chiral nor center symmetry breaking or rather restoration are completely realized due to their explicit breaking by finite quark masses. Nevertheless, chiral symmetry is suitable to investigate the thermal properties of QCD due to its approximate Nature as discussed in detail in Section 2.4.
The possible different phases of strongly interacting matter are usually presented as functions of temperature and baryonic chemical potential μ_B as shown in Fig. 2.5. The latter indicates a grand canonical ensemble, which allows a finite net-baryon number. QCD is symmetric under $\mu_B \to -\mu_B$, whereby negative values of the chemical potential correspond to a finite net amount of anti-baryons.

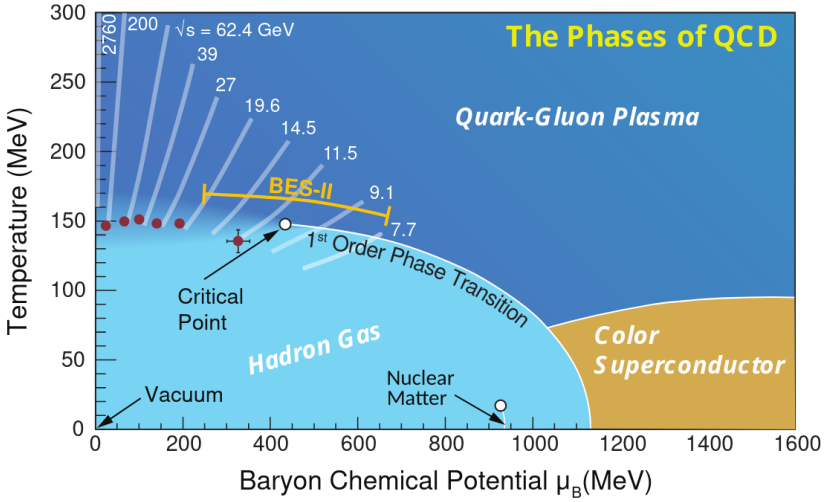

Figure 2.5: Schematic QCD phase diagram as a function of baryon chemical potential μ_B and temperature T. The collision energies of various experiments such as the BES-II scan program at RHIC are pointed out. Figure from [42].

What do we know for certain about the phase diagram? For low temperatures and chemical potential we are in the confined or hadronic phase. The system can be well described by the hadron resonance gas model (HRG) which takes possible inelastic interactions as resonances of the hadrons into account. Under extreme conditions of high temperature, chemical po-

tential or magnetic field, the system is too energetic as it can be described by the hadronic picture. The constituents are no longer locked in the confined phase, instead they start to liberate, freely move and form a highly interacting state of matter - the QGP (recall Section 2.2). This transition at $\mu_B = 0$ can be investigated via lattice QCD. It turned out that there is no sharp transition temperature, instead we face a transition region in which the chiral observables rapidly change [12]. The discovery of a so-called crossover has had crucial consequences for our understanding of the early universe, since the small asymmetry of baryons and anti-baryons implies a negligible μ_B [13]. So far, direct lattice simulations at finite density are hindered due to the sign problem. By performing simulations at vanishing (recent results e.g. [107]) or purely imaginary μ_B, the sign problem can be circumvented and results at finite and real chemical potential can be obtained by Taylor expansions. The imaginary μ_B method allowed us to calculate the transition line $T_c(\mu_B)$ of the crossover with unreached high precision. These computations up to $\mu_B \simeq 300$ MeV showed no sign of critical behavior [33]. Notably, these results are close to the chemical freeze-out temperatures T_{ch} calculated via a comparison of HRG model predictions to experimental results [108] (red points of Fig. 2.5), which agrees with the expectation that $T_{\mathrm{ch}} < T_c$ [109, 110].
The vacuum state at zero temperature and chemical potential is free of baryons. Increasing μ_B corresponds to adding energy to the system until the baryon number jumps discontinuously to finite values. The transition from the vacuum to the macroscopic nuclear matter density $n_0 \approx 0.16$ fm^{-3} is of 1$^{\mathrm{st}}$ order at $\mu_B \simeq m_N - 16$ MeV $\simeq 922$ MeV and $T = 0$, the nucleon mass m_N minus the nucleon binding energy [111]. The so-called nuclear liquid gas transition has been extensively studied theoretically using e.g. Hartree-Fock methods [112] or more recently with the quantum van der Waals HRG model [113] or an effective lattice field theory [114]. Increasing the temperature weakens the 1$^{\mathrm{st}}$ order phase transition (experimental evidence at e.g. [115]) until the latent heat vanishes at a critical endpoint $T_c \simeq 20$ MeV and $\mu_B^c \simeq 900$ MeV which is confirmed experimentally [116, 117].
The detection of gravitational waves of neutron star mergers as first measured by LIGO [15] opens a new possibility to study very dense astronomical objects which correspond to high μ_B. The high densities present in the inner core of such objects could lead to a QGP phase at low temperature and high chemical potential. Such a "cold" QGP phase is expected due to the assumed chiral symmetry restoration at high μ_B caused by screened color interactions [111]. Recent studies such as [118, 119] simulate neutron star mergers, suggest signals in the spectrum of gravitational waves to identify the transition from hadrons to quark matter and propose a 1$^{\mathrm{st}}$ order phase transition. At high μ_B, exotic phases such as color-superconductivity could appear, in which a color neutral $\langle \bar{q}q \rangle$ quark condensate could form which breaks color symmetry [120]. So far, no experimental evidence is found yet, which could change in the future due to the observation of gravitational waves of e.g. neutron star mergers. For a review of color superconductivity see [121].
Following both axes separately: 1) There is evidence for a smooth crossover transition at $\mu_B = 0$ in the high temperature region [12]. 2) On the other hand, there is a real phase transition expected for low temperatures beyond the value of the chemical potential for the nuclear liquid gas transition due to the expected restoration of chiral symmetry. Calculations based on Nambu–Jona-Lasinio or linear sigma models such as [122] or random matrix models [111] predict a 1$^{\mathrm{st}}$ order phase transition. It is important to note that these are strong arguments but no strict proofs since first principle lattice QCD simulations at high density are still hindered by the sign problem. It follows from these arguments that the 1$^{\mathrm{st}}$ order transition line starting at some high μ_B and $T = 0$ has to end in a critical endpoint, since the transition turns into a crossover at vanishing chemical potential.

To summarize: There are good reasons to assume the existence of a critical endpoint in the T-μ_B plane separating the hadronic from the QGP phase, but clear proofs are still missing - both theoretically and experimentally. Heavy ion collision experiments at RHIC or in the future at FAIR and NICA, or the observation of neutron star mergers together with the theoretical development of lattice QCD methods at finite density could disclose the secret of the existence and location of the critical endpoint in the near future.

3 Methods

A remarkable feature of QCD is the strong coupling in the low energy region which hinders the application of perturbative approaches. By investigating confinement on a discretized space time, Wilson laid the foundation of lattice QCD [31] which soon turned out to be suitable to study non-abelian gauge theories numerically as shown by Creutz for SU(2) [123, 124]. In this chapter I want to briefly discuss some key concepts of (thermal) lattice QCD with the focus on staggered fermions, the introduction of a chemical potential and its consequences as well as the basics of (rational) hybrid monte carlo methods. For this purpose I chose some selected topics of textbooks such as [25–28, 38, 125] and my Master thesis [126].

3.1 Finite temperature field theory

The concepts of statistical physics pave the way for calculations of many-body systems at finite temperature. We start with a short introduction to (fermionic) thermal field theory, sketch the derivation of a path integral representation of the partition function for fermionic oscillators and extend it to Dirac fields. The following discussion is based on [125, 126].

Starting from the definition of the partition function of a canonical ensemble with Hamiltonian $\hat{H}$

$$Z = \mathrm{tr}\left(e^{-\beta\hat{H}}\right) := \mathrm{tr}\left(e^{-\tau\hat{H}}\right) = \lim_{N\to\infty} \mathrm{tr}\left(\prod_{k=1}^{N} e^{\frac{-\tau\hat{H}}{N}}\right) := \lim_{N\to\infty} \mathrm{tr}\left(\prod_{k=1}^{N} e^{-\Delta\tau\hat{H}}\right), \tag{3.1}$$

the path integral can be derived by slicing the exponent in N pieces. The limit is necessary to use the Trotter decomposition and evaluating the separated kinetic and potential part of $\hat{H}$ on corresponding (conjugate) position and momentum eigenstates.
To derive an expression of the partition function for fermions, we begin with a fermionic oscillator whose Hamiltonian reads $\hat{H} = \omega(\hat{a}^\dagger\hat{a} - 1/2)$. Then the partition function can be obtained according to

$$Z = \mathrm{tr}\left(e^{-\beta\hat{H}}\right) = \langle 0|\, e^{-\tau\hat{H}}\, |0\rangle + \langle 1|\, e^{-\tau\hat{H}}\, |1\rangle\,, \tag{3.2}$$

which can be written in the path integral representation by using anti-commuting Grassmann numbers $\psi^\dagger$ and ψ. The creation and annihilation operators obey the anti-commutation relations

$$\{\hat{a}, \hat{a}\} = 0 = \{\hat{a}^\dagger, \hat{a}^\dagger\}, \qquad \{\hat{a}, \hat{a}^\dagger\} = 1, \tag{3.3}$$

with the following eigenstates

$$|\psi\rangle = e^{-\psi\hat{a}^\dagger}\,|0\rangle \qquad \Longrightarrow \qquad \hat{a}\,|\psi\rangle = \psi\,|\psi\rangle\,, \tag{3.4}$$

$$\langle\psi| = \langle 0|\, e^{-\hat{a}\psi^\dagger} \qquad \Longrightarrow \qquad \langle\psi|\,\hat{a}^\dagger = \langle\psi|\,\psi^\dagger, \tag{3.5}$$

and a vacuum state defined as $\hat{a}\,|0\rangle = 0$. Exploiting some features of Grassmann numbers such as [125]

$$\int \mathrm{d}\psi^\dagger \mathrm{d}\psi e^{-\psi^\dagger \psi}\,|\psi\rangle\,\langle\psi| = \mathbb{1}, \tag{3.6}$$

$$\int \mathrm{d}\psi^\dagger \mathrm{d}\psi e^{-\psi^\dagger \psi}\,\langle -\psi|\,e^{-\tau\hat{H}}\,|\psi\rangle = \langle 0|\,e^{-\tau\hat{H}}\,|0\rangle + \langle 1|\,e^{-\tau\hat{H}}\,|1\rangle = \mathrm{tr}\;e^{-\tau\hat{H}}, \tag{3.7}$$

the path integral representation of the partition function for the fermionic oscillator reads

$$Z = \lim_{N\to\infty} \int \mathrm{d}\psi_N^\dagger \mathrm{d}\psi_N \;...\; \int \mathrm{d}\psi_1^\dagger \mathrm{d}\psi_1\; e^{-S} \tag{3.8a}$$

$$:= \int \mathcal{D}\psi^\dagger(\tau)\mathcal{D}\psi(\tau) \exp\left(-\int_0^\beta \mathrm{d}\tau \left(\psi^\dagger(\tau)\frac{\mathrm{d}\psi(\tau)}{\mathrm{d}\tau} + H\left(\psi^\dagger(\tau),\psi(\tau)\right)\right)\right), \tag{3.8b}$$

with the action

$$S = \Delta\tau \sum_{i=1}^{N} \left(\psi_{i+1}^\dagger \frac{\psi_{i+1}-\psi_i}{\Delta\tau} + H\left(\psi_{i+1}^\dagger, \psi_i\right)\right). \tag{3.9}$$

It is important to note that the Grassmann variables fulfill antiperiodic boundary conditions $\psi(\beta) = -\psi(0)$ and $\psi^\dagger(\beta) = -\psi^\dagger(0)$.
Now we generalize these results by identifying the Grassmann numbers as Dirac field operators $\psi(\tau) \to \psi(\tau,\vec{x})$ and $\psi^\dagger(\tau) \to \psi^\dagger(\tau,\vec{x})$ which obey the anti-commuting relations in analogy to $\hat{a}$ and $\hat{a}^\dagger$ of Eq. (3.3)

$$\{\psi(\tau,\vec{x}),\psi(\tau,\vec{y})\} = 0 = \{\psi^\dagger(\tau,\vec{x}),\psi^\dagger(\tau,\vec{y})\}, \tag{3.10}$$

$$\{\psi(\tau,\vec{x}), i\psi^\dagger(\tau,\vec{y})\} = i\delta(\vec{x}-\vec{y}), \tag{3.11}$$

where Dirac indices are suppressed. First we note that the Hamiltonian density can be calculated by a Legendre transformation of the (free) Lagrangian

$$H = \pi\partial_0\psi - \mathcal{L} \tag{3.12a}$$

$$= \frac{\partial\mathcal{L}}{\partial(\partial_0\psi)}\partial_0\psi - \bar{\psi}(i\gamma_\mu\partial^\mu - m)\psi \tag{3.12b}$$

$$= \bar{\psi}(-i\gamma_k\partial^k + m)\psi, \tag{3.12c}$$

and rewritten to the Hamiltonian in the field operator language

$$\hat{H} = \int \mathrm{d}x^3 \bar{\psi}(\tau,\vec{x})(-i\gamma^k\partial_k + m)\psi(\tau,\vec{x}). \tag{3.13}$$

Ignoring the temporal and spatial integrals, the exponent of Eq. (3.8b) at the operator level with $\psi := \psi(\tau,\vec{x})$ and $\psi^\dagger := \psi^\dagger(\tau,\vec{x})$ reads

$$\psi^\dagger\partial_\tau\psi + \bar{\psi}(-i\gamma^k\partial_k + m)\psi = \bar{\psi}(\gamma_0\partial_\tau - i\gamma^k\partial_k + m)\psi \tag{3.14a}$$

$$:= L_E \tag{3.14b}$$

$$= -\mathcal{L}(\tau \to i\tau), \tag{3.14c}$$

leading to the partition function of the free Dirac theory at finite temperature

$$Z = \int \mathcal{D}\bar{\psi}(\tau,\vec{x})\mathcal{D}\psi(\tau,\vec{x}) \exp\left(-\int_0^\beta \mathrm{d}\tau \int \mathrm{d}x^3 L_E\right). \tag{3.15}$$

It is convenient to rewrite L_E using the Euclidean version of the Dirac matrices

$$\gamma_0^E = \gamma^0, \qquad \gamma_k^E = -i\gamma^k, \qquad \text{with} \qquad k = 1, 2, 3, \tag{3.16}$$

obeying

$$\{\gamma_\mu^E, \gamma_\nu^E\} = 2\delta_{\mu,\nu}, \qquad \gamma_\mu^{\dagger,E} = \gamma_\mu^E, \tag{3.17}$$

leading to

$$L_E = \bar{\psi}(\gamma_\mu \partial_\mu + m)\psi, \tag{3.18}$$

with $\gamma_\mu := \gamma_\mu^E$. As before, the fields obey the antiperiodic boundary conditions $\psi(\beta, \vec{x}) = -\psi(0, \vec{x})$ and $\bar{\psi}(\beta, \vec{x}) = -\bar{\psi}(0, \vec{x})$.
As stated in Eq. (3.14c), by extending the temporal dimension to the imaginary axis $\tau \to i\tau$ the Euclidean Lagrangian L_E can be obtained by its Minkowski version $\mathcal{L}$ - a procedure which is called Wick rotation.

3.2 Lattice QCD

In the last Section we derived the path integral representation of the free Dirac theory at finite temperature. But QCD is a non-abelian gauge theory based on $\mathrm{SU}(3)_c$ which makes the replacement of ∂_μ with its covariant version D_μ necessary. Hence interactions between fermionic and gauge fields (recall Eq. (2.1b)) are inevitable. The full path integral of QCD with quarks and gluons cannot be solved analytically (yet). Discretizing space time on a 3d+1 hypercubic lattice Λ, we are left with a finite number of integrals giving access to the powerful tool of Monte Carlo methods to solve them numerically. This Section is mainly based on [38, 127, 128].

3.2.1 Gauge action

It is convenient to place the fermionic fields on the sites of the 4d lattice which are connected by the so-called gauge links $U_\mu(n)$, where n is a point of the space time lattice. They are needed to enforce gauge invariance to relate quark fields at neighboring lattice sites n and $n \pm \hat{\mu}$. This is important for the discretization of the (covariant) derivative in the fermionic action. The following expressions which appear in the symmetric difference quotient with $g(n) \in \mathrm{SU}(3)$

$$\bar{\psi}(n)\psi(n + \hat{\mu}) \to \bar{\psi}(n)g^\dagger(n)g(n + \hat{\mu})\psi(n + \hat{\mu}), \tag{3.19}$$

$$\bar{\psi}(n)\psi(n - \hat{\mu}) \to \bar{\psi}(n)g^\dagger(n)g(n - \hat{\mu})\psi(n - \hat{\mu}), \tag{3.20}$$

are obviously not gauge invariant. By introducing $U_\mu(n)$, we end up with gauge invariant expressions

$$\bar{\psi}(n)U_\mu(n)\psi(n + \hat{\mu}) \to \bar{\psi}(n)g^\dagger(n)\tilde{U}_\mu(n)g(n + \hat{\mu})\psi(n + \hat{\mu}), \tag{3.21}$$

$$\bar{\psi}(n)U_\mu^\dagger(n - \hat{\mu})\psi(n - \hat{\mu}) \to \bar{\psi}(n)g^\dagger(n)\tilde{U}_\mu^\dagger(n - \hat{\mu})g(n - \hat{\mu})\psi(n), \tag{3.22}$$

if the gauge link transforms according to

$$U_\mu(n) \to \tilde{U}_\mu(n) = g(n)U_\mu(n)g^\dagger(n + \hat{\mu}). \tag{3.23}$$

In continuum QCD the generalization of such an object is known as parallel or gauge transporter or Wilson line [25], whose lattice version between neighboring points takes on the form

$$U_\mu(n) = e^{iagA_\mu(n)}. \tag{3.24}$$

a corresponds to the lattice spacing and A_μ are the gauge fields appearing in Eq. (2.2). These gauge links enable us to construct the smallest non-trivial closed loop, the so-called plaquette

$$\begin{aligned} P_{\mu\nu}(n) &= U_\mu(n)U_\nu(n+\hat{\mu})U_{-\mu}(n+\hat{\mu}+\hat{\nu})U_{-\nu}(n+\hat{\nu}) \\ &= U_\mu(n)U_\nu(n+\hat{\mu})U_\mu^\dagger(n+\hat{\nu})U_\nu^\dagger(n), \end{aligned} \tag{3.25}$$

with which a possible discretization of the continuum gauge action

$$S_G = \int \mathrm{d}^4x \mathcal{L}_G = \int \mathrm{d}^4x \frac{1}{4}\mathrm{tr}\ F_{\mu\nu}F_{\mu\nu}, \tag{3.26}$$

can be written as

$$S_G[U] = \beta \sum_{n\in\Lambda} \sum_{\mu<\nu} \left(1 - \mathrm{Re\ tr}\ P_{\mu\nu}/3\right). \tag{3.27}$$

The discretization effects are of $\mathcal{O}(a^2)$. By Taylor expanding the plaquettes, gauge links and fields and the usage of the Baker-Campbell-Hausdorff formula, it is possible to show that the continuum version of Eq. (3.27) is Eq. (3.26) in the limit $a \to 0$ and $\beta = 6/g^2$ [127]. Obviously the discretization of the gauge action is not unique which allows us to add and change terms of the discretized gauge action as long as the correct continuum version is matched for $a \to 0$. Lattice artifacts are caused by terms that only vanish in the continuum limit and hence are present at finite spacing. A suitable strategy to reduce these artifacts is the so-called Symanzik improvement [129, 130]. In this approach, further terms are added to the action including "extended" plaquettes of length $6a$ $R_{\mu\nu}$

$$S_{\mathrm{Sym.}} = \beta \sum_{n\in\Lambda} \sum_{\mu<\nu} \left(c_0\, \mathrm{Re\,tr}\left(\mathbb{1} - P_{\mu\nu}\right) + c_1\, \mathrm{Re\,tr}\left(\mathbb{1} - R_{\mu\nu}\right)\right). \tag{3.28}$$

The coefficients can be calculated at leading order in lattice perturbation theory. At tree-level, one obtains the coefficients $c_0 = \frac{5}{3}$ and $c_1 = -\frac{1}{12}$ [127].

3.2.2 Staggered fermions

So far we discussed the implementation of an improved gauge action on the lattice. Adding quarks is not such a straightforward task. For our thermal studies in the physical point a proper realization of chiral symmetry is important. According to the Nielsen–Ninomiya theorem [131–133], there is always a price to pay when fermions are discretized on a lattice. The most important statement of this theorem for our thermal studies is the impossibility to implement a doubler-free discretized version of fermions obeying chiral symmetry. Staggered fermions provide a computationally "cheap" possibility to significantly reduce the number of doublers by keeping a remnant of chiral symmetry. The following discussion is based on [38, 126, 128, 134].

Naive discretization of the fermionic action and doublers

Let us first start with the continuum Euclidean fermionic action

$$S_F = \int \mathrm{d}x^4 \bar{\psi}(\gamma_\mu D^\mu + m)\psi, \tag{3.29}$$

which can be straightforwardly discretized as

$$S_F[\bar{\psi},\psi,U] = a^4 \sum_{n\in\Lambda} \bar{\psi}(n) \left(\sum_{\mu=1}^{4} \gamma_\mu \frac{U_\mu(n)\psi(n+\hat{\mu}) - U_\mu^\dagger(n-\hat{\mu})\psi(n-\hat{\mu})}{2a} + m\psi(n) \right), \quad (3.30)$$

with the the symmetric difference quotient leading to $\mathcal{O}(a^2)$ (cmp. to Eqs. (3.21) and (3.22)). The 4d integration on the lattice is introduced as $a^4 \sum_{n\in\Lambda}$ with $a_t = a$. The quark propagator can now be calculated by a discrete Fourier transformation and reads in the free case ($U_\mu = \mathbb{1}$) [38]

$$S(p) = \frac{m\mathbb{1} - i\sum_\mu \gamma_\mu \frac{\sin(p_\mu a)}{a}}{m^2 + \frac{\sum_\mu \sin^2(p_\mu a)}{a^2}}. \quad (3.31)$$

The $\sin^2(p_\mu a)$ leads to 15 additional and unphysical poles, although only one single fermion should be described. These so-called doublers are present at any finite spacing and hence cause an incorrect continuum limit. In the chiral limit these poles are all located in the first Brillouin zone (momentum $p_\mu \in [-\pi/a, \pi/a]$) and are a natural consequence of the lattice formulation and discrete Fourier transformation. There are several methods to handle the inevitable appearance of doublers on the lattice, e.g. Wilson or staggered fermions - all with their own advantages and disadvantages. We focus here on the latter which are suitable to study finite temperature QCD in the physical point due to their low computational costs and remnant of chiral symmetry.

Staggered transformations

The main idea of staggered or Kogut-Susskind fermions [135] is to transform ψ and $\bar{\psi}$ in such a way that the action Eq. (3.30) is identical for all four Dirac components [38]. Keeping only one of them leads to an action without Dirac structure and thus to a reduction from 16 degrees of freedom to 4. This is achieved by the transformation

$$\psi(n) = \gamma_1^{n_1}\gamma_2^{n_2}\gamma_3^{n_3}\gamma_4^{n_4}\psi(n)', \quad (3.32a)$$

$$\bar{\psi}(n) = \bar{\psi}(n)'\gamma_4^{n_4}\gamma_3^{n_3}\gamma_2^{n_2}\gamma_1^{n_1}, \quad (3.32b)$$

where the γ-matrices are in their Euclidean representation (recall Eqs. (3.16) and (3.17)) and $n_1, ..., n_4$ are the components of n. This obviously mixes the space-time and Dirac indices and leaves the mass term invariant. The kinetic part contains terms of the form $\bar{\psi}(n)\gamma_\mu U_\mu \psi(n \pm \hat{\mu})$, whereby the γ_μ can be interchanged with the remaining γ-matrices which are present after staggered transformations Eqs. (3.32a) and (3.32b). The resulting sign depends on the direction $\hat{\mu}$ and is taken into account by η_μ, which replaces the γ_μ of Eq. (3.30). The resulting action reads

$$S_F[\bar{\psi}',\psi',U] = a^4 \sum_{n\in\Lambda} \bar{\psi}(n)' \left(\sum_{\mu=1}^{4} \eta_\mu(n) \frac{U_\mu(n)\psi(n+\hat{\mu})' - U_\mu^\dagger(n-\hat{\mu})\psi(n-\hat{\mu})'}{2a} + m\psi(n)' \right) \quad (3.33)$$

and η_μ takes on the values

$$\eta_1(n) = 1 \quad (3.34a)$$

$$\eta_2(n) = (-1)^{n_1} \quad (3.34b)$$

$$\eta_3(n) = (-1)^{n_1+n_2} \quad (3.34c)$$

$$\eta_4(n) = (-1)^{n_1+n_2+n_3}. \quad (3.34d)$$

Due to the fact that Eq. (3.33) does not include γ_μ, it has the same form for all Dirac components. Keeping one of them makes it possible to avoid the Dirac structure and to express the action in terms of the remaining Grassmann fields $\bar{\chi}$ and χ whose color indices remain suppressed:

$$S_F[\bar{\chi},\chi,U] = a^4 \sum_{n\in\Lambda} \bar{\chi}(n) \left(\sum_{\mu=1}^{4} \eta_\mu(n) \frac{U_\mu(n)\chi(n+\hat{\mu}) - U_\mu^\dagger(n-\hat{\mu})\chi(n-\hat{\mu})}{2a} + m\chi(n) \right) \tag{3.35a}$$

$$= a^4 \sum_{n,k\in\Lambda} \bar{\chi}(n) \left(\sum_{\mu=1}^{4} \eta_\mu(n) \frac{U_\mu(n)\delta_{k,n+\hat{\mu}} - U_\mu^\dagger(n-\hat{\mu})\delta_{k,n-\hat{\mu}} + m\delta_{k,n}}{2a} \right) \chi(k) \tag{3.35b}$$

$$:= a^4 \sum_{n,k\in\Lambda} \bar{\chi}(n) M_F(n|k) \chi(k). \tag{3.35c}$$

Which symmetries are encoded in the staggered action Eq. (3.35a) and how many quarks are actually taken into account? Let us restrict the following discussion to the free case $U_\mu = \mathbb{1}$ for simplicity. Mixing Dirac and space-time indices indicates that the Dirac structure can be restored in Eq. (3.35a), such that the staggered action is a $N_f = 4$ flavor theory. This can be achieved by a reduction of the Brillouin zone by dividing the primary lattice into 4d hypercubes of unit-length. Then the sum over all lattice points is replaced by a sum over the hypercubes and their corners [136]. However, under the assumption that the lattice has an even number of points in all directions, the new quark fields are given as [38]

$$q(z)_{\alpha t} = \frac{1}{8} \sum_s (\gamma_1^{s_1}\gamma_2^{s_2}\gamma_3^{s_3}\gamma_4^{s_4})_{\alpha t}\, \chi(2z+s), \tag{3.36}$$

with

$$n_\mu = 2z_\mu + s_\mu, \qquad z_\mu = 0,1,...,N_\mu/2-1, \qquad s_\mu = 0,1. \tag{3.37}$$

Here z_μ denotes the corresponding hypercubes with corners s_μ whose origins have a distance of $2a$. The index α in Eq. (3.36) is the Dirac and t is the so-called taste index $t = 1,2,3,4$. Now the action can be rewritten with the quark fields as [38] ($U_\mu(n) = \mathbb{1}$)

$$S_F[q,\bar{q}] = (2a)^4 \sum_z \left(m\mathrm{tr}(\bar{q}(z)q(z)) + \sum_\mu \mathrm{tr}(\bar{q}(z)\gamma_\mu \nabla_\mu q(z)) - a\sum_\mu \mathrm{tr}(\bar{q}(z)\gamma_5 \Delta_\mu q(z)\gamma_\mu\gamma_5) \right). \tag{3.38}$$

Since the sites of the lattice are now separated by $2a$, the derivatives in the above equation read

$$\nabla_\mu q(z) = \frac{q(z+\hat{\mu}) - q(z-\hat{\mu})}{4a}, \qquad \Delta_\mu q(z) = \frac{q(z+\hat{\mu}) - 2q(z) + q(z-\hat{\mu})}{4a^2}. \tag{3.39}$$

The last term in Eq. (3.38) mixes the tastes of $\bar{q}$ and q whereby the first two terms are diagonal in taste space. The so-called taste breaking term vanishes only in the continuum limit and hence represents another (unwanted) lattice artifact. In the case of a "mild" or almost absent taste breaking, a staggered fermion flavor describes 4 nearly degenerate continuum fermions. This leads to the rooting practice in which one takes the fourth root of the fermion determinant to eliminate the contribution of the doublers (see below Eq. (3.40b)). To illustrate this we integrate out the fermionic part of the partition function with the staggered

action S_F of Eq. (3.35c) and restrict the discussion to a (continuum) one flavor theory

$$Z = \int \mathcal{D}U\mathcal{D}\bar{\chi}\mathcal{D}\chi e^{-S_F[\bar{\chi},\chi,U]-S_G} \tag{3.40a}$$

$$= \int \mathcal{D}U \mathrm{det}M_F(U) e^{-S_G} \rightarrow \int \mathcal{D}U \left(\mathrm{det}M_F(U)\right)^{1/4} e^{-S_G}, \tag{3.40b}$$

with

$$\mathcal{D}\chi = \prod_{n\in\Lambda} d\chi(n), \qquad \mathcal{D}U = \prod_{n\in\Lambda}\prod_{\mu=1}^{4} dU_\mu(n). \tag{3.41}$$

The rooting procedure is a controversial topic (see e.g. [137]), since taking the fourth root is only reasonable in the continuum, in which the tastes are degenerate. It remains unclear if the universality class of the underlying theory might change and if locality is actually guaranteed in the continuum. This is questionable due to the interaction of the tastes. It is important to note that crosschecks between the Wilson and staggered quarks at finite temperature were performed. The studies [138,139] demonstrate a great agreement of important quantities such as the chiral observables, Polyakov loop and strange quark susceptibility in the continuum limit. Unphysical pion masses of $m_\pi = 545, 440, 285$ MeV were used to reduce the enormous computational costs of Wilson compared to staggered fermions. The expected dependence of the mentioned observables as functions of m_π was monitored for both fermion formulations.

Chiral symmetry for staggered quarks

The following paragraph is based on [128, 134], in which the authors discuss chiral and taste symmetry breaking for staggered quarks in detail.
An important feature of staggered fermions is that they preserve a remnant of chiral symmetry. In the chiral limit Eq. (3.35a) is invariant under $\mathrm{U}(1)_e\times$ $\mathrm{U}(1)_o$ rotations, implying that χ-fields transform independently on even or odd lattice sites [134]. This symmetry exhibits a spontaneous and explicit breaking induced by the mass term, analogous to chiral symmetry in the continuum (recall Section 2.4). It can be split into a vector and axial part $\mathrm{U}(1)_V\times$ $\mathrm{U}(1)_A$, where the transformation for the latter reads

$$\chi(n) \rightarrow e^{i\alpha\eta_5(n)}\chi(n), \tag{3.42}$$

$$\bar{\chi}(n) \rightarrow \bar{\chi}(n)e^{i\alpha\eta_5(n)}, \tag{3.43}$$

with $\eta_5(n) = (-1)^{\sum_i n_i}$. Analogous to γ_5, it can be used to project χ on the even and odd lattice site states $\chi_{e,o}$ [38]. In the case of Eq. (3.38) with the quark fields q, $\mathrm{U}(1)_e\times$ $\mathrm{U}(1)_o$ is enlarged to $\mathrm{U}(4)_L\times$ $\mathrm{U}(4)_R$ corresponding to the taste structure, which is (again) explicitly broken by the mass term to $\mathrm{SU}(4)_V$ - a symmetry breaking pattern which we discussed in detail in Section 2.4 for chiral symmetry. Taking the taste breaking term into account, the symmetry breaks to $\mathrm{U}(1)_e\times$ $\mathrm{U}(1)_o$, further motivating to suppress it as much as possible. Taste breaking has crucial consequences such as an unphysical pion mass spectrum which distorts e.g. the equation of state. Therefore a proper continuum extrapolation is mandatory, for which a suitable (improved) action is needed. Stout smearing turned out to be a suitable method to efficiently suppress the taste splitting as demonstrated in [140, 141].

3.2.3 4stout smearing

A direct consequence of formulating QCD on a lattice is the introduction of an ultraviolet cut-off determined by the spacing a. Therefore, observables which are sensitive to short distance

physics near the cut-off are naturally disturbed by the resulting short range fluctuations of the gauge fields. For our thermal studies, we apply four iterative steps of stout smearing [142] - called 4stout - to reduce these lattice artifacts and to lower the taste splitting as mentioned above. The key idea of stout-smearing is the replacement of $U_\mu(n)$ with $U'_\mu(n)$ - an appropriate gauge-invariant average of its neighboring links

$$U'_\mu(n) = e^{iQ_\mu(n)} U_\mu(n), \tag{3.44}$$

with

$$Q_\mu(n) = \frac{i}{2}\left(\Omega^\dagger_\mu(n) - \Omega_\mu(n) - \frac{\mathbb{1}}{3}\mathrm{tr}\left(\Omega^\dagger_\mu(n) - \Omega_\mu(n)\right)\right), \tag{3.45}$$

$$\Omega_\mu(n) = \left(\sum_{\mu\neq\nu} \rho_{\mu\nu} C_{\mu\nu}(n)\right) U^\dagger_\mu(n), \tag{3.46}$$

$$C_{\mu\nu}(n) = U_\nu(n) U_\mu(n+\hat{\nu}) U^\dagger(n+\hat{\mu}) + U^\dagger_\nu(n-\hat{\nu}) U_\mu(n-\hat{\nu}) U_\nu(n-\hat{\nu}+\hat{\mu}). \tag{3.47}$$

For our thermal studies [33, 143, 144] we used $\rho = \rho_{\mu\nu} = 0.125$ as smearing parameter. A

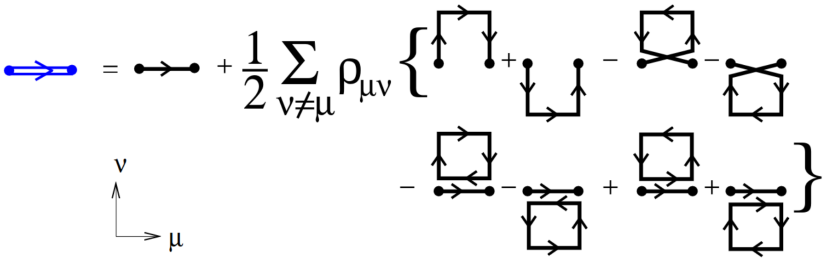

Figure 3.1: Illustration of the first stout-smearing step, whereby the exponential of $U'_\mu(n)$ is expanded in leading order and closed loops imply a trace. Figure from [142].

key feature of stout-smearing compared to other methods such as APE [145] or HYP [146] is the differentiability even after iterative applications. Hence the derivative of the action with respect to the gauge fields in the (R)HMC algorithm can be calculated analytically. A more computationally expensive alternative is (4)HEX smearing [147], which suppresses taste splitting even stronger, potentially enabling the usage of $N_t = 8$ for a controlled continuum limit. Such coarse lattices are usually discarded in continuum extrapolations for 4stout actions nowadays (see [148] for a recent study). In Fig. 3.2 the effect of different actions on the lattice pion sector is shown. 4HEX provides the strongest suppression of the taste splitting at all spacings a.

3.2.4 Scale setting

Simulating QCD on a lattice provides results in terms of lattice units. To relate these to their continuum and hence physical values, setting a scale is mandatory. Common strategies rely on precise calculations of f_π, m_Ω or w_0. In contrast to the first two, w_0 originates from a pure gluonic observable and does not involve computationally demanding calculations of fermion propagators. It is based on the Wilson flow, defined by

$$W(t = w_0^2) := t\frac{\mathrm{d}}{\mathrm{d}t}\left[t^2\langle E(t)\rangle\right]_{t=w_0^2} = 0.3. \tag{3.48}$$

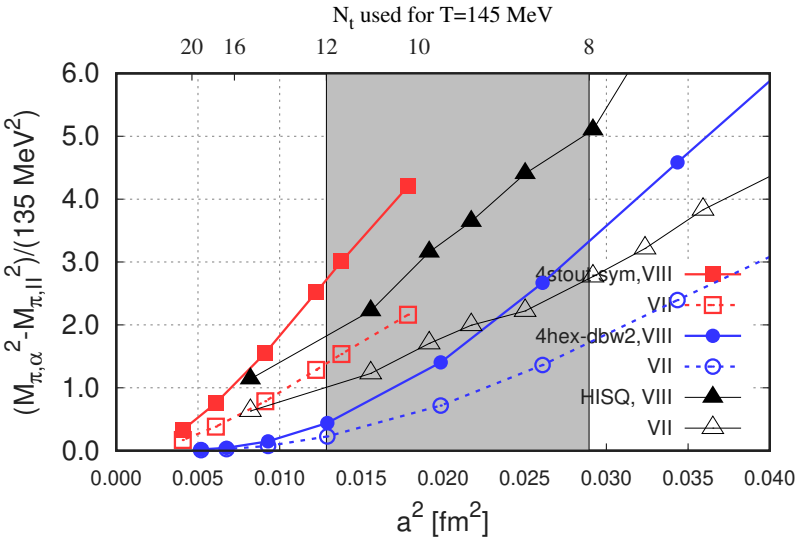

Figure 3.2: Taste breaking of the lattice pion multiplet. Quadratic mass difference between taste structure $\Gamma_{\mathrm{II}} = \gamma_0\gamma_5$ and corresponding $\Gamma_{\mathrm{VII}} = \gamma_0$ or $\Gamma_{\mathrm{VIII}} = 1$ for various actions as function of the quadratic spacing a^2: 4stout action with Symanzik improved gauge sector (red), HotQCD's HISQ [149] action (black) and 4HEX action with DBW2 [150] gauge sector (blue). Plot from [148].

Here $\langle E(t)\rangle$ is the expectation value of the gauge action of lattice configurations evolved via the Wilson flow [151, 152]. Calculating the Wilson flow implies integrating infinitesimal (e.g. stout) smearing steps of the gauge fields up to the fictitious flowtime t. Hence $W(t)$ is a pure gauge observable, not depending on fermion contributions. The measurement of w_0/a ($f_\pi a$ or $m_\Omega a$) in simulations enables the calculation of the spacing a via

$$a = \frac{w_0}{(w_0/a)_{\mathrm{lattice}}}, \tag{3.49}$$

whereby w_0 has to be known in physical units. In [152] w_0 was determined with high precision providing an agreement in the continuum limit using staggered or Wilson fermions in the physical point. Ref. [153] even takes QED effects into account, relevant for the determination of the magnetic moment of the muon. An important application of the Wilson flow is the renormalization of the measured topological charge at a chosen flow time. It preserves gauge invariance, suppresses ultraviolet fluctuations due to the smearing process of the gauge fields and enabled us to precisely study the topological features of quenched QCD. More details can be found in Sections 4.1.3 and 4.2.1.

3.3 Chemical potential

In strong interactions the baryon number as well as the corresponding quark flavor numbers are conserved quantities due to the global $\mathrm{U}(1)_V$ symmetry. Without the introduction of a chemical potential the expectation value of the corresponding net-number densities is zero. In heavy-ion collisions such a canonical system is realized but from the experimental point of view it is not possible to observe the whole phase space. In the current experimental setups

at RHIC or LHC gold or lead ions are used fulfilling the following conditions

$$\langle n_S \rangle = 0, \tag{3.50}$$

$$\frac{\langle n_Q \rangle}{\langle n_B \rangle} = 0.4. \tag{3.51}$$

The first constraint is called strangeness neutrality and comes from the absence of valence strange quarks in the nuclei. The second corresponds to the relation between the net-charge density $\langle n_Q \rangle$ and the net-baryon number density $\langle n_B \rangle$, which is determined by the ratio of the number of protons and nucleons Z/A:

$$\text{Lead} : \frac{\langle n_Q \rangle}{\langle n_B \rangle} = \frac{82}{207} \approx 0.4, \tag{3.52}$$

$$\text{Gold} : \frac{\langle n_Q \rangle}{\langle n_B \rangle} = \frac{79}{197} \approx 0.4. \tag{3.53}$$

To match these experimental conditions, a grand canonical system with non-vanishing net-chemical potentials is mandatory. As shown in Eq. (2.28) for the baryon number, we can define the particle number operator according to

$$\hat{N} = \int \mathrm{d}x^3 \bar{\psi}(x)\gamma_0\psi(x) = \int \mathrm{d}x^3 \psi^\dagger(x)\psi(x). \tag{3.54}$$

The extension from canonical to grand canonical systems naturally occurs by adding a term of the form $\mu\hat{N}$ to the Hamiltonian $\hat{H}$

$$Z = \mathrm{tr}\left(e^{-(\hat{H}-\mu\hat{N})/T}\right). \tag{3.55}$$

Then the number density can be calculated as

$$\langle n_i \rangle = \frac{T}{V}\frac{\partial \ln(Z)}{\partial \mu_i} \qquad i = B, Q, S \tag{3.56}$$

for the baryon number B, electric charge Q and strangeness S. For our thermal studies at the physical point the three light quarks u, d, s play the dominant role to monitor chiral symmetry breaking or restoration.

Chemical potential on the lattice

As indicated by Eq. (3.55), we can straightforwardly extend the Euclidean action Eq. (3.29) to a grandcanonical system by defining

$$S_F = \int \mathrm{d}x^4 \bar{\psi}\left(\gamma_\mu D_\mu + \mu\gamma_0 + m\right)\psi \tag{3.57a}$$

$$= \int \mathrm{d}x^4 \bar{\psi}\left(\gamma_k(\partial_k + iA_k) + \gamma_0(\partial_0 + iA_0 + \mu) + m\right)\psi \tag{3.57b}$$

$$:= \int \mathrm{d}x^4 \bar{\psi} M_F(\mu)\psi. \tag{3.57c}$$

Applying the same strategy of adding a term of the form $\bar{\psi}\mu\gamma_0\psi$ to the discretized action in Eq. (3.30) leads to a divergent energy density in the continuum extrapolation $a \to 0$ [154]. However, the authors proposed an elegant solution by understanding the μ term as an imaginary part of the temporal component of A_0, leading to the definition of weighted temporal links (compare with Eq. (3.24))

$$U_0(\mu) = e^{a\mu}U_0, \qquad U_0^\dagger(\mu) = e^{-a\mu}U_0^\dagger. \tag{3.58}$$

3.3.1 Higher order cumulants

In Chapter 5 we reconstruct the equation of state at finite density at strangeness neutrality and beyond. For this purpose the calculation of dimensionless higher order (baryon) cumulants such as χ_1^B,χ_2^B,χ_{11}^{BS} and χ_2^S is necessary. Let us start with the dimensionless pressure $\hat{p}$

$$\hat{p} = \frac{p}{T^4} = \frac{1}{VT^3} \log Z, \tag{3.59}$$

from which we can define dimensionless cumuluants according to

$$\chi_{ijk}^{BSQ} = \frac{\partial^{i+j+k} \hat{p}}{\partial^i \hat{\mu}_B \partial^j \hat{\mu}_S \partial^k \hat{\mu}_B}. \tag{3.60}$$

Table 3.1: Table of the three lightest quarks and their corresponding flavor properties.

quark type	B	Q	S
u	1/3	2/3	0
d	1/3	$-1/3$	0
s	1/3	$-1/3$	-1

The following transformations give access to study fluctuations of B, Q or S by taking their quantum numbers listed in Table 3.1 into account:

$$\mu_u = \frac{1}{3}\mu_B + \frac{2}{3}\mu_Q, \tag{3.61}$$
$$\mu_d = \frac{1}{3}\mu_B - \frac{1}{3}\mu_Q, \tag{3.62}$$
$$\mu_s = \frac{1}{3}\mu_B - \frac{1}{3}\mu_Q - \mu_S. \tag{3.63}$$

Hence, we can express higher order baryon fluctuations in terms of the quark cumulants

$$\chi_1^B = \frac{1}{3}\left[\chi_1^u + \chi_1^d + \chi_1^s\right], \tag{3.64}$$
$$\chi_2^B = \frac{1}{9}\left[2\chi_{11}^{ud} + 2\chi_{11}^{us} + 2\chi_{11}^{ds} + \chi_2^s + \chi_2^d + \chi_2^u\right], \tag{3.65}$$
$$\chi_{11}^{BS} = -\frac{1}{3}\left[\chi_2^s + \chi_1^u + \chi_1^d\right], \tag{3.66}$$
$$\chi_2^S = \chi_2^s. \tag{3.67}$$

Calculating these expectation values on the lattice in the staggered formalism involves taking derivatives of Z (recall Eq. (3.40b)) with respect to the chemical potentials μ_i including terms

of the form

$$\partial_{\mu_i} \left[\det M(\mu_i)\right]^{1/4} = \frac{1}{4} \frac{1}{\left[\det M(\mu_i)\right]^{3/4}} \partial_{\mu_i} \det M(\mu_i) \tag{3.68a}$$

$$= \frac{1}{4} \left[\det M(\mu_i)\right]^{1/4} \frac{1}{\det M(\mu_i)} \partial_{\mu_i} \det M(\mu_i) \tag{3.68b}$$

$$= \frac{1}{4} \left[\det M(\mu_i)\right]^{1/4} \partial_{\mu_i} \log \det M(\mu_i) \tag{3.68c}$$

$$= \frac{1}{4} \left[\det M(\mu_i)\right]^{1/4} \partial_{\mu_i} \mathrm{tr} \log M(\mu_i) \tag{3.68d}$$

$$= \frac{1}{4} \left[\det M(\mu_i)\right]^{1/4} \mathrm{tr}\ \partial_{\mu_i} \log M(\mu_i) \tag{3.68e}$$

$$= \frac{1}{4} \left[\det M(\mu_i)\right]^{1/4} \mathrm{tr} \left[M^{-1}(\mu_i) \partial_{\mu_i} M(\mu_i)\right]. \tag{3.68f}$$

Let us denote $\partial_{\mu_i} M(\mu_i) = M'$ and $\partial_{\mu_i} = \frac{\partial}{\partial \mu_i}$. For the second derivative we additionally need to calculate the terms

$$\partial_{\mu_i} \left[M^{-1} M'\right] = \left(M^{-1}\right)' M' + M^{-1} M''. \tag{3.69}$$

The derivative of the inverse matrix can be obtained by

$$\partial_{\mu_i} M M^{-1} = M' M^{-1} + M \left(M^{-1}\right)' = 0 \tag{3.70}$$

$$\implies \left(M^{-1}\right)' = -M^{-1} M' M^{-1}. \tag{3.71}$$

We can calculate the derivatives of the staggered fermion matrix with Eq. (3.35b):

$$M'\psi(x) = \frac{1}{2} \eta_4(x) \left[U_4(x)\psi(x+\hat{4}) + U_4^\dagger(x-\hat{4})\psi(x-\hat{4})\right], \tag{3.72}$$

$$M''\psi(x) = \frac{1}{2} \eta_4(x) \left[U_4(x)\psi(x+\hat{4}) - U_4^\dagger(x-\hat{4})\psi(x-\hat{4})\right]. \tag{3.73}$$

It is straightforward to generalize the calculations up to higher order derivatives with respect to μ_i. Further information can be found in [155].

3.3.2 Isospin symmetry and strangeness neutrality

In the case of isopsin symmetry ($m_u = m_d$ and $\mu_u = \mu_d$), Eqs. (3.61) to (3.63) are reduced to

$$\mu_u = \mu_d = \mu_l = \frac{1}{3} \mu_B, \tag{3.74}$$

$$\mu_s = \frac{1}{3} \mu_B - \mu_S, \tag{3.75}$$

implying

$$\frac{\langle n_Q \rangle}{\langle n_B \rangle} = 0.5. \tag{3.76}$$

The grand canonical formulation with (imaginary) μ_B can lead to a non-vanishing net-strangeness. The task is to tune μ_S (or μ_s) in such a way, that eq. Eq. (3.50) is fulfilled for each μ_B. These chemical potentials can be related by the following differential equation

$$\frac{\mathrm{d}}{\mathrm{d}\mu_B} \frac{\partial \log Z}{\partial \mu_S} = \frac{\mathrm{d}}{\mathrm{d}\mu_B} \langle n_S \rangle = 0. \tag{3.77}$$

By using

$$\frac{\mathrm{d}}{\mathrm{d}\mu_B} = \frac{\partial}{\partial\mu_B} + \frac{\mathrm{d}\mu_S}{\mathrm{d}\mu_B}\frac{\partial}{\partial\mu_S}, \tag{3.78}$$

Eq. (3.77) can be written as

$$0 = \frac{\mathrm{d}}{\mathrm{d}\mu_B}\langle n_S\rangle = \chi_{BS}^{11} + \frac{\mathrm{d}\mu_S}{\mathrm{d}\mu_B}\chi_S^2 \iff \frac{\mathrm{d}\mu_S}{\mathrm{d}\mu_B} = -\frac{\chi_{BS}^{11}}{\chi_S^2}, \tag{3.79}$$

and solved by e.g. Runge-Kutta methods. First calculations of the BMW group for the transition line $T_c(\mu_B)$ including strangeness neutrality were performed in 2015 [156].
However, a perfect strangeness neutrality along all observables can never be guaranteed. Hence, we extrapolate the fluctuations, which are essential for the equation of state, to their strangeness neutral point at leading order. In practice, each Jackknife bin is extrapolated to $\langle n_S\rangle = 0 = \chi_1^S$. Let us call $\tilde{\mu}_S = \mu_S + \Delta\mu_S$ the value for which $\langle n_S\rangle = 0$ and illustrate this approach for the baryon number density χ_1^B. Expanding $\langle n_S\rangle$ at leading order yields

$$\langle n_S\rangle = \frac{\partial \log Z}{\partial\mu_S} + \frac{\partial^2 \log Z}{\partial\mu_S^2}\Delta\mu_S = 0, \tag{3.80}$$

$$\implies \Delta\mu_S = -\frac{\chi_1^S}{\chi_2^S}. \tag{3.81}$$

Then χ_1^B reads in the strangeness neutral point

$$\chi_1^B(\tilde{\mu}_S) = \chi_1^B(\mu_S) + \chi_{11}^{BS}(\mu_S)\Delta\mu_S. \tag{3.82}$$

We generalized this procedure to obtain results for the equation of state at vanishing and varying strangeness and for the case of isospin breaking, which is discussed in Section 5.2.

3.3.3 Complex action problem

Let us recall that the fermion determinant can be calculated from (compare to Eq. (3.40a))

$$\det M_F(\mu) = \int \mathcal{D}\bar{\psi}\mathcal{D}\psi e^{-S_F[U,\bar{\psi},\psi,\mu]}. \tag{3.83}$$

In the case of a vanishing chemical potential, M_F obeys the so-called γ_5 hermiticity

$$\begin{aligned}(\gamma_5 M_F)^\dagger &= (D_\mu\gamma_\mu + m)^\dagger\,\gamma_5 \\ &= (-D_\mu\gamma_0\gamma_\mu\gamma_0 + m)\,\gamma_5 \\ &= \gamma_5\,(D_\mu\gamma_\mu + m) = \gamma_5 M_F \qquad (3.84)\\ \implies M_F^\dagger &= \gamma_5 M_F\gamma_5 \qquad (3.85)\end{aligned}$$

leading to a real determinant

$$\det\, M_F^\dagger = \overline{\det\, M_F} = \det\,(\gamma_5 M_F\gamma_5) = \det\, M_F. \tag{3.86}$$

This statement is not true for finite real μ

$$\begin{aligned}(\gamma_5 M_F(\mu))^\dagger &= (D_\nu\gamma_\nu + \mu\gamma_0 + m)^\dagger\,\gamma_5 \\ &= (-D_\nu\gamma_0\gamma_\nu\gamma_0 + \mu\gamma_0 + m)\,\gamma_5 \\ &= \gamma_5\,(D_\nu\gamma_\nu - \mu\gamma_0 + m) = \gamma_5 M_F(-\mu) \qquad (3.87)\\ \implies M_F^\dagger(\mu) &= \gamma_5 M_F(-\mu)\gamma_5 \qquad (3.88)\end{aligned}$$

providing a complex determinant

$$\det M_F^\dagger(\mu) = \overline{\det M_F(\mu)} = \det(\gamma_5 M_F(-\mu)\gamma_5) = \det M_F(-\mu). \tag{3.89}$$

If μ is purely imaginary (denoted as μ_I), then we obtain again a real determinant

$$\det M_F^\dagger(\mu_I) = \det M_F(\mu_I). \tag{3.90}$$

As a part of the partition function and hence of the probability distribution, the fermion determinant has to be real and positive. Nevertheless, there are several existing methods to obtain results at finite density. In the case of our thermal studies, we used the imaginary chemical potential method for which the complex determinant problem can be circumvented. In contrast to Taylor expanding observables from vanishing chemical potential (e.g. [157,158]), this approach provides a lever arm enabling us to obtain the crossover transition line $T_c(\mu_B)$

$$\frac{T_c(\mu_B)}{T_c(\mu_B = 0)} = 1 - \kappa_2 \left(\frac{\mu_B}{T_c(\mu_B)}\right)^2 - \kappa_4 \left(\frac{\mu_B}{T_c(\mu_B)}\right)^4, \tag{3.91}$$

with high precision and lower computational costs [33]. Other methods to get results at

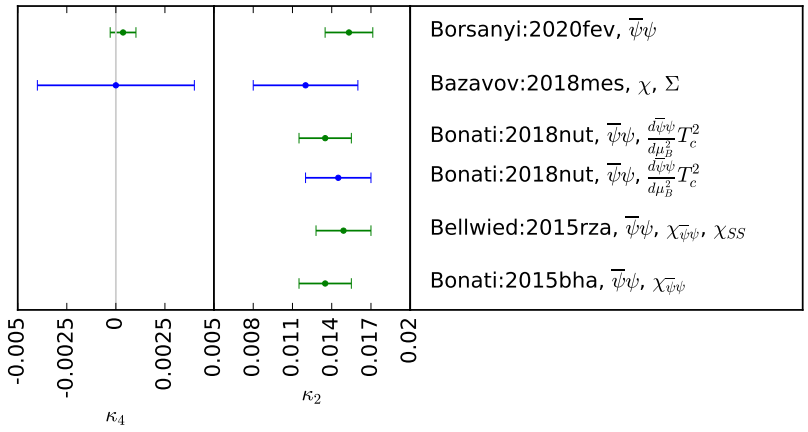

Figure 3.3: Taylor coefficients κ_2 and κ_4 of Eq. (3.91) calculated by different groups relying on extrapolation from $\mu = 0$ (blue points) and imaginary μ_I (green) obeying strangeness neutrality. Plot from our [33].

finite real μ are the density of states method (e.g. [159]), Lefschetz thimbles [160] or complex Langevin [161, 162]. I refer the reader to [163, 164] for a recent overview.

3.4 Monte Carlo methods

In the last Sections we discussed possible discretization schemes of gauge fields and fermions on a space time lattice. Now we want to use this machinery to actually calculate expectation values of observables O of interest

$$\langle O \rangle = \frac{1}{Z} \int \mathcal{D}U \; O \; \det M(U) e^{-S_G(U)}, \tag{3.92}$$

$$Z = \int \mathcal{D}U \det M(U) e^{-S_G(U)}. \tag{3.93}$$

Depending on the target theory, several fermionic determinants with appropriate chosen roots can be added to these equations which will not change the following discussion (recall Eq. (3.40b)). The equations look "inconspicuous", but we should appreciate the huge number of parameters encoded in them. Let us perform a rough estimation for a standard finite temperature lattice with $N_x = 48$ and $N_t = 12$: Each gauge link is a SU(3) matrix, implying $4 \cdot 8 = 32$ degrees of freedom leading to $4 \cdot N_x^3 \cdot N_t \cdot 32 \approx 170$ million parameters. The staggered fermion determinant has approximately $(N_c \cdot N_x^3 \cdot N_t)^2 \approx 15$ trillion entries. It is obvious that standard numerical integration is just infeasible due to the huge number of parameters. With Monte Carlo methods we are able to handle such integrals by generating samples distributed according to the underlying probability density (importance sampling). For our thermal studies, the heat bath + tempering algorithm in the case of quenched simulations and the RHMC algorithm with staggered fermions were used. The basis for these algorithms is the Metropolis-Hastings algorithm with importance sampling. Using this approach, we can approximate the expectation value of O in Eq. (3.92) with

$$\langle O \rangle = \frac{1}{N} \sum_{n=1}^{N} O(U^{(n)}), \tag{3.94}$$

where the gauge fields are distributed according to [38]

$$\mathrm{d}P(U) = \frac{\mathcal{D}U \det M(U) e^{-S_G(U)}}{\int \mathcal{D}U \det M(U) e^{-S_G(U)}}. \tag{3.95}$$

The statistical error of $\langle O \rangle$ is $\sim 1/\sqrt{N}$. The key idea is to obtain a "chain" of field configurations, whereby each new proposed set of U_μ - called U' - is generated only from the previous one, ideally following P of Eq. (3.95). Let us call $T(U'|U)$ the transition probability to obtain U' from U. The key features of the necessary algorithms are [165]

1. Positive probability: $T(U'|U) \geq 0 \; \forall \; U, U'$
2. Normalized probability: $\sum_{U'} T(U'|U) = 1 \; \forall \; U$
3. Detailed balance
$$T(U'|U)P(U) = T(U|U')P(U') \tag{3.96}$$
The probability to obtain U' from U weighted by the probability to be in configuration U, is equal to the probability to obtain U from U' weighted by the probability to be in configuration U'. This guarantees reversibility of the Markov process - a key feature of systems in (thermal) equilibrium.
4. Ergodicity: After a finite number n of steps
$$T^n(U|U') > 0. \tag{3.97}$$
It implies that the entire configuration space can be explored within a finite number of steps. I remind the reader of a similar case in classical mechanics and the Poincaré recurrence theorem, which roughly says that a mechanical system returns arbitrarily close to its initial state in a finite (but very long) time. Both concepts highlight long term behavior of the underlying systems which explore the phase/configuration space by returning to the initial state for a deterministic system (recurrence theorem) or by sampling all possible configurations (ergodicity).

A rather simple algorithm which fulfills these conditions is the Metropolis algorithm.

Metropolis algorithm

Let us start with a naive single variable update procedure:

1. Propose a new candidate U' which is a modification of U. For example

$$U'_\mu(n) = XU_\mu(n) \qquad X \in \mathrm{SU}(3), \tag{3.98}$$

with $X \in \mathrm{SU}(3)$ close to $\mathbb{1}$ and a chosen site n and direction μ. How X is selected has a strong impact on the acceptance rate and hence on the suitability of the algorithm. The main goal is to balance or rather fine tune the acceptance rate such that the system evolves in configuration space without being stuck.

2. According to the detailed balance condition, we construct a so-called accept/reject step for U'

$$r \leq \exp(-S(U') + S(U)) = \exp(-S_G(U') + S_G(U)) \frac{\det M(U')}{\det M(U)}, \tag{3.99}$$

where r is a random number uniformly distributed in $[0, 1]$. The action S is the full action with the fermion and gauge action. This is equivalent to an acceptance probability of the form

$$P = \min\left(1, \exp(-S_G(U') + S_G(U)) \frac{\det M(U')}{\det M(U)}\right). \tag{3.100}$$

This means that U' is always accepted if it decreases the action but an increase is also possible, which takes fluctuations into account.

This procedure is highly inefficient in the case of dynamical fermions since the determinant as a non-local quantity has to be computed every time. Let us first restrict the discussion to pure gauge SU(3) theories for which the heat bath algorithm is suitable.

Heat bath

The heat bath algorithm takes advantage of the fact that the action in a pure SU(3) gauge theory is a local quantity. Hence an update of one selected gauge link $U_\mu(n) \to U'_\mu(n)$ leads to a local change of the action (following the notation of Eq. (3.27))

$$\Delta S = S[U'_\mu(n)]_{\mathrm{loc}} - S[U_\mu(n)]_{\mathrm{loc}}, \tag{3.101}$$

$$S[U_\mu(n)]_{\mathrm{loc}} = \frac{\beta}{3} \mathrm{Re\ tr}\left(\mathbb{1} - U_\mu(n)\Sigma_\mu(n)\right). \tag{3.102}$$

The so-called staple

$$\Sigma_\mu(n) = \sum_{\nu \neq \mu} \left(U_\nu(n+\hat{\mu}) U^\dagger_\mu(n+\hat{\nu}) U^\dagger_\nu(n) + U^\dagger_\nu(n+\hat{\mu}-\hat{\nu}) U^\dagger_\mu(n-\hat{\nu}) U_\nu(n-\hat{\nu}) \right), \tag{3.103}$$

does not depend on the specific $U_\mu(n)$. Instead it contains the links that share a plaquette with $U_\mu(n)$. The key feature of the heat bath algorithm is to exploit locality in a way that for a chosen link, the new value $U'_\mu(n)$ is randomly selected with a local probability distribution determined by the surrounding links

$$\mathrm{d}P(U) = \mathrm{d}U \exp\left(\frac{\beta}{3} \mathrm{Re\ tr}\, U_\mu(n)\Sigma_\mu(n)\right). \tag{3.104}$$

In the case of the SU(3) gauge theory (or even SU(N)), the update procedure is done in the subgroup SU(2) [166] - called pseudo-heat bath method. Originally developed by Creutz [124], an efficient way was provided by Kennedy and Pendleton [167]. Detailed instructions can be found in [38].
In our thermal quenched studies [40, 168], one heat bath step is combined with three sweeps of overrelaxation. The latter provides a microcanonical change (similar to Hybrid Monte Carlo) such that the action is conserved. Let us illustrate overrelaxation for SU(2) which can be used for SU(3) just like in the pseudo-heat bath method:

$$U'_\mu(n) = V^\dagger_\mu(n) U^\dagger_\mu(n) V^\dagger_\mu(n), \qquad \Sigma_\mu(n) = r \cdot V_\mu(n) \;\; r \in \mathbb{R}. \tag{3.105}$$

The action remains unchanged as can be seen by setting the focus on its relevant part

$$\begin{aligned} \text{Re tr}\left[U'_\mu(n)\Sigma_\mu(n)\right] &= \text{Re tr}\left[V^\dagger_\mu(n)U^\dagger_\mu(n)V^\dagger_\mu(n) r \cdot V_\mu(n)\right] = r\text{Re tr}\left[V^\dagger_\mu(n)U^\dagger_\mu(n)\right] \\ &= \text{Re tr}\left[U_\mu(n)\Sigma_\mu(n)\right]. \end{aligned} \tag{3.106}$$

This procedure is obviously not compatible with ergodicity since we want to simulate canonical systems which take fluctuations of the energy into account. Hence the combination with the heat bath step is mandatory.

3.4.1 Parallel tempering

Simulating real phase transitions makes us face the phenomenon of critical, in the case of 2^{nd} order transitions [85], and supercritical slowing down for 1^{st} order phase transitions [40, 168]. Both cause a high auto-correlation time for the order parameter. This can be significantly reduced by employing parallel tempering. Originally used to simulate spin systems with several coexisting phases [169], the key idea of tempering is to treat the control parameter, e.g. the temperature as a dynamical variable. This can help to accelerate the decorrelation of the order parameter. Parallel tempering extends this idea by including multiple simulations (called sub-ensembles) at different parameters which can exchange configurations. Studies of spin systems such as [170, 171] or with focus on lattice QCD [172–174] demonstrate the potential of parallel tempering algorithms. Following the "quasi-recipe" of [172], parallel tempering takes advantage of the fact that the equilibrium distributions of the sub-ensembles overlap. The phase spaces Γ_i of these sub-ensembles are determined by:

1. A set of parameters p_i which can include, depending of the simulated theory, quark masses, gauge couplings, hopping parameters etc..
2. Their configurations labeled as a_i which contain e.g. gauge links or pseudo-fermion fields.
3. An action S_i which depends on 1) and 2).

The parallel tempering algorithm relies on Markov chains whose equilibrium distribution $P^{\text{eq}}_{\text{PT}}$ is the product of the N individual sub-ensemble distributions P^{eq}_i

$$P^{\text{eq}}_{\text{PT}} = \prod_{i=1}^{N} P^{\text{eq}}_i = \prod_{i=1}^{N} \frac{e^{-S_i(a_i)}}{Z_i}. \tag{3.107}$$

Exactly as for the full phase space $\Gamma_{\text{PT}} = \prod_{i=1}^{N} \Gamma_i$, the partition function Z_{PT} of the whole ensemble is $Z_{\text{PT}} = \prod_{i=1}^{N} Z_i$.

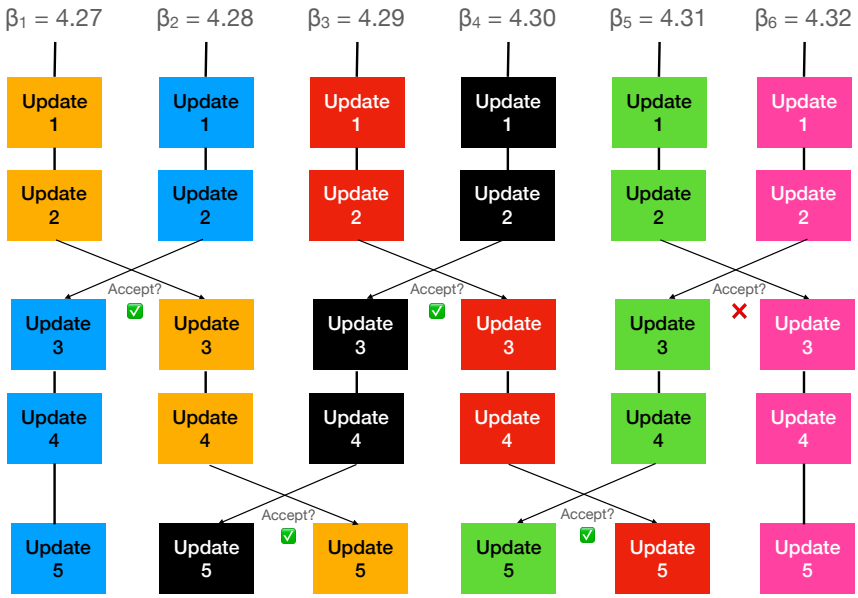

Figure 3.4: Illustration of the configuration exchange in the parallel tempering algorithm for a set of 6 sub-ensembles with individual gauge coupling β.

How does the parallel tempering algorithm work? Let us distinguish two types of Markov transitions:

1. There are N individual sub-ensembles which are updated according to the standard algorithms such as (R)HMC or heat-bath. They fulfill the detailed balance condition and run independently.

2. Now the overlap of the equilibrium distributions of the sub-ensembles is exploited which enables a transition/swap of configurations between sub-ensembles i (config. a) and j (config. b). The detailed balance condition

$$P_s(i,j)e^{-S_i(a)}e^{-S_j(b)} = P_s(j,i)e^{-S_i(b)}e^{-S_j(a)}, \tag{3.108}$$

   can be satisfied if the probability $P_s(i,j)$ for an exchange of configurations between i and j is chosen the be the Metropolis acceptance probability (compare to Eq. (3.100))

$$P_s(i,j) = \min\left(1, e^{-\Delta S}\right), \qquad \Delta S = S_i(b) - S_i(a) + S_j(a) - S_j(b). \tag{3.109}$$

   This implies that swapping configurations is more likely for neighboring ensembles which share a large overlap between their equilibrium distributions.

As a result the auto-correlation time within the sub-ensembles is reduced, since they gather contributions of the other ensembles at different parameters (Fig. 3.4). The price to pay is a resulting correlation between the observables of different sub-ensembles which has to be taken into account in the data analysis. A key feature of the parallel tempering algorithm is that the sub-ensembles are kept in equilibrium which can be reached by 1). If there are no transitions between the sub-ensembles, caused by far separated parameters for instance, then we end up with the standard Metropolis procedure and the sub-ensembles run completely independently.

3.4.2 Reweighting

Simulations are usually performed for a fixed set of parameters such as temperature or quark masses. Nevertheless it is possible to extract information about systems which are slightly different from those directly simulated. A common procedure is reweighting, which can even be used for regions in parameter space that are not accessible by direct Monte Carlo methods such as lattice QCD at finite density [175]. The following paragraph is mainly based on [176]. Let us assume we simulated a thermal system at some inverse temperature $\beta = 1/T$. Then the expectation value of an observable O reads

$$\langle O \rangle_\beta = \frac{\sum_\mu O_\mu e^{-\beta E_\mu}}{\sum_\mu e^{-\beta E_\mu}}. \tag{3.110}$$

The sum $\sum_\mu$ implies the summation over all possible states μ provided by the system. Since it is just infeasible to cover the full configuration space, Monte Carlo methods estimate the expectation value by selecting randomly (distributed according to p_{μ_i}) subsets of configurations μ_i

$$\langle O \rangle_\beta^E = \frac{\sum_{i=1}^N O_{\mu_i} p_{\mu_i}^{-1} e^{-\beta E_{\mu_i}}}{\sum_{i=1}^N p_{\mu_i}^{-1} e^{-\beta E_{\mu_i}}}. \tag{3.111}$$

If the configurations are chosen according to $p_\mu = e^{-\beta E_\mu}/Z$, we end up with the so-called importance sampling Eq. (3.94). Let us now assume we simulated at β' and now want to obtain information at β. Then the Boltzmann weights have to be changed such that $p_{\mu_i} = e^{-\beta' E_{\mu_i}}/Z_{\beta'}$

$$\langle O \rangle_\beta^E = \frac{\sum_{i=1}^N O_{\mu_i} e^{-(\beta-\beta')E_{\mu_i}}}{\sum_{i=1}^N e^{-(\beta-\beta')E_{\mu_i}}}. \tag{3.112}$$

The denominator $\sum_{i=1}^N e^{-(\beta-\beta')E_{\mu_i}}$ determines the extent of the overlap between the distributions. If it is close to zero, the method obviously fails which is referred as overlap problem. So far, this approach takes one single simulation into account which is used to reweight to another parameter set. A popular way to incorporate multiple simulations is a version of the Ferrenberg-Swendsen method [177, 178], which is called multiple histogram method.

3.4.3 Correlated multiple histogram method

The main feature of this reweighting technique is to estimate the density of states $W(E)$

$$Z(\beta) = \sum_E W(E) e^{-\beta E}, \tag{3.113}$$

and hence the partition function $Z(\beta)$ over the full range of simulation points β_i. This allows a precise interpolation of the observables of interest. We extend the results of [177, 178] and derive it for correlated data as those obtained by using parallel tempering. We published the correlated multiple histogram method in [40]. Let us restrict the discussion to a discrete set of energies. The case of a continuous energy spectrum demands the replacement $W(E) \to W(E)\mathrm{d}E$, which does not change the final equations [176].
Let us first recall that the weighted average a of data sets x_i, $i = 1, 2, ..., m$ can be calculated by minimizing

$$\chi^2 = \sum_{i,j}^m (x_i - a) \left(C^{-1}\right)_{i,j} (x_j - a), \tag{3.114}$$

with C^{-1} being the inverse covariance matrix [179]. The minimum is found for

$$a = \frac{\sum_{i,j=1}^{m} \left(C^{-1}\right)_{i,j} x_j}{\sum_{i,j=1}^{m} \left(C^{-1}\right)_{i,j}}, \tag{3.115}$$

which has minimal fluctuations in the case of correlated measurements compared to other possible linear combinations. Since $W(E)$ does not depend on any value of β it can be estimated by the densities of states of the individual simulations $W_i(E)$ according to Eq. (3.115). Thus i labels the simulation at β_i which is correlated with the other ones due to the β tempering algorithm. The histograms of the energy $N_i(E)$ are stored and can be related to the density of states by

$$W_i(E)\frac{e^{-\beta_i E}}{Z(\beta_i)} = \frac{N_i(E)}{n_i} = p_i(E), \tag{3.116}$$

where n_i is the total amount of entries of the histogram and $p_i(E)$ denotes the probability of simulation i to generate a state with energy E in the case of importance sampling [176]. In the same manner the exact density of states $W(E)$ is estimated by multiple simulations performed at the same coupling

$$W(E) = \frac{\overline{N_i}(E) Z(\beta_i)}{n_i e^{-\beta_i E}}. \tag{3.117}$$

It is important to note that $\overline{N_i}$ is the averaged histogram of these simulations, thus its error is $\sigma_i = \sqrt{g_i \overline{N_i}}$. The factor g_i takes the correlation time τ_i of the ensemble into account and reads $g_i = 1 + 2\tau_i$. To construct

$$W(E) = \frac{\sum_{i,j=1}^{m} \left(C^{-1}\right)_{i,j} W_j(E)}{\sum_{i,j=1}^{m} \left(C^{-1}\right)_{i,j}}, \tag{3.118}$$

we write with Eqs. (3.116) and (3.117) the covariance matrix according to

$$\begin{aligned} C_{i,j} &= \operatorname{cov}(W_i, W_j) && \text{(3.119a)} \\ &= \langle W_i W_j \rangle - \langle W_i \rangle \langle W_j \rangle && \text{(3.119b)} \\ &= W^2 \, \frac{\operatorname{cov}(N_i, N_j)}{\overline{N_i}\,\overline{N_j}} && \text{(3.119c)} \\ &= W^2 \, \frac{\operatorname{corr}(N_i, N_j) g_i g_j}{\sigma_i \sigma_j}. && \text{(3.119d)} \end{aligned}$$

with the shorthand notation $W_i = W_i(E)$, $N_i = N_i(E)$. Here $\operatorname{cov}(N_i, N_j)$ and $\operatorname{corr}(N_i, N_j)$ stand for components of the covariance and correlation matrix respectively which are estimated according to the standard Jackknife resampling method. Now we can write Eq. (3.118) as

$$\begin{aligned} W(E) &= \frac{\sum_{i,j=1}^{m} \sigma_i \sigma_j (g_i g_j)^{-1} \operatorname{corr}^{-1}(N_i, N_j) \, W_j}{\sum_{i,j=1}^{m} \sigma_i \sigma_j (g_i g_j)^{-1} \operatorname{corr}^{-1}(N_i, N_j)} \\ &= \frac{\sum_{i,j=1}^{m} (g_i g_j)^{-1/2} \sqrt{\frac{n_i Z_j}{n_j Z_i}} e^{E(\beta_j - \beta_i)/2} \, N_j(E) \operatorname{corr}^{-1}(N_i, N_j)}{\sum_{i,j=1}^{m} (g_i g_j)^{-1/2} \sqrt{\frac{n_i n_j}{Z_j Z_i}} e^{-E(\beta_i + \beta_j)/2} \operatorname{corr}^{-1}(N_i, N_j)}. \end{aligned} \tag{3.120}$$

In some cases the correlation matrix is singular, caused by bins which only contain a few entries. Since these bins have a very small contribution to the end result of $W(E)$, we neglect the correlation of them with other bins. In the case of uncorrelated simulations the correlation matrix is the unity matrix and we get back to the standard Ferrenberg-Swendsen equation for the density of states

$$W(E) = \frac{\sum_{i=1}^{m} g_i^{-1} N_i(E)}{\sum_{i=1}^{m} g_i^{-1} \frac{n_i}{Z_i} e^{-\beta_i E}}. \tag{3.121}$$

Assuming that the Z_i reach a fix point, they are iteratively determined by

$$Z_i = \sum_E W(E) e^{-\beta_i E}, \tag{3.122}$$

with $W(E)$ of Eq. (3.120) until Δ^2, defined as

$$\Delta^2 = \sum_i^m \left(\frac{Z_i^{(n)} - Z_i^{(n-1)}}{Z_i^{(n)}} \right)^2, \tag{3.123}$$

reaches a desired value as for example $\Delta^2 \leq 10^{-19}$. $Z_i^{(n)}$ denotes the value of Z_i after n iterations. Inserting Eq. (3.120) in Eq. (3.113), the partition function $Z(\beta)$ over the full simulation range can be evaluated. Assuming constant auto-correlation times τ_i, the g_i factors are the same for every simulation. According to Eq. (3.120) or Eq. (3.121) they represent a constant factor for all Z_i which can be dropped.
Let us discuss some crucial points for the iteration of the partition functions: They take on huge values and cannot be represented correctly on a machine, resulting in serious rounding errors. This problem can be reduced by introducing a normalization factor for all partition functions. This factor always cancels in the calculation of expectation values and hence can be freely chosen, for example Z_i/Z_1. Nevertheless, this procedure reduces the problem but does not solve it. We deal with sums of huge exponents (see Eq. (3.120)) containing E, which is proportional to the space-time volume. An appropriate solution is to work in the logarithm representation. Let us illustrate this for e.g. the denominator D of Eq. (3.121)

$$\ln D = \ln \left(\sum_{i=1}^{m} g_i^{-1} \frac{n_i}{Z_i} e^{-\beta_i E} \right) \tag{3.124a}$$

$$:= \ln \left(\sum_{i=1}^{m} e^{\alpha_i} \right) \tag{3.124b}$$

$$= \ln \left(e^{\alpha_{\max}} + \sum_{i \neq i_{\max}}^{m} e^{\alpha_{\max} + \alpha_i - \alpha_{\max}} \right) \tag{3.124c}$$

$$= \alpha_{\max} + \ln \left(1 + \sum_{i \neq i_{\max}}^{m} e^{\alpha_i - \alpha_{\max}} \right). \tag{3.124d}$$

Here $\alpha_{\max}$ stands for the largest value of the exponents α_i, whose summation index is indicated by $i_{\max}$. The logarithm of Eq. (3.124d) can be calculated precisely with the intern log1p function provided by math.h for the C-programming language.

Hybrid Monte Carlo

In the pure gauge theory, we can calculate the shift of the action in Eq. (3.99) locally. In the case of dynamical fermions we introduce a non-local quantity with the fermion determinant

which makes local update algorithms highly inefficient. The Hybrid-Monte-Carlo (HMC) algorithm [180, 181] is able to update the complete set of gauge configurations at once by providing simultaneously a high acceptance rate. This can be reached by the introduction of artificial momenta P and the evolution of the system according to the dynamics defined by the underlying Hamiltonian. Along these trajectories the energy of the system is (approximately) conserved to enable a high acceptance rate. Since the development of algorithms such as HMC is an own research field in the lattice community, I sketch the main aspects mainly based on [38, 165, 182].
Let us first note that the introduction of artificial momenta P does not change the expectation values of observables of interest:

$$\langle O \rangle = \frac{\int \mathcal{D}U \mathrm{det}M e^{-S}\, O}{\int \mathcal{D}U \mathrm{det}M e^{-S}} \tag{3.125a}$$

$$= \frac{\int \mathcal{D}U\mathcal{D}P\ \mathrm{det}M e^{-S-P^2/2}\, O}{\int \mathcal{D}U\mathcal{D}P\ \mathrm{det}M e^{-S-P^2/2}}. \tag{3.125b}$$

We start with the main concepts of HMC algorithms for actions with an even number of degenerative flavors

$$S[U] = S_G[U] - \bar{\psi}(M^\dagger M)\psi, \tag{3.126}$$

which gives $(\mathrm{det}M)^2$ as a weight factor. At the end we extend this discussion to the case of rooted determinants as needed for staggered fermions. With

$$\int \mathcal{D}\bar{\psi}\mathcal{D}\psi e^{-\bar{\psi}M\psi} = \mathrm{det}M = \pi^{-N} \int \mathcal{D}\phi_R \mathcal{D}\phi_I e^{-\phi^\dagger M^{-1}\phi}, \tag{3.127}$$

we can rewrite Eq. (3.126) as

$$S[U] = S_G[U] - \phi^\dagger (M^\dagger M)^{-1}\phi, \tag{3.128}$$

which results in an irrelevant constant factor that cancels in the calculation of expectation values. Using a set N_ϕ of the so-called pseudofermions $\phi = \phi_R + i\phi_I$, which are conventionally chosen to be Gaussian distributed $p(\phi) = e^{-\phi^\dagger\phi}$, we can calculate the determinant stochastically [165]

$$(\mathrm{det}M)^2 = \left\langle \frac{e^{-\phi^\dagger (M^\dagger M)^{-1}\phi}}{p(\phi)} \right\rangle_{p(\phi)} = \frac{1}{N_\phi} \sum_{k=1}^{N_\phi} \frac{e^{-\phi_k^\dagger (M^\dagger M)^{-1}\phi_k}}{p(\phi_k)} + \mathcal{O}(1/\sqrt{N_\phi}). \tag{3.129}$$

In the case of the SU(3) gauge group, we can express each link as

$$U_\mu(n) = e^{i\sum_{k=1}^{8} \omega_\mu^k(n) T_k} := e^{iQ_\mu(n)}. \tag{3.130}$$

To every "coordinate" Q_μ corresponds the momentum

$$P_\mu(n) = \sum_{k=1}^{8} P_\mu^k(n) T_k, \tag{3.131}$$

for which P^2 in the Hamiltonian is replaced by $\sum_{n,\mu} \mathrm{tr} P_\mu^2(n)$. In this representation P_μ^k and $\omega_\mu^k(n)$ are the conjugate variables. The generators T_k are the same as used in the QCD Lagrangian.
The HMC steps are:

1. Generate χ with normal distribution to obtain the pseudofermion fields $\phi = M^\dagger \chi$.

2. Generate $P_\mu(n)$ whereby the components P^k are normally distributed.

3. Evolve the system according to Hamilton equations of motion [165]

$$\dot{\omega_k} = \frac{\partial H}{\partial P_k} = P_k \qquad \Longrightarrow \dot{U}_\mu(n) = P_\mu(n) U_\mu(n) \tag{3.132}$$

$$\dot{P_k} = -\frac{\partial S}{\partial \omega_k} \qquad \Longrightarrow \dot{P}_\mu(n) = -\frac{\partial S}{\partial Q_\mu(n)} := -F_\mu(n) \tag{3.133}$$

   where the dot stands for the fictitious time derivative. They can be solved via e.g. the leap-frog method whose discretization errors are taken into account in the following accept/reject step.

4. The new set of candidates P' and U' are accepted with a probability of

$$p = \min(1, e^{-\Delta H}) \qquad \Delta H = H(P', U') - H(P, U). \tag{3.134}$$

   as already used in Eq. (3.99).

The crucial and time consuming part is the calculation of the force F_μ informally written as

$$F_\mu(n) = \frac{\partial S(U)}{\partial Q_\mu(n)}. \tag{3.135}$$

We want to calculate the derivative of the scalar function S with respect to Q which is a sum over the generators T_a and real numbers ω_a and hence a Lie-algebra su(3). We can define a possible Lie-derivative of a scalar function $f(U)$ according to [38]

$$\frac{\partial f(U)}{\partial \omega_a} = \frac{\partial}{\partial \omega} \, f(e^{i\omega T_a})\Big|_{\omega=0}. \tag{3.136}$$

The force as the result of a derivative with respect to Q is part of the Lie-algebra su(3) and can be written as

$$F = \frac{\partial S}{\partial Q} = \sum_{a=1}^{8} T_a \frac{\partial S(U)}{\partial \omega_a} \tag{3.137a}$$

$$= \sum_{a=1}^{8} T_a \frac{\partial}{\partial \omega_a} \left(S_G[U] + \phi^\dagger (M^\dagger M)^{-1} \phi \right). \tag{3.137b}$$

Restricting this short discussion to the fermionic part we face terms of the form

$$\frac{\partial}{\partial \omega_a} \left(\phi^\dagger (M^\dagger M)^{-1} \phi \right) = -\left((M^\dagger M)^{-1} \phi \right)^\dagger \left(\frac{\partial M^\dagger}{\partial \omega_a} M + M^\dagger \frac{\partial M}{\partial \omega_a} \right) \left((M^\dagger M)^{-1} \phi \right). \tag{3.138}$$

Computationally demanding is in particular the calculation of the inverse $(M^\dagger M)^{-1}$. Again, due to its enormous size, it is just impractical to calculate it directly. Using the conjugate gradient method $M^\dagger M \phi$ can be calculated efficiently by solving

$$(M^\dagger M)^{-1} \phi = x \Longleftrightarrow M^\dagger M \, x = \phi, \tag{3.139}$$

for x. In the case of staggered fermions, we deal with determinants of the form $(\det M)^{n/4}$. Let us approximate the hermitian matrix $M^\dagger M$ by a sum of rational functions $r(M^\dagger M)$ and rewrite the (pseudo)fermionic action according to

$$S_F = -\phi^\dagger r(M^\dagger M)\phi, \tag{3.140}$$

with

$$r(M^\dagger M) = \alpha_0 + \sum_{k=1}^{m} \frac{\alpha_k}{M^\dagger M + \beta_k}. \tag{3.141}$$

Using the Remez algorithm, the coefficients α_k and β_k can be calculated [183] which remain fixed during the simulation (individually tuned for each quark mass). The accuracy of this rational approximation is determined by m and can be tuned to machine precision. Multi-shift solvers [184] provide an efficient way to invert $M^\dagger M + \beta_k$ for a set of β_k. As a variant of the hybrid monte carlo algorithm, it is referred as rational hybrid monte carlo (RHMC) [183, 185, 186].

4 Upper right corner of the Columbia plot

Exploring the heavy mass regions in the context of the Columbia plot gives us insights into the deconfinement transition of QCD (recall Section 2.5.1). Although there is a clear evidence for a 1^{st} order phase transition in the quenched approximation and a smooth crossover at the physical point, a non-perturbative determination of the critical quark masses is still missing. A better understanding of the upper right corner of the Columbia plot is not only interesting from the theoretical point of view. It opens the possibility to test models such as effective lattice theories [187, 188] or models based on functional approaches [81] which can make predictions at finite baryon density up to small quark masses. The only tool at hand to study QCD from first principles is lattice QCD which can work as a benchmark for these models. Furthermore, the precise knowledge and interplay of the critical parameters such as temperature or quark masses in this region could guide the way towards conditions which are relevant for heavy ion collisions by extrapolating critical surfaces. Moreover, computational strategies employed in the heavy mass region could be helpful to study criticality in the lower mass region, which features higher simulation costs. This motivated us to explore the upper right corner of the Columbia plot by using new algorithmic approaches such as parallel tempering. This method enabled us to study the thermal and topological features of quenched QCD precisely [40, 168] and to pinpoint the critical quark masses on $N_t = 6, 8$ lattices [85].

4.1 Quenched QCD at finite temperature

Simulating the pure gluonic SU(3) gauge theory corresponds to neglecting the sea quark contributions by setting the fermion determinant to one. Although this seems to be a rough approximation to full QCD, it has yielded remarkable results, such as the light hadron spectrum with just 10% deviation of the kaon mass to its experimental value [189]. On the thermodynamic side, pioneering works such as [74] calculated the pressure and energy density up to $5T_c$ and extrapolated them to the continuum. With a Symanzik-improved gauge action, the string tension and equation of state could be calculated with higher precision [190]. In [191] the temperature range was extended up to $1000T_c$. This is usually computationally demanding since the spatial extension N_x has to increase with the temperature to keep the physical volume constant. The challenge was accomplished by investigating finite volume effects especially above T_c, which turned out to be smaller than the statistical errors. This enabled them to connect the high temperature perturbative region with the low temperature non-perturbative region [191].
In this Section we discuss the framework of parallel tempering applied to the deconfinement transition of quenched QCD. In this context we calculated the transition temperature with unreached high precision, classified the transition to be of 1^{st} order and determined the latent heat in the continuum and infinite volume limit. The following Sections are part of our

publications [40, 192]. I refer to Sections 2.3 and 2.5.1 and references to avoid repetitions of the historical outline regarding the deconfinement transition and the discussion of center symmetry breaking.

4.1.1 Observables

QCD in the quenched approximation features a 1$^{\text{st}}$ order phase transition which is driven by the spontaneous breaking of the $\mathcal{Z}_3$ center symmetry. In this case, the Polyakov loop P works as a true order parameter to probe the center symmetry breaking. The discretized version of the Polyakov loop defined in Eq. (2.13) reads

$$P = \frac{1}{N_s^3 N_c} \sum_{\vec{x}} P_{\vec{x}} = \frac{1}{N_s^3 N_c} \sum_{\vec{x}} \text{tr} \left[\prod_{\tau} U_4(\vec{x}, \tau) \right], \tag{4.1}$$

where N_s stands for the spatial extension of the lattice, $\vec{x}$ and τ indicate the spatial and temporal position respectively and $N_c = 3$ corresponds to the number of colors. In the case of a 1$^{\text{st}}$ order phase transition the Polyakov loop should show a discontinuity at the critical coupling β_c in the thermodynamic limit, whereby its susceptibility χ diverges linearly with the physical volume. For a 2$^{\text{nd}}$ order phase transition this behavior is accompanied by critical exponents. Hence, analyzing the peak of the susceptibility determines the type of phase transition and the corresponding transition temperature T_c (coupling β_c). Another way to extract β_c is the zero-crossing of the third-order Binder cumulant b_3 of the absolute value of the Polyakov loop. The susceptibility and the Binder cumulant are defined as

$$\chi = N_s^3 \left(\langle |P|^2 \rangle - \langle |P| \rangle^2 \right), \qquad b_3 = \frac{\langle (|P| - \langle |P| \rangle)^3 \rangle}{\langle (|P| - \langle |P| \rangle)^2 \rangle^{3/2}}. \tag{4.2}$$

The third Binder cumulant b_3 works as a measure of the skewness of the distribution of $|P|$.

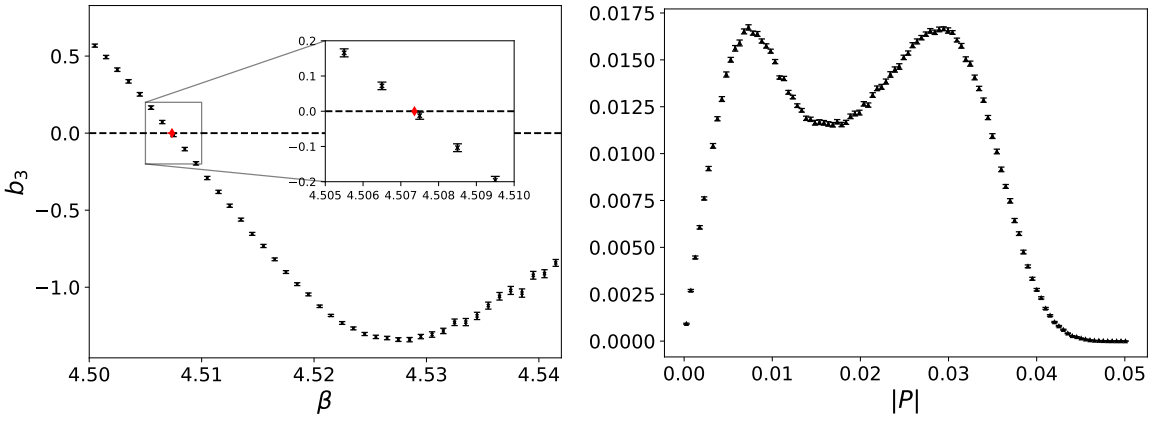

Figure 4.1: Left: b_3 as function of β exemplary shown for $32^3 \times 8$ reweighted via the correlated multiple histogram method to $b_3 = 0$ (red point) to obtain the critical coupling. Right: Normalized histogram of $\langle |P| \rangle$ which is reweighted to β_c defined by $b_3 = 0$ for $32^3 \times 8$. The error on the bins are jackknife errors.

Simulating far away from β_c, i.e. where the system is deep in one phase, there is a single (Gaussian-) peak in the distribution. As one comes closer and closer to the critical coupling, a second peak evolves which corresponds to the 2$^{\text{nd}}$ phase of the system. As soon as β_c is

reached, both peaks have the same shape and the distribution is completely symmetric which leads to a vanishing skewness. The left panel of Fig. 4.1 shows the Binder cumulant b_3 which is reweighted via the correlated multiple histogram method to $b_3 = 0$ (red point) to obtain β_c. The corresponding normalized and reweighted Polyakov loop histogram is presented on the right panel, which clearly shows a double peak structure, indicating the presence of both phases. Strictly speaking, there are no phases in finite systems; here we loosely use the word phase to describe the (de-)confined regimes. In the infinite volume limit, defining β_c by the peak of the susceptibility or vanishing b_3 should be equivalent. Both results have to agree in the thermodynamic limit since the peak of χ diverges linearly, the width vanishes linearly and the slope of b_3 (close to β_c) increases linearly with the volume. To compare results at different lattice spacings, the susceptibility should be renormalized to extract the coupling β_χ at which it peaks. This is obviously not necessary for the zero-crossing of b_3, whose corresponding coupling is labeled as β_b. The renormalization procedure for χ works as follows:

$$\chi_R(\beta, N_x, N_t) = Z^{N_t}(\beta)\chi(\beta, N_x, N_t), \tag{4.3}$$

$$\chi_R(\beta_b, 4N_t, N_t) = Z^{N_t}(\beta_b)\chi(\beta, 4N_t, N_t) := 1. \tag{4.4}$$

This implies that $\chi_R(\beta_b) = 1 \ \forall \ LT = 4$. It is not strictly necessary to renormalize the susceptibility in order to extract β_c. As the width of the bare peak decreases linearly with the inverse volume, $Z(\beta)$ becomes approximately constant across that width, and so the difference between β_χ of $\chi(\beta)$ and β_χ of $\chi_R(\beta)$ should go to zero in the infinite volume limit. Thus, the value of β_c extracted from $\chi(\beta)$ should agree with the value of β_c extracted from $\chi_R(\beta)$.

4.1.2 Parallel tempering to improve on supercritical slowing down

Supercritical slowing down is a phenomenon which appears in simulations of 1^{st} order phase transitions, associated with high auto-correlation times. We illustrate its appearance in quenched QCD where the Polyakov loop populates three distinct degenerate deconfined and one confined center sector. Right at β_c, both phases are present in a finite volume as presented in the left panel of Fig. 4.2. The configurations around the origin correspond to the confined phase and those located around the three sectors belong to the deconfined phase. Let us change the view and look at the effective potential defined as $V = -\log(\langle|P|\rangle)$ which shows two minima (right panel of Fig. 4.2). In contrast to the thermodynamic limit, the confined and deconfined phase are not completely separated. In a finite volume a temperature range around T_c exists, in which the system can be in both phases and tunnel between them. These states are split by the energy ΔE, which scales with volume V. Since both phases have to be sampled, this gets more severe as V is increased. One can see that the barrier between the two phases increases with the volume. The consequence of this is a high auto-correlation time if tunneling is not sampled, since the system tends to stick in one phase. Parallel tempering is a suitable method to overcome these problems. It reduces the auto-correlation time within the sub-ensembles, since they gather contributions of the other ensembles at different couplings. Hence both phases of the system around β_c can be sampled. For the parallel tempering to be effective, the acceptance rate of swapping updates must be carefully controlled, such that the action distributions of neighboring ensembles have a substantial overlap. This can be achieved through the control of the distance of the parameter sets p_i, which, thus, have to move closer to each other as the physical volume increases. This is easily satisfied if the number of streams in the transition region is kept constant as the width of the

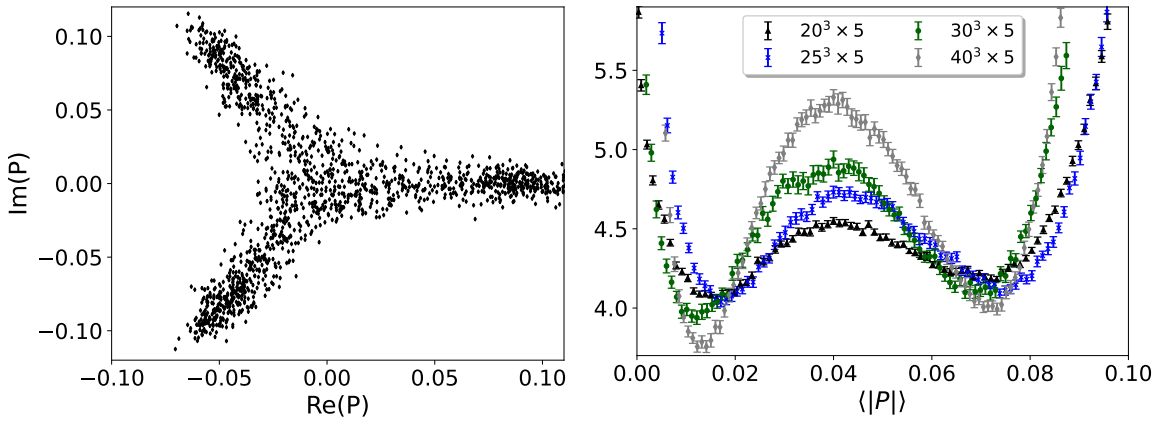

Figure 4.2: Left: Real and imaginary part of the Polyakov loop at β_c for $32^3 \times 8$. Every 1000th configuration is shown. Right: Effective potential of the absolute value of the Polyakov loop for various volumes in quenched QCD, after employing parallel tempering. The barrier between the phases increases with the volume.

transition region scales with inverse volume. Typically, we have simulations at 16-256 β values and introduce swapping updates at predefined points in the Markov chain (typically after 5 sweeps in each sub-ensemble). This algorithm can be especially efficiently parallelized in our case where the β dependence of the action is simply given as an overall factor of some function of the link variables. We set up a number of streams updating a configuration at certain β values (typically we use equidistant points). After 5 sweeps on their configuration, all the streams need to communicate one number (their action) to a master node which proposes (and accepts or rejects) several swapping updates for each stream, and afterwards informs each stream which β value they ended up at. This means that the network bandwidth and computational requirements for the swapping updates are negligible, although some efficiency is lost as synchronization between the streams is required.
In Fig. 4.3 we show the β history of two streams (out of 128) for a simulation on a $45^3 \times 10$ lattice. As one observes the streams follow a trajectory similar to a random walk on the allowed β range and they visit all points for a long enough simulation. The value of the Polyakov loop changes relatively slowly during the history of the stream. If we look at the history of the Polyakov loop for a given β, the largest auto-correlation comes from the instances when the same stream contributes (even if the stream visited other β values in the meantime). We therefore reorder the Monte Carlo chain using the stream ID number of the contributions (and keep the chronological order among contributions from each stream). This ensures that the most correlated contributions will be close to each other (i.e. this ordering results in the largest auto-correlation for the given Monte Carlo chain), which helps to minimize the correlations between blocks in the jackknife analysis. For parallel tempering simulations the distance between neighboring ensembles $\Delta\beta$ and their total number n play a crucial role. Increasing $\Delta\beta$ suppresses the probability to swap configurations and the ensembles collect more contributions from their neighbors until they "decouple" and run as independent simulations. For a suitable acceptance rate of swapping updates, the action distributions of neighboring ensembles should clearly overlap, which can be obtained by tuning n and $\Delta\beta$. In Fig. 4.4 the auto-correlation time of the Polyakov loop for different sets of parallel tempering simulations is compared to standard methods. As one observes, the auto-correlation is substantially smaller for the parallel tempering simulations, despite at the

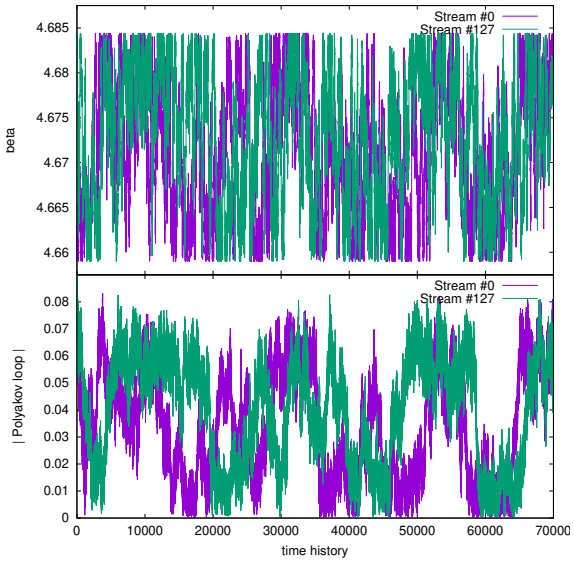

Figure 4.3: The β history (above) and Polyakov loop average (below) of 2 streams as a function of the Monte Carlo sweeps in a simulation on a $48^3 \times 10$ lattice with 128 streams on the range $4.659 \leq \beta \leq 4.6844$ divided equidistantly.

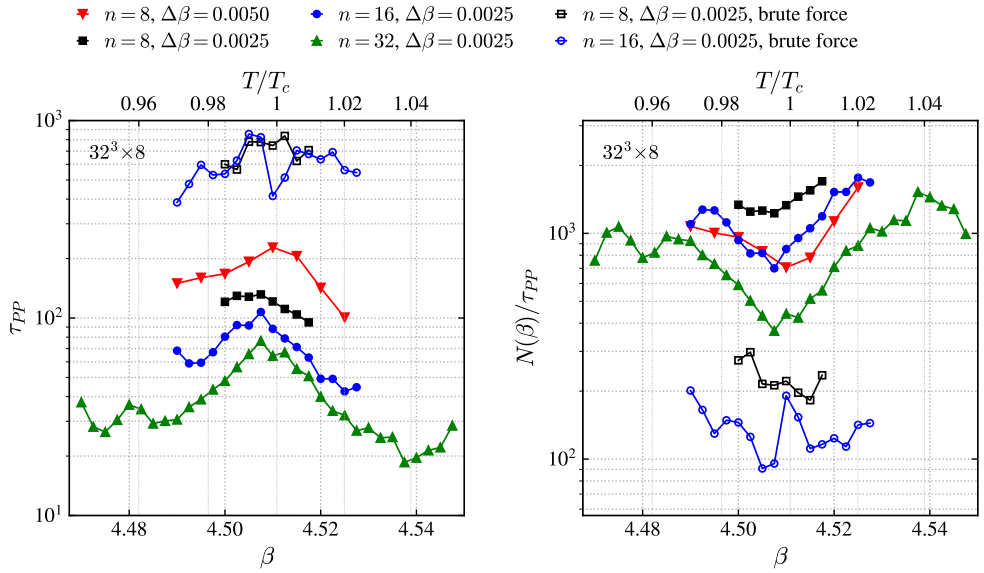

Figure 4.4: Left panel: Auto-correlation time of the Polyakov loop as a function of the coupling β on a $32^3 \times 8$ lattice using parallel tempering (filled points) and brute force simulations (unfilled points) with the same amount of computer time. $\Delta\beta$ indicates the $\beta-$spacing between the sub-ensembles and n stands for the total number of them. Right panel: Number of computed updates divided by the auto-correlation time as a function of β.

increased cost of being forced to simulate several β values. In the right panel of Fig. 4.4 we show the number of configurations created in brute force and in parallel tempering simulations at similar parameters, using the same amount of computer time. The auto-correlation time improves tremendously as the number of β values increases and as $\Delta\beta$ decreases (increasing the acceptance rate of swap updates). The red and black points indicate that the number of independent configurations created by the tempering algorithm increases substantially by simply decreasing $\Delta\beta$. Increasing the density of β values, as between the red and blue points, results in nearly the same efficiency, indicating that the decrease in the number of updates (due to having twice as many streams for the same computer time) scales roughly with the decrease in the auto-correlation time. In Fig. 4.5 the advantages of parallel tempering

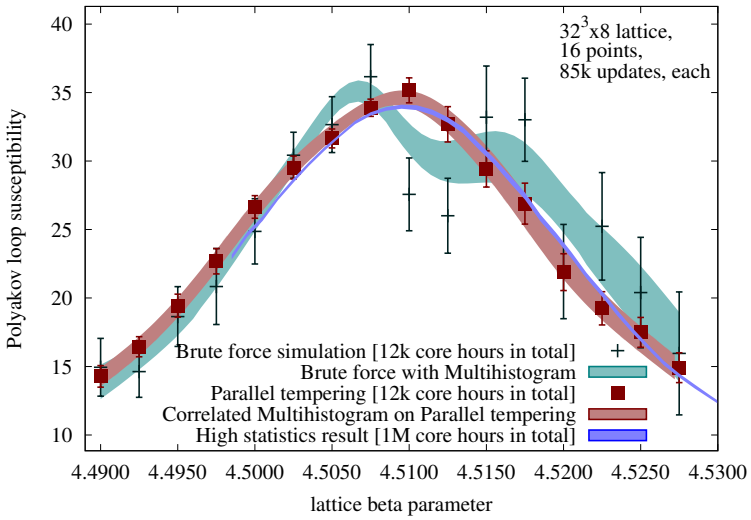

Figure 4.5: Polyakov loop susceptibility as a function of the coupling β in quenched QCD on a $32^3 \times 8$ lattice. The red squares correspond to parallel tempering simulations and the red band indicates the interpolation between them obtained with the correlated multiple histogram method.

compared to standard brute force simulations are clearly visible. With the same amount of computer time, the statistical errors of the tempering results are smaller and describe much better a high statistic result, especially close to β_c. The uncorrelated multiple histogram method is used for the brute force simulations and the parallel tempering simulations are interpolated with the correlated version of this method. In practice, the correlations between ensembles are quite small. Neglecting these correlations in the multiple histogram procedure causes a negligible change in the results (much smaller than the statistical errors).

4.1.3 Transition temperature

To relate the action-dependent value of the coupling β at the transition to a more generic transition temperature, it is necessary to set the scale. We use w_0 based on the Wilson flow (recall Section 3.2.4). We compute the w_0 scale in lattice units (w_0/a) for many values of β for two different discretizations of the flow (WSC and SSC). See [193] for notation and further information. This gives us another systematic choice as to which version of the scale setting to use. We then interpolate these results to get $w_0/a(\beta)$ by fitting with polynomials of order 6 and 7 in the β range $[4.0, 4.95]$. It is critical to ensure that finite volume effects on

the w_0 scale remain small, as these effects increase with the flow time. At zero temperature, we performed a volume study for w_0/a as a function of L/w_0, where L denotes the spatial extent of the box. Fluctuations in w_0/a are comparable in size to the statistical error at each volume; consequently, no significant volume dependence was found. Now we can convert $w_0/a(\beta)$ into a transition temperature for β_χ or β_b via

$$\frac{w_0}{aN_t} = w_0 T. \tag{4.5}$$

To compute the continuum value of the transition temperature $w_0 T_c$ in the infinite volume limit, we first find the continuum value of $w_0 T_c$ at finite volume and fixed lattice aspect ratio $LT = N_s/N_t$ and then extrapolate the results of the continuum theory at different LT to the limit where $(LT)^3 \to \infty$. In Fig. 4.6 an exemplary continuum extrapolation for $w_0 T_c$ defined

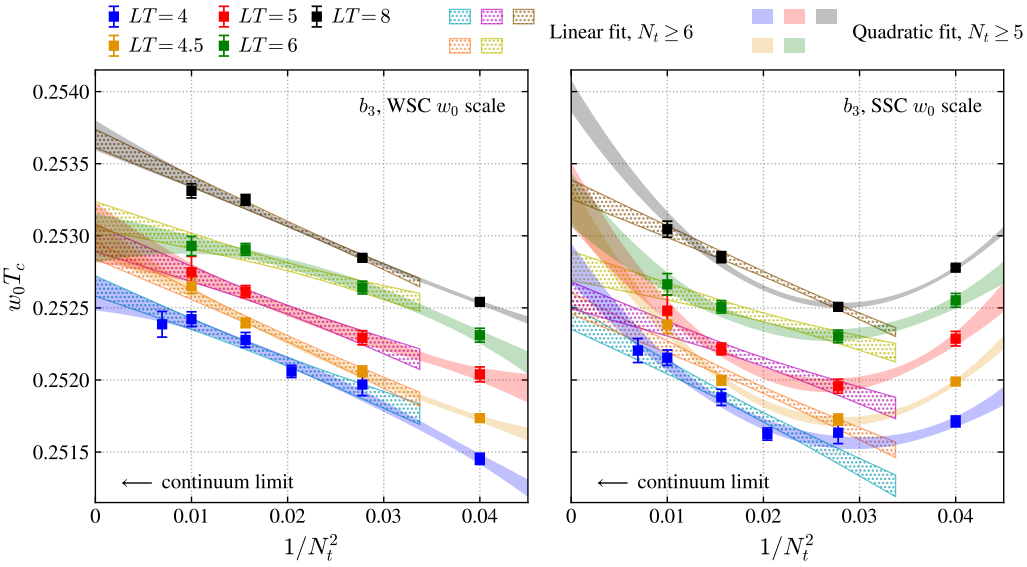

Figure 4.6: Exemplary continuum extrapolation of $w_0 T_c$ defined by β_b for various volumes LT. Left: Using WSC w_0 scale. Right: Using SSC w_0 scale. Each data point is the median value of $w_0 T_c$ computed for that lattice from the systematic analysis, and the error bars give the combined statistical and systematic error. Error bands are shown for the two kinds of extrapolating fit that are used: a linear fit to lattices with $6 \leq N_t$, and a quadratic fit to lattices with $5 \leq N_t$. The error bands give the combined statistical and systematic error from all similar fits performed in the analysis.

by β_b is shown for two different flow discretizations. We use large lattices with aspect ratios $LT = 4$, 4.5, 5, 6, and 8 for four different temporal extensions: $N_t = 5$, 6, 8, and 10. To check the consistency of the continuum extrapolation at other temporal extensions, we also include two lattices with $N_t = 7$ and 12 in the $LT = 4$ extrapolation. In the left panel of Fig. 4.6, one can see that $w_0 T_c$ goes roughly linearly with N_t^{-2} for each LT. We perform two types of fits to extrapolate to the continuum: a linear fit to all lattices with $N_t \geq 6$, and a quadratic fit to all lattices with $N_t \geq 5$. The fits are shown in Fig. 4.6; the error bands give the combined statistical and systematic errors from all the similar fits performed in the analysis.
The continuum results from χ_R and b_3 are shown in Fig. 4.7 as functions of $(LT)^{-3}$. A quadratic fit to $LT \geq 4$ is used to extrapolate to the infinite volume limit. This fit is shown

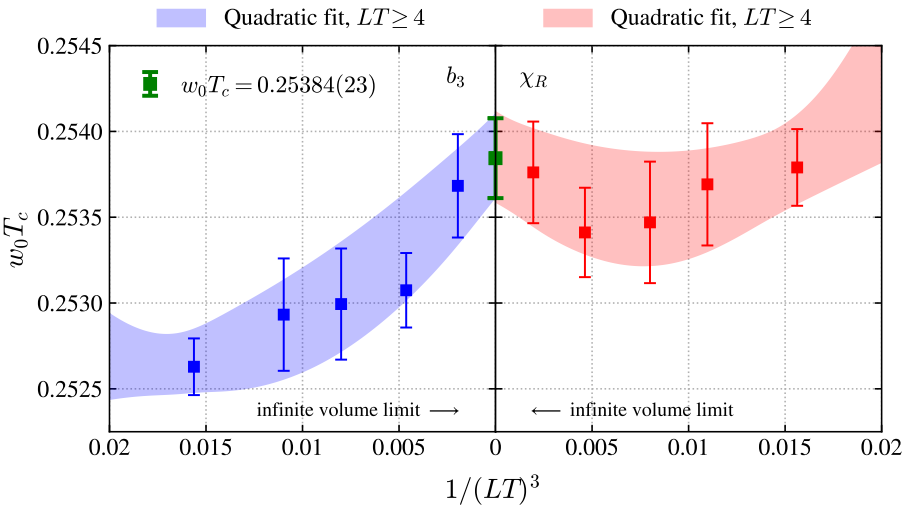

Figure 4.7: Infinite volume extrapolation of the continuum $w_0 T_c$. Left: Using the zero-crossing of b_3. Right: Using the peak of χ_R. Each point is the median value of $w_0 T_c$ computed for each aspect ratio LT in the systematic analysis, and the error bars give the combined statistical and systematic error. Error bands are shown for the quadratic fit to $LT \geq 4$. The error bands give the combined statistical and systematic errors from all similar fits in the analysis. The extrapolations from b_3 and χ_R are in agreement, as expected. The final result, $w_0 T_c = 0.25384(23)$, is shown in green.

in Fig. 4.7 for both χ_R and b_3. The error bands give the combined statistical and systematic errors from all the similar fits that were performed. We find that the infinite volume value of the transition temperature $w_0 T_c$ computed using χ_R agrees with the value computed using b_3, as expected. Following the analysis method introduced in [153] (and see detailed description in [126]) to estimate the statistical and systematic uncertainties of the results, in total we have performed 256 different analyses, characterized by the choice of the moment of the Polyakov loop (χ_R or b_3), the degree of the fit to the moment (3, 4, 5 or 6), whether and how the fit is correlated (uncorrelated or correlated with an eigenvalue cutoff of 10%, 5%, 1%), the choice of the w_0 scale calculation (WSC, SSC), the degree of the fit to the w_0 scale data (6 or 7), and the degree and range of the continuum extrapolation (linear or quadratic). The statistical and systematic uncertainties are synthesized into a CDF defined by

$$F(w_0 T_c) = \frac{1}{2} + \frac{1}{2 \cdot 256} \sum_{i=1}^{256} w_i \operatorname{erf}\left(\frac{w_0 T_c - \mu_i}{\sqrt{2}\sigma_i} \right), \tag{4.6}$$

where μ_i and σ_i are the central value and statistical uncertainty respectively of the ith analysis, and w_i is the weight of the CDF of the ith result. (This equation then assumes that the statistical result of each analysis is well-described by a normal distribution with a mean of μ_i and standard deviation of σ_i). We have no prior assumptions as to the relative statistical significance of any of the analyses, and so we take an agnostic position by weighting all analyses equally, i.e. by setting $w_i = 1$. The final result is then the median value of the CDF, implicitly defined by $F(w_0 T_c) = 0.5$, and the central 68% width is taken as twice the

total error. This yields a final value of $w_0 T_c = 0.25384(23)$ - the first per-mill accurate result

Table 4.1: Error budget of $w_0 T_c$.

median	0.25384	
statistical error	0.00011	0.043 %
full systematic error	0.00021	0.082 %
Observable (b_3 , χ_R)	$1.1 \cdot 10^{-5}$	0.0042 %
Fit order (3, 4, 5, 6)	$2.1 \cdot 10^{-5}$	0.0085 %
Fit type (corr, uncorr)	$1.2 \cdot 10^{-5}$	0.0047 %
Scale setting (WSC, SSC)	$1.9 \cdot 10^{-5}$	0.0075 %
Scale fit order (6, 7)	$2.4 \cdot 10^{-6}$	0.0010 %
Continuum limit range	$1.2 \cdot 10^{-4}$	0.0487 %

in QCD thermodynamics. The error budget is presented in Table 4.1.

4.1.4 Volume scaling and identifying the order of phase transition

Following the renormalization scheme described in Section 4.1.1 for χ_R, we can classify the order of phase transition by investigating the volume scaling of continuum extrapolated results. We select fixed physical volumes ($LT = 4.5, 5, 6, 8$) and interpolate $Z(\beta)$ to the actual volume dependent β_c of each simulation with $N_t = 5, 6, 8$ and 10. The renormalized result $\chi_R(L,T) = Z^{N_t}(\beta)\chi(\beta, N_x, N_t)$ is continuum extrapolated at fixed volume. Continuum extrapolated results are shown in Fig. 4.8 for the $\chi_R(w_0 T)$ curves at fixed volume, and in Fig. 4.9 for the inverse peak height. In Fig. 4.8 (left), each curve is continuum extrapolated

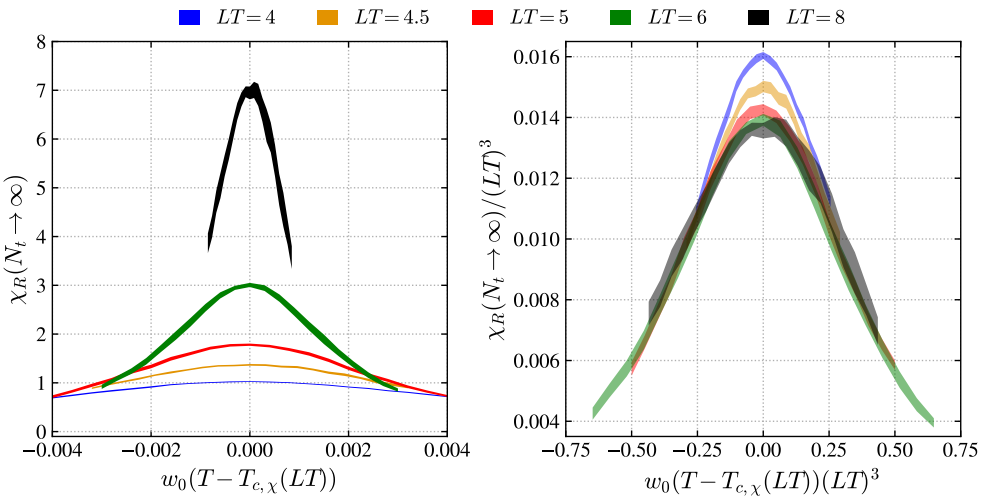

Figure 4.8: Left: Continuum extrapolated renormalized Polyakov loop susceptibility at different volumes, centered around the volume-dependent peak position $w_0 T_{c,\chi}(LT)$. The bands include both statistic and systematic uncertainties. Right: Same curves as in the left panel, but scaled with appropriate powers of the volume, in order to highlight the linear volume dependence typical for a 1$^{\text{st}}$ order transition.

at the indicated fixed volume, and the bands include both statistic and systematic uncertainties. Note that, had we subtracted the infinite volume limit value $w_0 T_c$ instead of the

volume-dependent values $w_0 T_{c,\chi}(LT)$, the curves would not have have been exactly centered around zero, but a trend would have appeared where larger volumes would peak closer to zero. However, as can be seen in the right panel of Fig. 4.7, the difference would be negligible, since the continuum extrapolated peak position shows a very mild volume dependence. The right panel of Fig. 4.8 shows the same curves as in the left panel, but scaled with the volume in order to highlight the volume dependence. We can see that the bands corresponding to $LT = 5, 6, 8$ are almost indistinguishable, clearly showing that they fall in the linear volume scaling regime typical of a 1^{st} order transition.

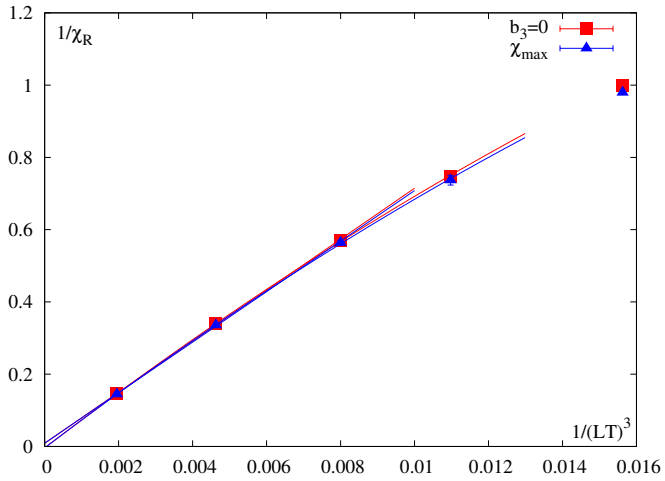

Figure 4.9: Infinite volume extrapolation of the inverse Polyakov loop susceptibility. The results are renormalized and continuum extrapolated, systematic errors are included. We use red symbols if we defined T_c by the zero of b_3 and blue symbols by the peak of χ_R. The linear scaling sets in for $5 \leq LT$.

In Fig. 4.9 we actually show two extrapolations, one for each definition of T_c, using the zero of the third Binder cumulant or the susceptibility peak in red and blue, respectively. The extrapolations do not differ at all depending on this ambiguity and the main systematic uncertainty comes from the possibility to include a inverse quadratic volume term in the infinite volume extrapolations. We find that the inverse susceptibility is extrapolated to be vanishing, (or, actually, strongly constrained: $\chi_R^{-1}(V = \infty) = 0.0023(58)_{\text{stat}}(65)_{\text{sys}}$) in the infinite volume limit. In this context, let us discuss another observable, which can be used to identify the order of phase transition. The fourth standardized moment b_4 (compare to Eq. (4.2))

$$b_4 = \frac{\langle (|P| - \langle |P| \rangle)^4 \rangle}{\langle (|P| - \langle |P| \rangle)^2 \rangle^2}, \tag{4.7}$$

serves as a measure of the kurtosis of a distribution. Depending on the type of phase transition, it takes on $b_4 = 3$ for a crossover (Gaussian distribution), $b_4 = 1$ for a 1^{st} order and $b_4 = 1.604$ for a 2^{nd} order Z_2 phase transition [84]. We could observe that b_4 is nearly constant for volumes up to $LT = 5$ and only mildly drops for the largest volumes $LT = 6, 8$ (see left panel of Fig. 4.10). This is in contrast to the volume scaling of the peak of the susceptibility (right panel) for which the expected linear scaling sets in for $LT \geq 5$.

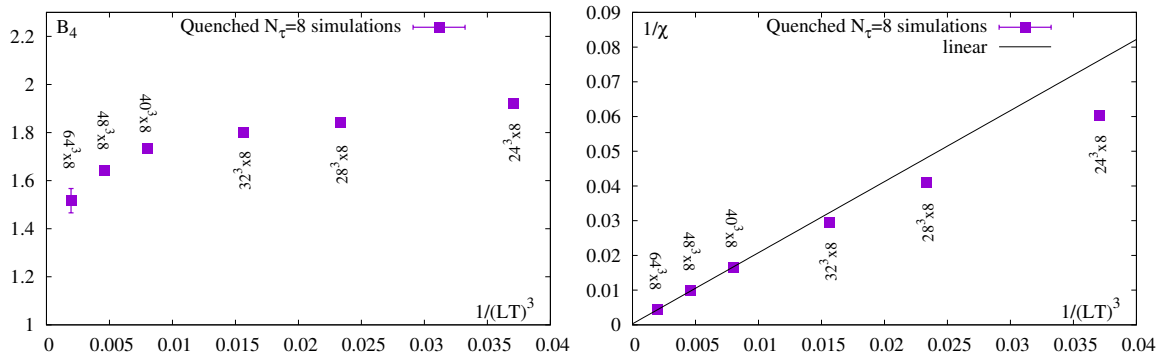

Figure 4.10: Volume scaling of b_4 (left panel) and peak of the bare Polyakov susceptibility (right panel) for $N_t = 8$.

4.1.5 Latent heat

A key feature of a 1$^{\text{st}}$ order phase transition is a non-vanishing latent heat. This quantity can be understood as the discontinuity of the trace anomaly I/T^4

$$\frac{I}{T^4} = \frac{\epsilon - 3p}{T^4}, \tag{4.8}$$

and hence of the energy density ϵ, as the transition is crossed. The trace anomaly is a measure of the deviation from an ideal/scale invariant system and can be calculated according to

$$\begin{aligned}
\epsilon - 3p &= \frac{T^2}{V}\partial_T \log Z - 3p && \text{(4.9a)}\\
&= \frac{T^2}{V}\partial_T \left(\frac{pV}{T}\right) - 3p && \text{(4.9b)}\\
&= T^2\left(-\frac{p}{T^2} + \frac{1}{T}\partial_T p\right) - 3p && \text{(4.9c)}\\
&= T\partial_T p - 4p && \text{(4.9d)}\\
&= T^5 \partial_T \left(\frac{p}{T^4}\right) && \text{(4.9e)}\\
&= T^5 \partial_T \left(-\frac{f}{T^4}\right). && \text{(4.9f)}
\end{aligned}$$

In the first line we used the standard definitions of the thermodynamical quantities in statistical mechanics: $\epsilon = T^2/V\partial_T \log Z$ and assume large volumes such that $p = T\partial_V \log Z \approx T\frac{\log Z}{V}$. Using the lattice extensions with $\frac{1}{T^3 V} = \frac{N_t^3}{N_x^3}$, we can rewrite

$$\begin{aligned}
\frac{f}{T^4} = -\frac{1}{T^4 V} T \log Z &= -\frac{1}{T^3 V}\int \mathrm{d}\beta' \left[S_0^{\text{per site}} - S_T^{\text{per site}}\right] && \text{(4.10a)}\\
&= -N_t^4 \int \mathrm{d}\beta' \left[S_0 - S_T\right], && \text{(4.10b)}
\end{aligned}$$

and get the final expression for the trace anomaly according to

$$\frac{I}{T^4} = \frac{\epsilon - 3p}{T^4} = T\partial_T \left(-\frac{f}{T^4}\right) \tag{4.11a}$$

$$= N_t^4 T \frac{\partial \beta}{\partial T} \left[S_0 - S_T\right] \tag{4.11b}$$

$$= -N_t^4 a \frac{\partial \beta}{\partial a} \left[S_0 - S_T\right]. \tag{4.11c}$$

Here the gauge action at finite temperature S_T is renormalized with the action at zero temperature S_0 according to the scheme provided by [74]. Calculating the jump of the trace anomaly is a challenging task. We face a pronounced temperature dependence just above and just below T_c (see left panel of Fig. 4.11). The most successful method to define the

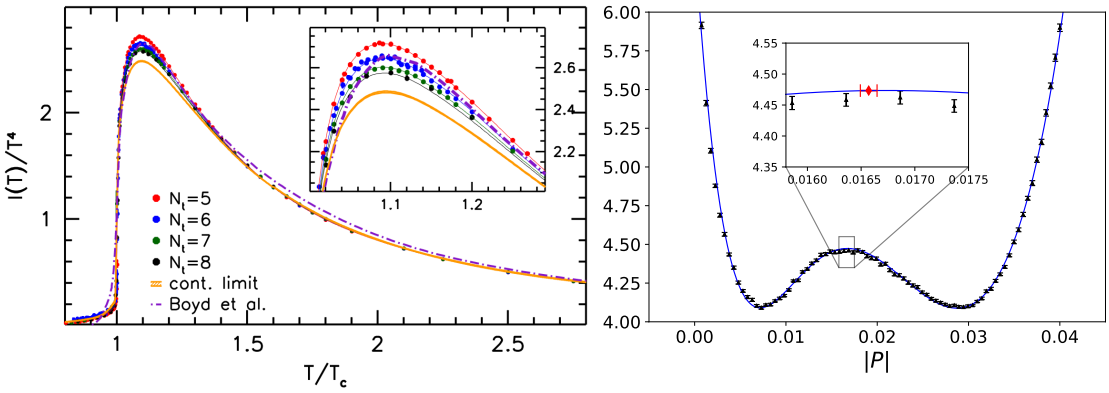

Figure 4.11: Left: Trace anomaly for $LT = 8$ volumes and various spacings as function of the temperature. Plot from [191]. Right: Exemplary presentation of the cut determination for $32^3 \times 8$. The effective potential at β_c is fit with a polynomial to determine the minimum between both peaks which serves as a cut (red point).

latent heat, the one we also use here, is to simulate right at β_c and classify the lattice configurations into the cold and hot phases [75, 76]. The procedure works as follows: We reweight our closest ensemble to β_c right to the critical coupling and calculate the minimum between the two peaks of the $|P|$ histogram (see right panel of Fig. 4.11). This minimum gives us a cut between the hot and the cold phases of the system. Then the trace anomaly is calculated for configurations whose $|P|$ is above and below the cut yielding

$$\frac{\Delta E}{T^4} := \Delta \frac{\epsilon - 3p}{T^4} = N_t^4 T \frac{\partial \beta}{\partial T} \left[S_{\text{cold}} - S_{\text{hot}}\right]. \tag{4.12}$$

To calculate $T\frac{\partial \beta}{\partial T}$, we can use $f(\beta) := w_0/a(\beta)$ by

$$-T\frac{\partial \beta}{\partial T} = a\frac{\partial \beta}{\partial a} = \frac{f(\beta)}{\frac{\partial f(\beta)}{\partial \beta}}. \tag{4.13}$$

$f(\beta)$ is a polynomial of deg=6,7 as described in the previous Section. In Fig. 4.12 the bare Polyakov loop histograms are shown for three volumes of our $N_t = 5$ lattice set. Standard jackknife errors are shown on the histograms. The trace anomaly shows no discontinuity between the phases and its Polyakov loop dependence can be modeled by a polynomial. We fit a 3^{rd} order polynomial with finite volume corrections proportional to $1/L^3$ to obtain the

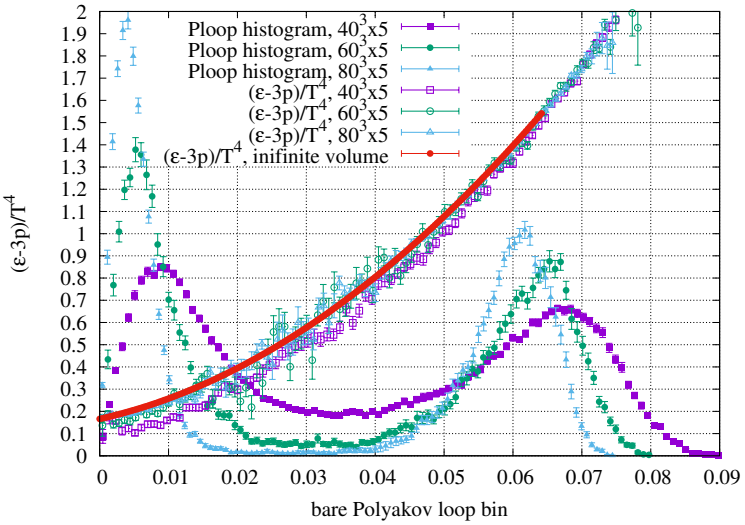

Figure 4.12: Polyakov loop histograms for three volumes on $N_t = 5$ along with the trace anomaly expectation values for each Polyakov loop bin. The double peak structure and the sharpening of the peaks with increasing volume match our expectations for a 1^{st} order transition. The trace anomaly shows no discontinuity in this representation, hence the infinite volume limit can be found using a polynomial model.

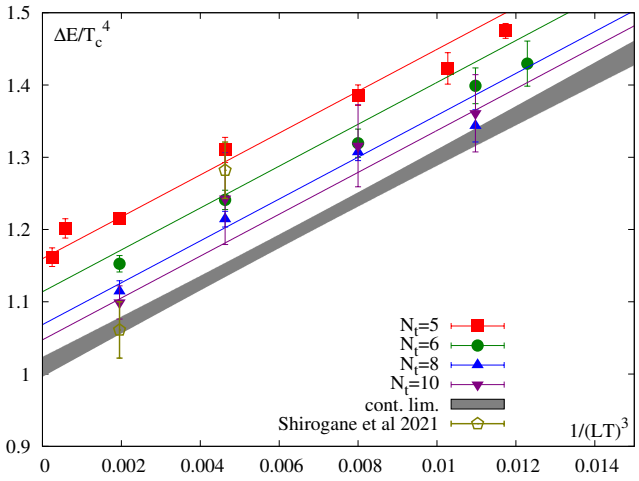

Figure 4.13: Combined infinite volume and continuum limit of the latent heat according to Eq. (4.12). The extrapolation is linear both in $1/N_t^2$ and $1/L^3$, in this example we exclude all ensembles with $N_t < 6$ or $LT < 5$. The continuum extrapolated but finite volume results of [75] are shown for comparison.

infinite volume extrapolation (red curve). This picture connects the latent heat with the hot-phase value of Polyakov loop. The cold phase peak moves to zero as $1/L^3$, hence, the $y-$intercept of the red curve points to the trace anomaly at $T_c - \epsilon$. Similarly, the non-trivial position of the second histogram peak in the thermodynamic limit is translated by the same curve to the trace anomaly at $T_c + \epsilon$. We calculated the latent heat according to Eq. (4.12) and found that a combined linear continuum and infinite volume fit is possible as presented in Fig. 4.13. For the final result we consider the following sources of systematic

uncertainties. The continuum limit is calculated both using and not using $N_t = 5$, including or not including the aspect ratio $LT = 4.5$ into the infinite volume extrapolation. We use various number of Polyakov bins (100, 200 or 400) and two different log-polynomial models for fitting the negative logarithm of the histogram so that the cut value separating the phases can be calculated. We have performed two separate analyses: first using reweighting to β_c from the closest available β ensemble, second, using the multihistogram method to calculate averages at β_c. The final results is shown Table 4.2. The small but clearly non-vanishing

Table 4.2: Final result of the latent heat in the continuum and infinite volume limit.

median	1.0249	
statistical error	0.021	2.1 %
full systematic error	0.027	2.7 %
Histogram fitting	0.0030	0.29 %
Histogram binning	0.0002	0.02 %
β_c definition	0.0135	1.32 %
w_0 interpolation	0.0007	0.07 %
LT range	0.0121	1.18%
N_t range	0.0157	1.53%
Analysis method	0.0019	0.18%

value of the latent heat highlights that the thermal transition in quenched QCD is a weak 1^{st} order transition in the context of SU(N) theories [77]. The major driver of the systematic error is the definition of β_c and the selection of N_t ensembles to the continuum limit which contribute 1.32% and 1.53% to the error.

4.2 Topological features of the deconfinement transition

Let us briefly recall some aspects of Section 2.4 to highlight the motivation to study the topological features of QCD, as they are not only interesting from a theoretical point of view. The corresponding topological susceptibility is relevant in cosmology as part of a potential solution to the strong CP problem: QCD suffers from a fine tuning problem. Its Lagrangian could contain terms of the form

$$\mathcal{L}_\theta = -i\theta q(x), \tag{4.14}$$

which break the CP symmetry unless $\theta = 0$ (or precisely $\theta = n \cdot 2\pi$ with $n \in \mathbb{Z}$). Here $q(x)$ denotes the topological charge density. The Peccei-Quinn mechanism provides an attractive solution to this problem by proposing an additional field, the dark matter candidate called axion $A(x)$, which couples to the gauge fields and obeys a U(1) symmetry. The dynamical breaking of the latter leads to a non-vanishing expectation value of the axion field $\theta + \langle A \rangle / f = 0$, and hence to a mass generation $m_A^2 = \chi / f^2$, which is determined by the topological susceptibility χ [194, 195]. Moreover, the θ dependence of quenched QCD is also relevant in phenomenology by predicting the mass of the η'. As shown by Witten [60] in the large N limit (N is the number of colors), the corresponding free energy must be a multibranched function of θ/N, which has a non-vanishing θ dependence at leading order in $1/N$ [196]. Hence in the confined phase, there is a spontaneous breaking of the CP symmetry at $\theta = (2n+1)\pi$ due to the system's choice for one branch. At these points a 1^{st} order phase transition is expected since two branches with opposite derivatives intercept there. This leads to another possible phase diagram of quenched QCD depending on θ. I refer to [196] for further information.
Because the free energy density is an even function of θ due to the $\theta \to -\theta$ symmetry, we can expand it in θ as

$$f(\theta) = f(0) + \frac{1}{2}\chi\theta^2 + \frac{1}{4!}\chi_4\theta^4 + \mathcal{O}(\theta^6), \tag{4.15}$$

with the topological susceptibility $\chi(T)$ and the fourth moment $\chi_4(T)$ defined as

$$\chi(T) = \frac{\langle Q^2 \rangle}{\mathcal{V}}, \qquad \chi_4(T) = \frac{1}{\mathcal{V}}\left[\langle Q^4 \rangle - 3\langle Q^2 \rangle^2\right], \tag{4.16}$$

where $\mathcal{V}$ denotes the space time volume. The temperature dependence of the observables is not explicitly written to facilitate readability such that $\chi := \chi(T)$. Let us note that in the literature the deviation from the susceptibility is often considered [197–199]

$$\Delta f(\theta) = \frac{1}{2}\chi\theta^2\left[1 + b_2\theta^2 + ...\right], \qquad b_2 = -\frac{\chi_4}{12\chi}. \tag{4.17}$$

The free energy (density) is a continuous function, hence we expect at the transition $f_c = f_d$, with the index c denoting the confined and d the deconfined phase. Expanding them in θ and reduced temperature t at leading order and dropping the constant terms leads to

$$f_c(t,\theta)/T_c = A_c t + \frac{\chi_c}{2}\theta^2, \tag{4.18}$$

$$f_d(t,\theta)/T_c = A_d t + \frac{\chi_d}{2}\theta^2. \tag{4.19}$$

The equality of f_c and f_d right at the transition can be rewritten as

$$T_c A_c t + \frac{\chi_c}{2}\theta^2 = T_c A_d t + \frac{\chi_d}{2}\theta^2, \tag{4.20}$$

and simplified to

$$\frac{T_c(\theta)}{T_c(0)} = 1 + \frac{\Delta\chi}{2\Delta\epsilon}\theta^2 := 1 + R_\theta\theta^2. \tag{4.21}$$

Here we used $\Delta\chi = \chi_d - \chi_c$ and the latent heat $\Delta\epsilon$ at $\theta = 0$

$$\begin{aligned}\Delta\epsilon = \epsilon_d - \epsilon_c &= T^2\left(-\partial_T(f_d/T) + \partial_T(f_c/T)\right)_{T=T_c} \\ &\simeq T_c(A_c - A_d).\end{aligned} \tag{4.22}$$

Using our result for the latent heat $\Delta\epsilon/T_c^4 = 1.025(21)(27)$ as calculated in Section 4.1.5, we find, with $R_\theta = 0.0178(5)$ from [196] (which is continuum extrapolated on $LT = 4$), $\Delta\chi/T_c^4 = -0.0365(18)$. Our goal is to quantify $\Delta\chi$ and the curvature R_θ as a direct lattice result in the continuum and infinite volume limit. Therefore we use the methods such as identifying hot and cold phases via histograms and parallel tempering as used to investigate the deconfinement transition in the last Sections. The following Sections are part of our publications [168, 200].

4.2.1 The topological charge on the lattice

We simulated the pure SU(3) Yang-Mills theory with the Symanzik-improved gauge action in a narrow range of gauge couplings around β_c using parallel tempering. The center of this range was fine tuned to the critical coupling β_c with a per mille precision in T/T_c. At this coupling we stored the configurations for further analysis. The use of parallel tempering has significantly reduced the auto-correlation time by allowing a frequent exchange of configurations between $T < T_c$, $T \approx T_c$ and $T > T_c$ sub-ensembles. On each lattice configuration we measured the Symanzik-improved topological charge defined similarly as in [201–203]

$$Q = \sum_{mn\in\{11,12\}} c_{nm} Q_{mn}, \tag{4.23}$$

where the coefficients c_{mn} are

$$c_{11} = 10/3, \quad c_{12} = -1/3, \tag{4.24}$$

and Q_{mn} is the naive topological charge defined through the lattice version of the field strength tensor ($\hat{F}_{\mu\nu}$)

$$Q_{mn} = \frac{1}{32\pi^2}\frac{1}{m^2n^2}\sum_x \sum_{\mu,\nu,\rho,\sigma} \epsilon_{\mu\nu\rho\sigma} \cdot \mathrm{tr}(\hat{F}_{\mu\nu}(x;m,n)\hat{F}_{\rho\sigma}(x;m,n)). \tag{4.25}$$

$\hat{F}_{\mu\nu}(x;m,n)$ is built by averaging clover terms of $m \times n$ plaquettes at site x on the $\mu\nu$ plane. We introduced smearing on the gauge field via the Wilson flow, which allowed us to measure a renormalized topological charge which we defined at a given flow time t. All moments of Q are a constant function of the flow time t in the continuum. In practice one selects a fixed flow time t in physical units, e.g. relative to the actual temperature T at which the continuum extrapolation can be carried out using the lattices at hand. The choice of t is, thus, a compromise, such that t should be small enough to avoid high computational costs but also to avoid finite volume effects $t \ll L^2$, yet large enough to maintain $t \gg a^2$. To choose an appropriate flow time, we study the t dependence of χ as presented on the left panel of Fig. 4.14. We show the normalized susceptibility χ/T_c^4, so that the comparison of lattices with different resolution is meaningful. Different curves with the same color represent

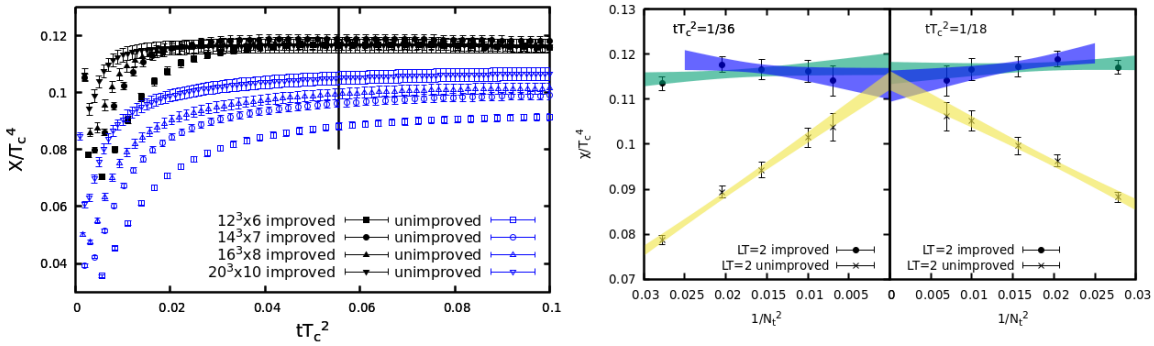

Figure 4.14: Left: χ/T_c^4 as function of tT_c^2 on $LT = 2$ with different resolutions. Black points indicate results from a Symanzik-improved topological charge and blue empty points are obtained using no improvement. Right: Continuum extrapolations of χ/T_c^4 on $LT = 2$ lattices for different flow times written as $tT_c^2 = 1/36$ (left) and $tT_c^2 = 1/18$ (right). The colored bands show linear fits on the data. The shorter bands of color blue are linear fits on the improved data using data only from finer lattices $N_\tau > 6$. In the case of t/T_c^2=1/36 the reduced chi square $\chi_r^2 = \chi^2/(\text{degrees of freedom})$ of the fits for the unimproved, improved and the short range improved data are respectively $\chi^2_{\texttt{unimp}} = 1.06/3$, $\chi^2_{\texttt{imp}} = 3.25/3$ and $\chi^2_{\texttt{imp,s}} = 0.14/2$. In the case of tT_c^2=1/18 we got $\chi^2_{\texttt{unimp}} = 0.85/3$, $\chi^2_{\texttt{imp}} = 1.57/3$ and $\chi^2_{\texttt{imp,s}} = 0.17/2$.

different lattice spacings, and with different colors we show data that were calculated from the improved or unimproved topological charge. We defined Q at a flow time that fell into the plateau region even in the case of the coarsest lattices. Our choice of the flow time $tT^2 = 1/18$ is highlighted with a black vertical line. Fixing t we could calculate χ and determine a continuum limit for Symanzik-improved and unimproved data sets, which we compare on the right panel of Fig. 4.14 together with results that we calculated at a smaller flow time $tT^2 = 1/36$. If Q is renormalized correctly, the continuum limits obtained from improved and unimproved data should agree. This is true in the case with our choice of t (right hand side), whereas at a smaller t (left hand side) finite size effects are still significant and improved and unimproved continuum extrapolations slightly differ. The blue bands show a shorter range fit on the improved data, excluding the $N_\tau = 6$ lattice. The continuum limit from the smaller fit range extrapolation is compatible with results using the whole data set, therefore we will use one or the other of the two cases in the following sections depending on the χ^2 of the fit on the actual data. In the next section we describe a broader temperature scan throughout the transition 0.9 T/T_c-1.1 T/T_c. Calculating the Wilson flow at several temperatures would have a large computational cost. Therefore in this case we calculated Q after using stout smearing on the gauge field corresponding to the same physical smearing radius as in the case of the Wilson flow. We performed a number of stout smearings ($\rho = 0.125$), such that $tT_c^2 = 1/18 = N_{\text{smear}}\ \rho/N_\tau^2$. This means $N_{\text{smear}} = 16$ for the coarsest lattice ($N_\tau = 6$) and $21.\bar{7}$ steps for $N_\tau = 7$, $28.\bar{4}$ for $N_\tau = 8$, and $44.\bar{4}$ steps for $N_\tau = 10$. Non integers steps were realized through an interpolation of Q in the step number. The difference between the two methods turned out to be statistically insignificant. Hence we choose the cheaper smearing procedure.

4.2.2 The continuum extrapolated susceptibility in the transition region

In addition to the simulations we carried out by tuning precisely at the transition temperature, we measured Q for ensembles generated in the vicinity of the transition temperature. Employing parallel tempering we were able to cover the temperature range $0.9T_c < T < 1.1T_c$ in a fine mesh of 64 or more gauge couplings. In this Section we focus on the aspect ratio $LT = 4$, for which we could carry out the continuum extrapolation. In Fig. 4.15 the normalized topological susceptibility in the vicinity of T_c is presented for $N_\tau = 6, 7, 8, 10$. For

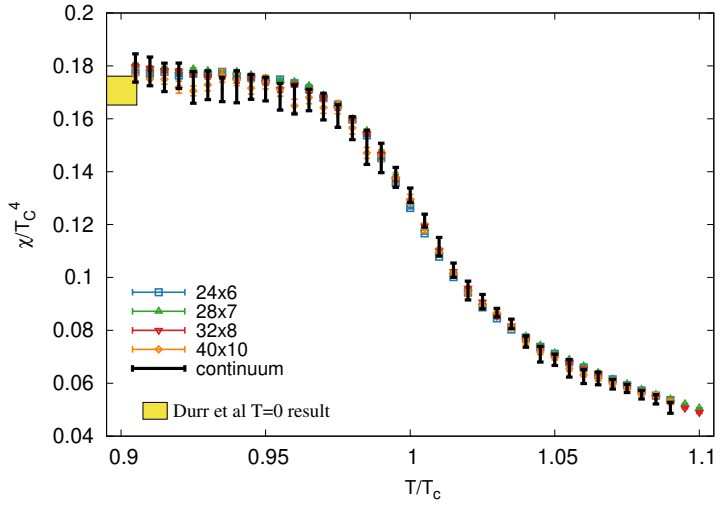

Figure 4.15: χ/T_c^4 as function of the temperature around T_c for aspect ratio $LT = 4$. The continuum extrapolation, which includes statistical and systematic uncertainties, is shown in black. A result at $T = 0$ from [204] is added in yellow. It was given in r_0 units, which can be translated by combining $w_0 T_c = 0.25384(23)$ from [40] with $w_0/r_0 = 0.341(2)$ from [205] to obtain $\chi/T_c^4 = 0.1707(55)$.

the continuum extrapolation, we used a spline interpolation in β to extract data at equal temperatures for all N_τ. The continuum limit is then performed at fixed temperatures independently, whereby we use two different scale setting functions. The first scale setting is defined through w_0: we used the $w_0/a(\beta)$ data set from 48^4 lattice simulations in the same β range. These w_0/a data were translated to $T_c a(\beta)$ scale by the factor $w_0 T_c = 0.25265$ valid for the aspect ratio $LT = 4$ (and neglecting its per-mill level error). The second scale setting was defined through the sequence of the transition gauge couplings $(\beta_c(N_\tau))$ for various N_τ as determined in [40]. We, thus, set $T_c a(\beta_c(N_\tau)) = 1/N_\tau$ and interpolate to the other gauge couplings (using a polynomial fit). We can estimate the systematic error of the continuum extrapolation by first fitting with the $N_\tau = 6$ and omitting it in a second fit.

4.2.3 The discontinuity of the topological susceptibility

In this Section we want to quantify $\Delta\chi(T_c)$ in the continuum and infinite volume limit. As presented in Fig. 4.16 we can see no significant volume dependence in the deconfined phase, but below T_c the slope rapidly grows with the volume. Multiplying the temperature axis with the volume as indicated on the inset plot, there is an overlap of the χ/T_c^4 curves, typical for a 1^{st} order phase transition. In Fig. 4.17 we show the same lattice configurations by splitting the ensembles into confined $(|P| < P_c)$ and deconfined $(|P| > P_c)$ sub-ensembles.

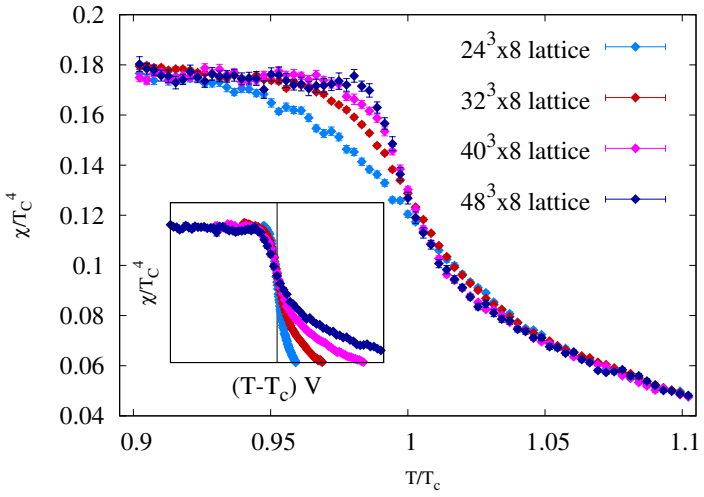

Figure 4.16: χ/T_c^4 as function of the temperature around T_c for aspect ratios $LT = 3, 4, 5, 6$ on $N_\tau = 8$. The increasing slope indicates a discontinuity. The inset plot normalizes the temperature axis with the volume: there the curves overlap at and below T_c.

Similar as described in Section 4.1.5 and shown on the right panel of Fig. 4.11, P_c is the

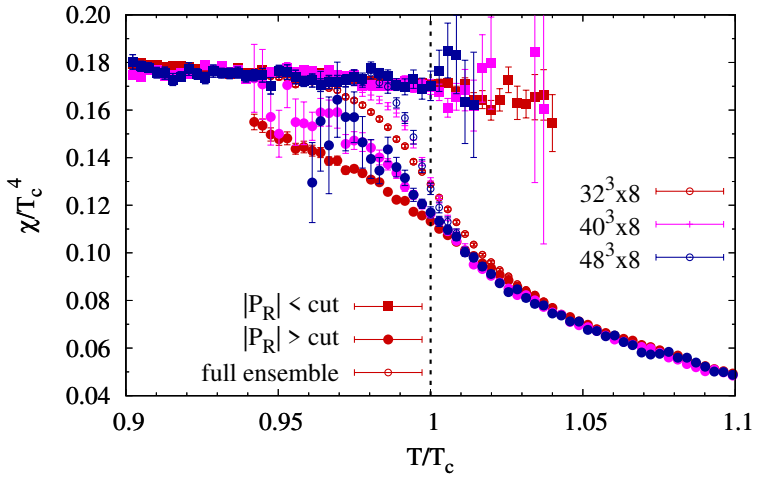

Figure 4.17: χ/T_c^4 as function of the temperature around T_c for aspect ratios $LT = 4, 5, 6$ on $N_\tau = 8$. The high and low temperature phases were separated into two sub-ensembles via cutting the Polyakov loop histogram at the local minimum between both peaks.

position of the local minimum of the renormalized Polyakov loop histogram at T_c for all temperatures. We see that, at T_c, χ takes very distinct values in the two phases, and this extends to a small vicinity of the transition temperature, depending on the volume. Similar to the renormalization scheme described in Section 4.1.1, we renormalize the absolute value of the Polyakov loop according to

$$P(T; N_x, N_\tau) = P_0(\beta(TN_\tau); N_x, N_\tau) Z(\beta(TN_\tau))^{N_\tau}, \tag{4.26}$$

with $P_0(\beta(TN_\tau); N_x, N_\tau)$ denoting the ensemble average of the volume averaged bare Polyakov loop. The renormalization factor $Z(\beta)$ is determined by setting a renormalization condition $P(T) \equiv 1$ at $T = T_c$. We determined Z using $LT = 4$ lattices with $N_\tau = 5, 6, 7, 8, 10$ and 12. A polynomial fit to $\log Z(\beta)$ allows an interpolation in β. In the following systematic analysis the error coming from the Polyakov loop renormalization refers to the ambiguity in the $Z(\beta)$ interpolation scheme. We performed simulations right at β_c and took possible deviations into account by reweighting to $b_3 = 0$ (recall Section 4.1.1).

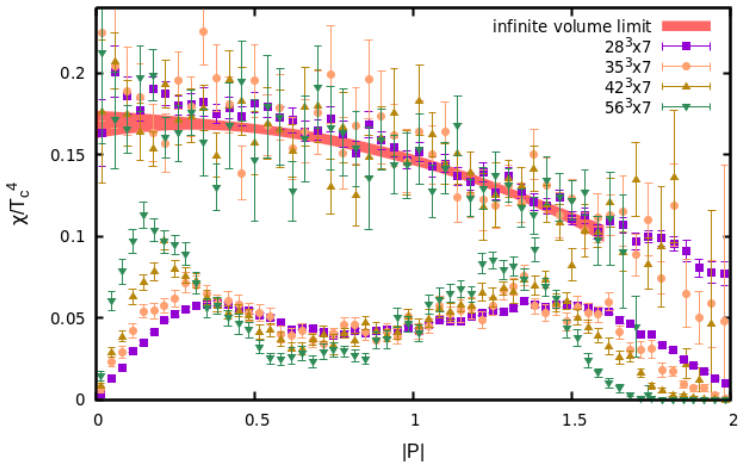

Figure 4.18: χ/T_c^4 as function of absolute value of the renormalized Polyakov loop. In the lower region we show Polyakov loop histograms belonging for different volumes. The temporal extension of the lattices used for this figure is $N_\tau = 7$.

In Fig. 4.18, for each Polyakov loop bin of the reweighted ensembles χ/T_c^4 is shown. We observe a smooth function for each volume, with a mild volume dependence. The infinite volume limit is calculated with a 2D fit of a second degree polynomial. We determined $\Delta\chi$ at the transition ensemble-by-ensemble by subtracting the value of χ in cold phase from that of the hot phase (similar to the latent heat calculation). Then we extrapolated the infinite volume and the continuum limit via a two dimensional fit. The systematic error analysis is performed in the following way: First we varied the fit range by including and excluding data with the smallest aspect ratio $LT = 4$, then we used two different fit formulas for the infinite volume and continuum extrapolations, one was a function with three parameters $f(x, y) = a+b\cdot x+c\cdot y$ and the other was a function with four parameters $g(x, y) = a+b\cdot x+c\cdot y+d\cdot xy$, with $x = 1/N_\tau^2$ and $y = 1/(LT)^3$. Furthermore we varied the fit range of the function that was

Table 4.3: Error budget of $\Delta\chi/T_c^4$.

$\Delta\chi/T_c^4$		
median	-0.034378	
statistical error	0.0044	13 %
full systematic error	0.0032	9.3 %
Fit range	0.0026	7.43 %
Fit formula	0.0026	7.54 %
Fit range of histogram	0.0000	0.05 %
Renormalizing	0.0000	0.11 %

used to determine the minima of Polyakov loop histograms, the smaller range being $0.15|P|$-$1.85|P|$ and the larger range was $0.1|P|$-$1.9|P|$. Finally we used two different schemes to interpolate the renormalization factors of the Polyakov loop. In Table 4.3 the error budget is shown. As expected, the systematics is dominated by the ambiguities in the infinite volume extrapolation. Our directly calculated result $\Delta\chi/T_c^4 = -0.0344(44)(32)$ agrees with the estimated discontinuity obtained from Eq. (4.21).

4.2.4 The θ-dependence of the transition temperature

Similar to the situation for QCD at finite density, simulations at real θ are infeasible due to the resulting complex action. The method to determine R_θ in [206] uses simulations at imaginary values of the θ parameter (θ^I denotes the imaginary part). Analogously to the study of the T-μ_B phase diagram, we can also extract R_θ from $\theta = 0$ ensembles. To achieve this we start from the sub-ensemble of the tempered $\theta = 0$ simulation corresponding to $\beta \approx \beta_c(0)$, that we already used to obtain $\Delta\chi$. In these sub-ensemble Q was determined using the gradient flow. We perform a simultaneous reweighting in θ and β in order to maintain $b_3 = 0$ (in practice, we used a very small value of $\theta = 0.02i$). This third order cumulant could be obtained with high precision thanks to parallel tempering. The zero-crossing of b_3 was found through reweighting in β from a single gauge coupling, since all streams in the tempered simulation are roughly equally represented at each β. This eliminated the need for fitting the curve $b_3(\beta)$. In addition to this, we performed simulations at imaginary θ. Instead of the Hybrid Monte-Carlo technique we use the pseudo-heatbath algorithm (with overrelaxation sweeps) to propose updates that undergo a Metropolis step to accept or reject the update according to the action $S_{\text{topo}} = Q\theta^I$. This Q is defined using a sequence of stout smearings and the improved clover definition, such that the renormalization step is no longer necessary. For modest θ^I parameters (e.g. $\theta^I < 2$) and volumes ($LT \leq 6$) we find reasonable acceptance (>10%). The range of accessible θ^I parameters diminishes with the inverse volume. This, however, does not prohibit the use of larger lattices, since the slope of $b_3(\beta)$ scales proportionally to the volume, increasing the achievable precision on $\beta_c(\theta^I)$ accordingly. Thus, in a larger volume we can extract R_θ with a smaller lever arm (a smaller value of θ^I). With Eq. (4.21), we can construct a proxy quantity $\mathcal{F}$ for the curvature R_θ which is defined for $\theta = 0$ as well as for imaginary θ

$$\frac{\frac{T_c(\theta)}{T_c(0)} - 1}{\theta^2} := \mathcal{F}\left(\theta^2, 1/N_\tau^2, 1/(LT)^3\right), \tag{4.27}$$

with $T_c(\theta)/T_c(0) = w_0(\beta_c, \theta)/w_0(\beta_c, 0)$. The value of $\mathcal{F}\left(\theta^2, 1/N_\tau^2, 1/(LT)^3\right)$ at vanishing arguments is R_θ in the thermodynamic and continuum limit. We perform a global fit to the data $\mathcal{F}(x, y, z) = R_\theta + Ax + By + Cz$, where A, B and C are the leading slopes for the residual θ^2, lattice spacing and volume dependence of $\mathcal{F}$, respectively. We take three sources of systematic errors into account. First, the scale setting ambiguity, here using different interpolations to the $w_0 a(\beta)$ function. Second, we varied the fit formula, by enabling or disabling the $C/(LT)^3$ term. Most importantly, the third option controlled the continuum limit range: whether we included or excluded the coarsest lattice $N_\tau = 6$ in the continuum extrapolation. The final result for R_θ is shown in Table 4.4.

Table 4.4: Error budget of R_θ.

R_θ		
median	0.0181	
statistical error	0.00045	2.5 %
full systematic error	0.00064	3.5 %
w0 interpolation	$5 \cdot 10^{-6}$	0.03 %
choice of the fit function $\mathcal{F}$	0.00003	0.14 %
continuum extrap. range	0.0006	3.5 %

This result is in remarkable agreement with the earlier continuum extrapolated (though not infinite volume extrapolated) value given by the Pisa group $R_\theta = 0.0178(5)$ [196].

4.3 The critical quark mass in the heavy mass region

In the last Sections we studied the thermal and topological features of the deconfinement transition in quenched QCD. Now we want to investigate the thermodynamics of QCD in the heavy mass region including dynamical quarks. I refer to Section 2.5.1 to avoid repetitions of the historical outline regarding the research of the critical mass, but let us recall some main aspects of criticality in this regime.
Starting from the quenched approximation, decreasing the quark masses weakens the phase transition until the corresponding latent heat vanishes at the critical mass. These endpoints of the 1st order phase transition should be in the same universality class as the 3d Ising model or Z(2) spin systems sharing the same critical exponents. Our goal is the determination of the critical endpoint m_c in the $N_f = 3$ flavor theory, i.e. we investigate the diagonal of the Columbia plot with staggered fermions and 4stout smearing. This is a challenging task since we face critical slowing down and much higher computational costs compared to quenched simulations due to the inclusion of dynamical fermions. We use again parallel tempering to improve on critical slowing down, which features high auto-correlations times, too. Although the mechanisms of critical and supercritical slowing down are similar, they are not completely identical. The key challenge for the latter was to sample both phases, which are present in a finite volume near T_c. The barrier between both states significantly increases with the volume, which is a serious problem in a volume scaling study (recall Section 4.1.2). However, a key feature of a 2nd order phase transition is a diverging correlation length in the infinite volume limit. This implies a slow response of the system near criticality - critical slowing down - leading to a high auto-correlation time as well.

4.3.1 Mass scaling of the observables

We focus on the Polyakov loop and its susceptibility to study the spontaneous and explicit breaking of the Z(3) center symmetry. The latter leads to a non-vanishing value of $\langle |P| \rangle$ in the confined phase. Nevertheless, the Polyakov loop is still a steeply rising function in the transition region and its inflection point could be associated with the transition temperature. Another way to define a critical coupling is the determination of the peak position of the susceptibility, a strategy we used in the previous Sections and from now on. For simplicity we work with the bare quantities.

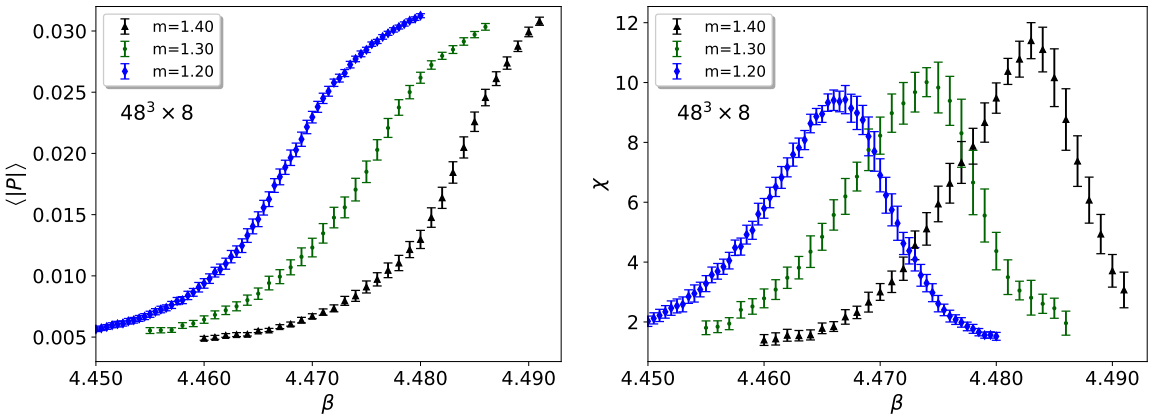

Figure 4.19: Polyakov loop (left) and its susceptibility (right) as a function of the coupling β at several masses (in lattice units) in the vicinity of the critical mass on a $48^3 \times 8$ lattice.

The Polyakov loop and its susceptibility are presented in Fig. 4.19 for several quark masses in lattice units. It is clearly visible that the the critical coupling is shifted to higher values by increasing the quark masses. A similar statement can be made for the peak of the susceptibility which increases with the quark masses. Analyzing the peak of the susceptibility is a suitable method to determine the type of phase transition. A diverging peak in the infinite volume limit is a clear sign of a real transition. The main task is then how to determine the peak as precisely as possible. A suitable strategy is to express the susceptibility as a function of the Polyakov loop, as shown in Fig. 4.20. The advantage is a simpler form of $\chi\left(\langle|P|\rangle\right)$ compared to $\chi(\beta)$ (right panel of Fig. 4.19), whereby the latter is compatible with a larger set of possible fitting functions. For this purpose, all jackknife blocks (cubic splines) are solved for the central sample: $\langle|P|\rangle(\beta) = \text{const.}$. The resulting β are substituted into the jackknife splines $\chi(\beta)$. In this way, the statistical error on $\langle|P|\rangle$ is converted into an additional error of χ. We used a similar strategy in [33] in which we expressed the chiral susceptibility as a function of the chiral condensate.

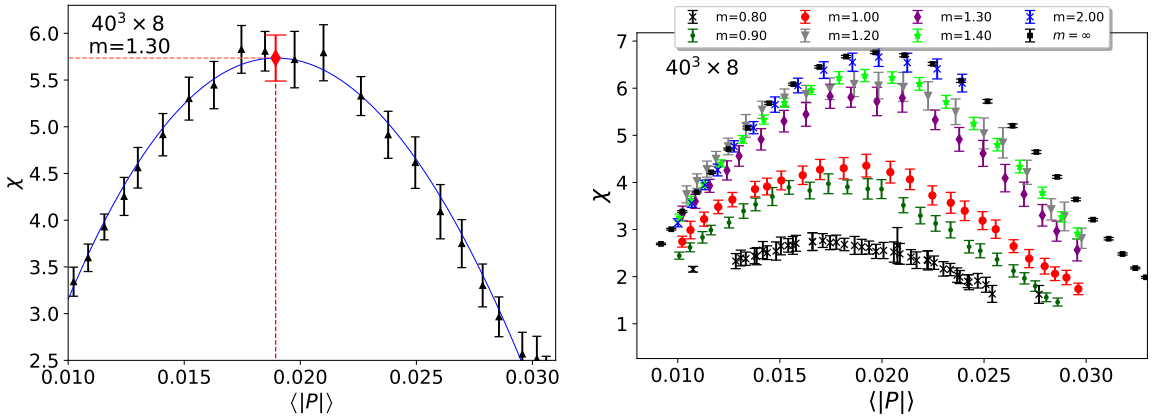

Figure 4.20: Susceptibility as a function of $\langle|P|\rangle$. Left: Illustration of the peak determination via a low order polynomial fit. Right: Impact of different quark masses on χ.

In the right panel of Fig. 4.20 the mass scaling of the susceptibility is presented for one lattice. The peak height increases with the quark mass, but this tendency gets weaker for the higher masses. In particular, a quark mass of $m = 2.00$ overlaps with the result from quenched simulations.

4.3.2 Volume scaling of χ_{max}

In the case of a 1$^{\text{st}}$ order phase transition, the peak height χ_{max} diverges linearly with the physical volume $(LT)^3 \to \infty$. For a 2$^{\text{nd}}$ order phase transition, this behavior is accompanied by critical exponents, probably given by Z(2) spin systems (recall Section 2.5.1). The last statement relies on continuum QCD, however we expect to observe signs of criticality also at finite spacing. In Fig. 4.21 the susceptibility as a function of β is presented for two different quark masses and the three largest lattices. In both cases, the peak height increases with the volume, but much milder for $m = 0.90$ compared to $m = 1.30$. The system seems to be located more deeply in the crossover phase for the lighter mass, while it gets more critical for the higher mass (later we will see that $m = 1.30$ is very close to the critical quark mass). In Fig. 4.22 the volume scaling of the inverse peak height as a function of the inverse physical volume is presented on $N_t = 8$ lattices for several quark masses. For $m = 0.90$, χ_{max}^{-1} takes on

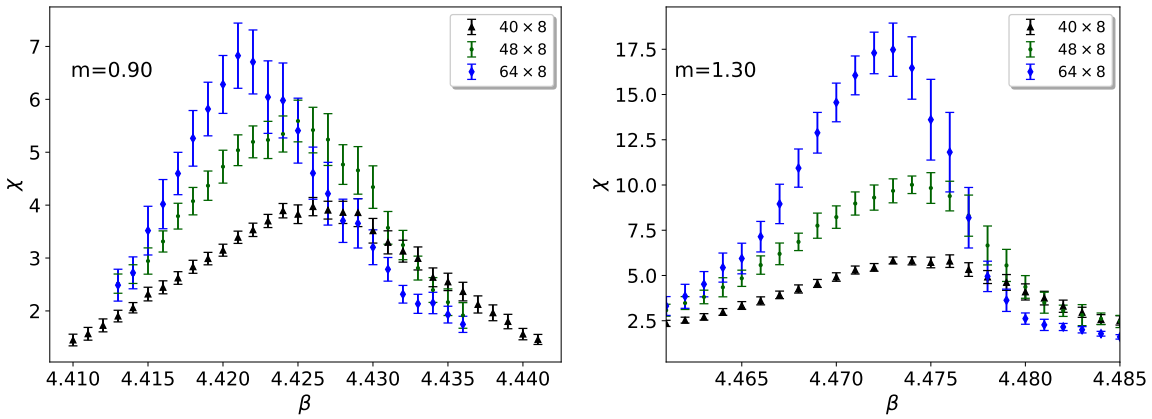

Figure 4.21: $\chi(\beta)$ on three different volumes. Left: Results for $m = 0.90$, rather located in the crossover phase. Right: Results for $m = 1.30$, close to the critical mass.

a finite and non-vanishing value in the infinite volume limit, which is a sign that the system is still in the crossover region. By increasing the quark masses, the systems seems to get

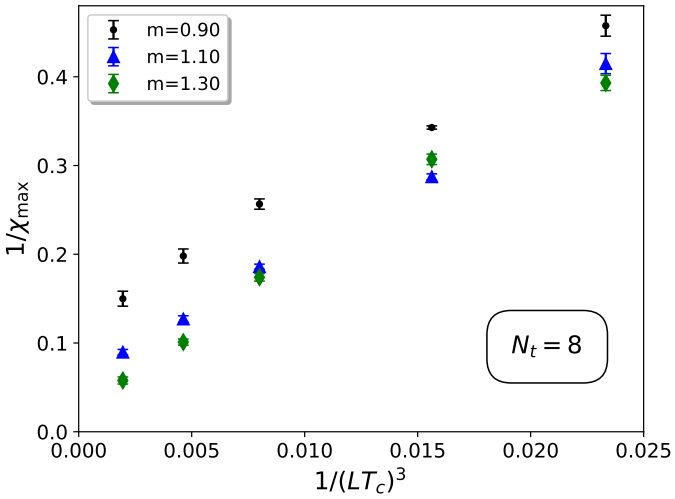

Figure 4.22: Inverse peak height as function of the inverse physical volume for three quark masses. The infinite volume limit corresponds to $1/(LT)^3 \to 0$.

more and more critical, since $\chi^{-1}_{\max}$ tends to vanish for $1/(LT)^3 \to 0$, but not linearly. In particular this is visible for the largest three lattices $(40^3 \times 8, 48^3 \times 8, 64^3 \times 8)$ for which the linear scaling sets in in quenched QCD (see right panel of Fig. 4.10).

4.3.3 Determination of the critical quark mass

In the case of a 2$^{\text{nd}}$ order phase transition, $\chi^{-1}_{\max}$ vanishes in the infinite volume limit according to a power law. We expect Z(2) critical exponents to apply, whereby the quark mass represents the symmetry breaking field. Therefore we extract the critical quark mass m_c via

$$\chi^{-1}_{\max}(LT_c \to \infty) = A \cdot (m_c - m)^{\gamma}, \tag{4.28}$$

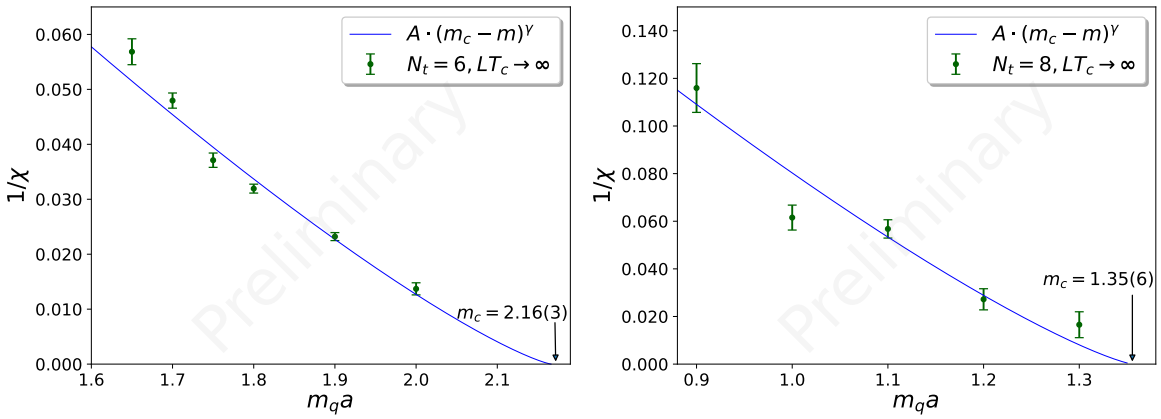

Figure 4.23: Inverse peak height in the infinite volume limit as a function of the quark masses for $N_t = 6$ (left) and $N_t = 8$ (right).

with A and m_c as fitting parameters and $\gamma = 1.2373$ [21]. In Fig. 4.23 the infinite volume extrapolated results for χ^{-1}_{max} as function of the quark mass are shown for $N_t = 6$ (left) and $N_t = 8$ (right). The critical quark masses are given in lattice units. We can construct dimensionless quantities such as the pseudoscalar mass or $w_0 T_c$ and get for $N_t = 8$: $m_{\text{ps}}/T_c = 20.20(4)$ and $w_0 T_c = 0.247(4)$ (errors are purely statistical). These results are close to previous results from matrix models [80] which predict $m_{\text{ps}}/T_c \approx 18.7$ and lattice simulations with Wilson fermions $m_{\text{ps}}/T_c \approx 18.1$ [84]. The latter was obtained for a $N_f = 2$ flavor theory, indicating that N_f could have a mild impact on the critical mass. This assumption is supported by [80] in which the authors declare that m_c increases with N_f.
There are several approaches on how to determine the critical quark mass. For instance, we focused on the peak of the susceptibility, [84] investigated the finite size scaling of the fourth Binder cumulant b_4 and [82] used a histogram method, for which the Polyakov loop histogram is reweighted, until the double peak structure vanishes. It is worth to note that the latter found a double peak structure in the crossover region for volumes $6 \leq LT \lesssim 9$, which is "washed out" for $LT = 10, 12$. This observation highlights the need for large volumes to classify the transition. So far continuum extrapolated results are still missing. This is a challenging and computational expensive task due to the need for large statistics, mainly caused by critical slowing down and the inclusion of dynamical quarks.

5 Lattice QCD EoS at finite density

In the last Sections we explored the mass and θ parameter space of thermal QCD with lattice simulations. Let us now turn to the physical point for which we set $\theta = 0$ and deal with physical quark masses. The corresponding phase diagram in the T-μ_B plane is currently intensively studied, both theoretically and experimentally (recall Section 2.6). In this chapter, we discuss recent results from lattice simulations, which are highly relevant for heavy ion collision experiments. The calculation of the EoS of strongly interacting matter under extreme conditions such as temperature, density or magnetic fields is of outstanding importance. It gives access to thermodynamic quantities such as entropy or energy density and thus to the understanding of interactions in heavy ion collisions or dense matter astrophysics. The EoS is an input for relativistic hydrodynamical simulations [207, 208] which are essential for the interpretation of experimental results. The capability to reliably detect gravitational waves opens the possibility to study super dense objects such as neutron stars (and their mergers) which could feature a "cold" QGP phase in their inner core. Signals of a possible 1^{st} order phase transition from the QGP to the hadronic phase should be visible in the thermodynamic quantities and hence shed light on the T-μ_B phase diagram at low temperatures.
First continuum extrapolated results from the lattice in (2+1) QCD were presented by the Wuppertal-Budapest collaboration [141] using 2stout staggered fermions on $N_t = 6, 8, 10$ and refined with $N_t = 10, 12, 16$ in [209]. HotQCD [210] could confirm these results with a different discretization using the HISQ action. Furthermore, the EoS with charm quarks (2+1+1) was calculated in [195] and in the background of magnetic fields in 2+1 QCD [211]. Direct calculations at finite density are hindered by the sign problem. Using a Taylor expansion of the EoS [212] with simulations at vanishing chemical potential, the results were extended to higher μ_B by adding more terms to the Taylor series [213]. We performed simulations at imaginary chemical potentials which enabled us to extrapolate the EoS to unreached high and real μ_B over a broad temperature range with a new expansion scheme. The work was later extended by matching conditions which are relevant for heavy ion collisions. The following Sections are part of our works [143, 214, 215].

5.1 The EoS from an alternative expansion scheme

The knowledge of the EoS from lattice simulations commonly consists of the Taylor expansion coefficients of the pressure around $\mu_B = 0$

$$\frac{p(T,\mu_B)}{T^4} = \sum_n \frac{1}{(2n)!}\chi^B_{2n}(T,0)\left(\frac{\mu_B}{T}\right)^{2n}, \tag{5.1}$$

where χ^B_j are the j-th derivatives of the normalized pressure:

$$\chi^B_j(T,\mu_B) = \left(\frac{\partial}{\partial \mu_B/T}\right)^j \frac{p(T,\mu_B)}{T^4}\ . \tag{5.2}$$

Besides diagonal coefficients, one can also define off-diagonal correlators between different conserved charges in QCD. Correlators between baryon number and strangeness, which we will need in our procedure, are defined as

$$\chi^{BS}_{jk}(T,\mu_B) = \left(\frac{\partial}{\partial \mu_B/T}\right)^j \left(\frac{\partial}{\partial \mu_S/T}\right)^k \frac{p(T,\mu_B)}{T^4} \ . \tag{5.3}$$

Such correlators have phenomenological relevance [216] and they can also be used to extrapolate the equation of state of QCD in the full, four-dimensional phase diagram at finite T, μ_B, μ_S, μ_Q [217]. High order derivatives of the pressure are notoriously difficult to calculate, as they suffer from a low signal-to-noise ratio. This is because their direct determination involves large cancellations of different terms containing derivatives of the Dirac operator [155]. Moreover, pathological behavior – namely non-monotonicity in the T- or μ_B-dependence – appears in the extrapolated thermodynamic quantities at chemical potentials beyond $\mu_B/T \lesssim 2-2.5$. This is due to the fact that, for large enough μ_B/T, the observables at finite chemical potential are dictated by the $\mu_B = 0$ temperature dependence of the last coefficient included in the expansion. Hence, the structures appearing around the QCD transition temperature in higher order coefficients are "translated" into the finite-μ_B behavior of e.g., the entropy, baryon density, etc. Another inherent problem with the Taylor expansion is the fact that it is carried out at constant temperature. This means that the values of the coefficients at $\mu_B = 0$ and a certain temperature T determine the equation of state at the same T at finite μ_B, while the pseudo-critical temperature T_{pc} might have varied considerably. While a sufficiently large number of expansion coefficients would lead to smooth extrapolated functions, even though the Taylor coefficients themselves present a complex structure around the transition temperature, the problem here is rather practical. A scheme that could work with fewer coefficients would be preferable from a cost point of view. In Fig. 5.1 we show

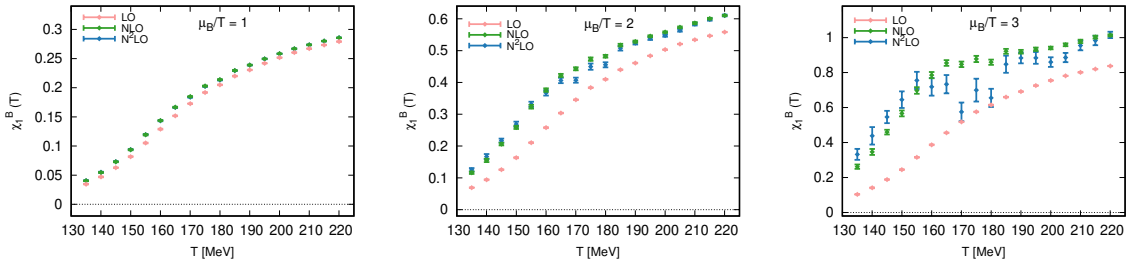

Figure 5.1: Baryon density from a Taylor expansion with the coefficients of [218], at $\mu_B/T = 1, 2, 3$, as a function of the temperature. Different colors correspond to the order to which the expansion is carried out.

the baryon density $n_B(T)$ obtained from a Taylor expansion with the coefficients in [218], at $\hat{\mu}_B = 1, 2, 3$. The extrapolation is shown including an increasing number of coefficients, to show the effect of higher-order ones. The leading-order (LO) and higher truncations refer to $\sim \hat{\mu}_B \partial n_B(T)/\partial \hat{\mu}_B$, or $\sim \frac{1}{6}\hat{\mu}_B^3 \partial^3 n_B(T)/\partial \hat{\mu}_B^3$, etc. being the last term in the expansion. The derivatives are taken at $\mu_B = 0$. At $\hat{\mu}_B = 1$ apparent convergence is achieved at the NLO level, for higher chemical potential this is not the case. Especially at $\hat{\mu}_B = 3$, the inclusion of all the coefficients in [218] causes unphysical non-monotonic behavior.
We start with an interesting obervation from imaginary μ_B simulations: In the left panel of Fig. 5.2 we show temperature scans of the quantity $n_B(T)/\hat{\mu}_B = \chi_1^B(T,\hat{\mu}_B)/\hat{\mu}_B$ for several fixed imaginary μ_B/T ratios. The 0/0 limit at $\mu_B = 0$ can be easily resolved and equals $\chi_2^B(T)$.

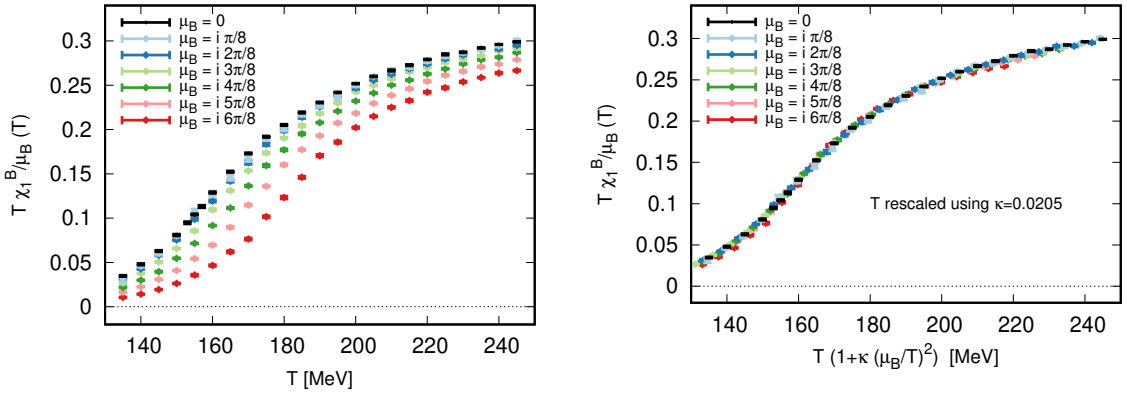

Figure 5.2: Left: The (imaginary) baryon density at simulated (imaginary) baryon chemical potentials, divided by the chemical potential. The points at $\mu_B = 0$ (black) show the second baryon susceptibility $\chi_2^B(T)$. Right: Same curves as in the left panel, with a temperature rescaled in accordance to Eq. (5.5) with $\kappa = 0.0205$.

The T-dependence of the normalized baryon density at finite chemical potential appears to be simply shifted/rescaled towards higher temperatures from the $\mu_B = 0$ results for χ_2^B. This behavior is more apparent in the vicinity of the transition, where the slope of these curves is larger. At very high temperatures, as well as at very low temperatures a simple shift cannot describe the physics, since the curves become extremely flat. A simple rescaling of temperatures can be described as

$$\frac{\chi_1^B(T, \hat{\mu}_B)}{\hat{\mu}_B} = \chi_2^B(T', 0), \tag{5.4}$$

where the actual temperature difference can be expressed through a μ_B-dependent rescaling factor that we write for simplicity as

$$T' = T\left(1 + \kappa \hat{\mu}_B^2\right). \tag{5.5}$$

In the right panel of Fig. 5.2 we show a version of the curves in the upper panel, where all the finite-$\hat{\mu}_B$ curves are shifted in accordance to Eq. (5.5) with $\kappa = 0.0205$. Remarkably, we note how well the curves are superimposed to each other, even with the simple assumption of a single, T-independent parameter governing the transformation. A similar behavior is observed for other quantities too. We show in Fig. 5.3 the first and second order fluctuations of strangeness at imaginary baryon chemical potentials. In analogy with Eq. (5.4) one has:

$$\frac{\chi_1^S(T, \hat{\mu}_B)}{\hat{\mu}_B} = \chi_{11}^{BS}(T', 0), \tag{5.6}$$

$$\chi_2^S(T, \hat{\mu}_B) = \chi_2^S(T', 0), \tag{5.7}$$

where T' is defined analogously to Eq. (5.5), albeit with different κ parameters.

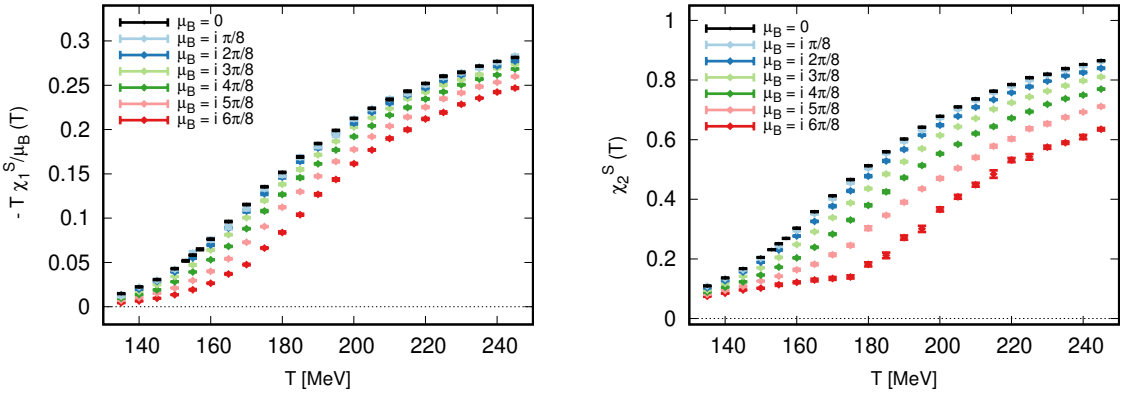

Figure 5.3: Left: (Imaginary) strangeness density divided by the baryon chemical potential. Right: Strangeness susceptibility at simulated (imaginary) baryon chemical potentials. The points at $\mu_B = 0$ (black) show the baryon- strangeness correlator $\chi_{11}^{BS}(T)$ (left) and the second strangeness susceptibility $\chi_2^S(T)$ (right), respectively.

Motivation

To motivate our alternative summation scheme, let us first consider a crude approximation that we will later refine. We take Eq. (5.5) at face value and use it together with Eq. (5.4) to obtain a well defined $\chi_1^B(T, \hat{\mu}_B)$ function. We need a $\chi_2^B(T, 0)$ function as well, which we borrow from a deliberately simple fit $f(T) = a + b \arctan(c(T - d))$ to our data on a $48^3 \times 12$ lattice. In principle, we could not only calculate $\chi_1^B(T, \hat{\mu}_B)$ at arbitrary $\hat{\mu}_B$ but, blindly believing Eq. (5.5), one could calculate the higher μ_B-derivatives as well. While this will not describe Nature precisely, it can serve as a test for the Taylor expansion method. To this end, we took several $\hat{\mu}_B$-derivatives of our $\chi_1^B(T, \hat{\mu}_B)$ function and calculated its truncated Taylor series for the lowest four orders. Here LO means just plotting $\chi_2^B(T, 0)$. We compared our mock curve (labelled as "full") against its Taylor expansion at three real values of the chemical potential (see Fig. 5.4). For $\hat{\mu}_B = 1, 2$, the summation up to LO and NLO is sufficient to

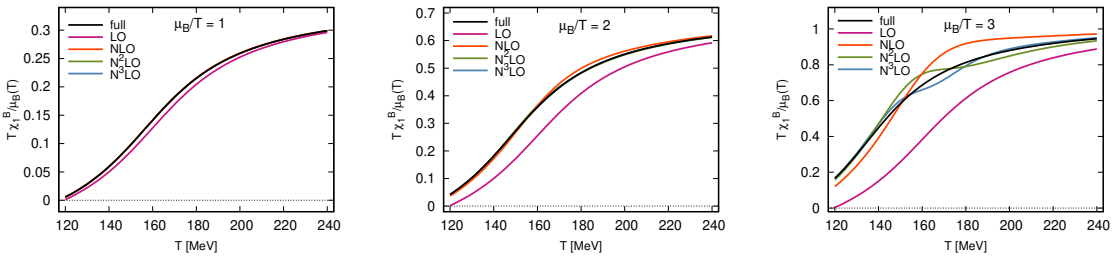

Figure 5.4: Benchmarking various orders of the Taylor method assuming an equation of state, where the μ_B-dependence of $\chi_1^B/\hat{\mu}_B$ consists of a simple shift in temperature. This equation of state is a somewhat simplified form of the observed behaviour.

perfectly reproduce the function. However, as the chemical potential is increased, the Taylor expansion carried as far as the NNNLO does not reproduce the original function. On the one hand, convergence is achieved more slowly; on the other hand, spurious effects appear, which generally manifest themselves in a non-monotonicity of the function. The picture emerging from this simple analysis is rather suggestive, especially when compared to the results shown in Fig. 5.1 (right panel) obtained from actual lattice data. We also note that this simple

analysis does not suffer from the additional complications of signal extraction for higher order expansion coefficients, which in turn play a relevant role in the real-data analysis.

5.1.1 Formalism

At vanishing chemical potential, we can express the normalized baryon density as a Taylor expansion:

$$\frac{\chi_1^B}{\hat{\mu}_B}(T,\hat{\mu}_B) = \chi_2^B(T,0) + \frac{\hat{\mu}_B^2}{6}\chi_4^B(T,0) + \frac{\hat{\mu}_B^4}{120}\chi_6^B(T,0) + \cdots . \tag{5.8}$$

As shown in Fig. 5.2, the behavior of $\frac{\chi_1^B}{\hat{\mu}_B}(T,\hat{\mu}_B)$ at finite chemical potential clearly resembles that of $\chi_2^B(T,\hat{\mu}_B)$, although shifted/rescaled in temperature. As long as $\chi_1^B/\hat{\mu}_B$ is a monotonic function of T, the finite density physics can be encoded into the $T'(T,\hat{\mu}_B)$ function. A straightforward, but systematic generalization of Eq. (5.5) reads:

$$T'(T,\hat{\mu}_B) = T\left(1 + \kappa_2^{BB}(T)\hat{\mu}_B^2 + \kappa_4^{BB}(T)\hat{\mu}_B^4 + \mathcal{O}(\hat{\mu}_B^6)\right) . \tag{5.9}$$

In the above equation, we introduced the new parameters $\kappa_2^{BB}(T)$ and $\kappa_4^{BB}(T)$, which describe the shift/rescaling of the temperature of $\chi_1^B/\hat{\mu}_B$ at finite μ_B. Analogous parameters will be introduced below for the case of $\chi_1^S/\hat{\mu}_B$ (κ_2^{BS} and κ_4^{BS}) and of χ_2^S (κ_2^{SS} and κ_4^{SS}) at finite μ_B. In a way, this formalism replaces the fixed temperature μ_B expansion by a fixed-observable temperature expansion. Having now the expressions Eqs. (5.4) and (5.8) for the same quantity we require their equality at each order in the $\hat{\mu}_B$ expansion at $\mu_B = 0$, having:

$$\chi_2^B(T',0) = \chi_2^B(T,0) + (T'-T)\chi_2^{B\prime}(T,0) + \frac{(T'-T)^2}{2}\chi_2^{B\prime\prime}(T,0) + \cdots , \tag{5.10}$$

with the temperature derivatives

$$\chi_2^{B\prime}(T,0) := \frac{\mathrm{d}}{\mathrm{d}T}\chi_2^B(T,0), \qquad \chi_2^{B\prime\prime}(T,0) := \frac{\mathrm{d}^2}{\mathrm{d}T^2}\chi_2^B(T,0). \tag{5.11}$$

To facilitate readability, we suppress for now the baryon B indices for the κ coefficients and the explicit temperature dependence of χ_2^B or χ_4^B to illustrate the calculation:

$$(T'-T)\chi_2' = T\left(\kappa_2\hat{\mu}_B^2 + \kappa_4\hat{\mu}_B^4\right)\chi_2', \tag{5.12}$$

$$(T'-T)^2\chi_2'' = T^2\left(\kappa_2^2\hat{\mu}_B^4 + \kappa_4^2\hat{\mu}_B^8 + 2\kappa_2\kappa_4\hat{\mu}_B^6\right)\chi_2''. \tag{5.13}$$

Compare order by order Eqs. (5.8) and (5.10)

1. $\mathcal{O}(\hat{\mu}_B^2)$:

$$\chi_2'\kappa_2 T\hat{\mu}_B^2 = \frac{\hat{\mu}_B^2}{6}\chi_4 \tag{5.14}$$

$$\Longrightarrow \kappa_2^{BB}(T) = \frac{1}{6T}\frac{\chi_4^B(T)}{\chi_2^{B\prime}(T)} \tag{5.15}$$

2. $\mathcal{O}(\hat{\mu}_B^4)$:

$$\chi_2'T\kappa_4\hat{\mu}_B^4 + \frac{\hat{\mu}_B^4}{2}T^2\kappa_2^2\chi_2'' = \frac{\hat{\mu}_B^4}{120}\chi_6 \tag{5.16}$$

$$\Longrightarrow \kappa_4^{BB} = \frac{1}{360\chi_2^{B\prime}(T)^3}\left(3\chi_2^{B\prime}(T)^2\chi_6^B(T) - 5\chi_2^{B\prime\prime}(T)\chi_4^B(T)^2\right) \tag{5.17}$$

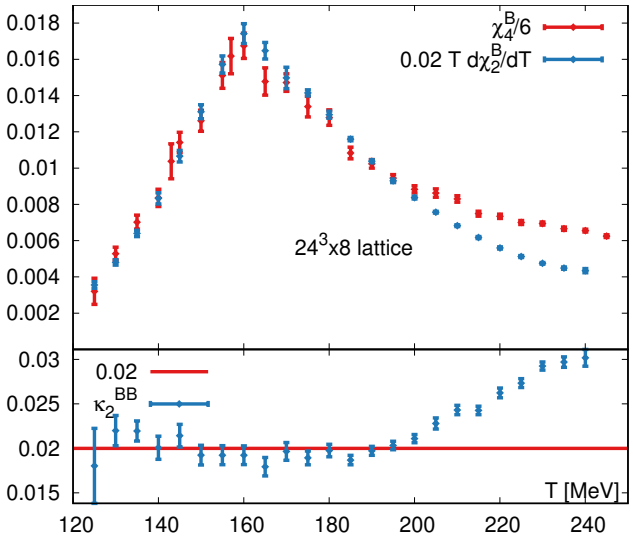

Figure 5.5: Evaluation of Eq. (5.15) on a $24^3 \times 8$ lattice with high statistics. The resulting $\kappa_2^{BB}(T)$ shows a very mild temperature dependence in the transition region.

Before we embark into the discussion of the lattice analysis, let us have an impression on the discussed quantities. Eqs. (5.15) and (5.17) give a way to directly determine $\kappa_2^{BB}(T)$ and $\kappa_4^{BB}(T)$ using only $\mu_B = 0$ data. This approach might be subject to numerical problems, especially in the case of $\kappa_4^{BB}(T)$, which is obtained as the difference of two competing terms. Notice, too, that Eq. (5.15) contains temperature-derivatives of the $\chi(T)$ coefficients, which may pose a numerical challenge, unless the coefficients are known with sufficient statistics and resolution in T. On lattices where high statistics data taking is feasible, we can investigate Eq. (5.15), at least for κ_2^{BB}. In the top panel of Fig. 5.5 we compare the numerator and (rescaled) denominator of Eq. (5.15), while their ratio $\kappa_2^{BB}(T)$ is shown in the bottom panel. In the entire transition region the ratio is consistent with a constant, because the peak in $\chi_4^B(T)$ is replicated in the temperature dependence of $\chi_2^B(T)$. As opposed to the Taylor coefficients, $\kappa_2^{BB}(T)$ shows a very mild temperature dependence.
A similar treatment can be applied to the other observables. For the second order fluctuations including baryon number and strangeness, one can consider

$$\frac{\chi_1^S}{\hat{\mu}_B}(T, \hat{\mu}_B) = \chi_{11}^{BS}(T,0) + \frac{\hat{\mu}_B^2}{6}\chi_{31}^{BS}(T,0) + \frac{\hat{\mu}_B^4}{120}\chi_{51}^{BS}(T,0) + \cdots , \tag{5.18}$$

and

$$\chi_2^S(T, \hat{\mu}_B) = \chi_2^S(T,0) + \frac{\hat{\mu}_B^2}{2}\chi_{22}^{BS}(T,0) + \frac{\hat{\mu}_B^4}{24}\chi_{42}^{BS}(T,0) + \cdots . \tag{5.19}$$

Similarly as before, one can show that

$$\kappa_2^{BS}(T) = \frac{1}{6T}\frac{\chi_{31}^{BS}(T)}{\chi_{11}^{BS\prime}(T)} , \tag{5.20}$$

$$\kappa_4^{BS}(T) = \frac{1}{360\chi_{11}^{BS\prime}(T)^3}\left(3\chi_{11}^{BS\prime}(T)^2\chi_{51}^{BS}(T) - 5\chi_{11}^{BS\prime\prime}(T)\chi_{31}^{BS}(T)^2\right) , \tag{5.21}$$

and

$$\kappa_2^{SS}(T) = \frac{1}{2T}\frac{\chi_{22}^{BS}(T)}{\chi_2^{S\prime}(T)}, \tag{5.22}$$

$$\kappa_4^{SS}(T) = \frac{1}{24{\chi_2^{S\prime}(T)}^3}\left({\chi_2^{S\prime}(T)}^2\chi_{42}^{BS}(T) - 3\chi_2^{S\prime\prime}(T){\chi_{22}^{BS}(T)}^2\right) . \tag{5.23}$$

To summarize: We use Eq. (5.9) (and its generalization with κ_2^{ij} and κ_4^{ij}) as the definition of a truncation scheme rather than to investigate a Taylor expanded result. We use lattice data at zero and imaginary μ_B to obtain the coefficients in Eq. (5.9), which then can be used to either calculate the Taylor coefficients or, even better, to extrapolate the equation of state at finite μ_B with no reference to the Taylor coefficients themselves. Also, we use imaginary chemical potentials not only to calculate the coefficients, but also to study the single observable first, on which the analysis is based. We base our description of the entire chemical potential-dependence of the QCD free energy function on $\chi_1^B(T, \hat{\mu}_B)/\hat{\mu}_B$. It is essential to rely on one observable only, in order to guarantee thermodynamic consistency: entropy, pressure and energy density will obey the known thermodynamic relations (see Section 5.1.5) only if they come from the same truncation scheme.

5.1.2 Simulation details

We use the lattice action and the parameters described in [155]. The action benefits from tree-level Symanzik improvement in the gauge sector and four levels of stout smearing for the staggered flavors. The up and down quarks are degenerate. The resulting light pair of quarks, as well as the strange and charm quarks assume their respective physical mass. We performed simulations at $\mu_B = 0$ on $32^3 \times 8$, $40^3 \times 10$, $48^3 \times 12$ and $64^3 \times 16$ lattices in a temperature range of $130-300$ MeV, and up to 500 MeV on larger volumes. These simulations were complemented at imaginary values of the chemical potential in the temperature range $135 - 245$ MeV for the lattice resolutions $N_\tau = 8, \ldots, 12$. The $\mu_B \neq 0$ data were simulated at $\mu_S = 0$, some of these ensembles were already used in [218]. In addition, we performed a high-statistics run on the cheap and coarse $24^3 \times 8$ lattice, mainly to produce Fig. 5.5. These data did not enter the continuum extrapolation.

5.1.3 The coefficients κ_2^{ij} and κ_4^{ij}

For the determination of κ_2^{ij} and κ_4^{ij}, one can take advantage of simulations both at zero and finite imaginary chemical potential. To extract $\kappa_4^{BB}(T)$ via Eq. (5.17), a precise result on $\chi_B^6(T)$ would be necessary. Instead, we utilize imaginary chemical potential simulations as follows: We perform simulations at imaginary values of the baryon chemical potential:

$$\hat{\mu}_B = i\frac{n\pi}{8} , \qquad n \in \{3, 4, 5, 6\}, \tag{5.24}$$

with $\hat{\mu}_Q = \hat{\mu}_S = 0$. We simulate temperatures in the range $T = 135 - 245\,\text{MeV}$. For each temperature T and chemical potential $\hat{\mu}_B$ we determine the temperature T' for which Eq. (5.4) (or Eqs. (5.6) and (5.7) for the other observables) holds, hence defining a function $T'(T, \hat{\mu}_B)$. We can rewrite Eq. (5.9) and define a proxy quantity according to

$$\Pi(T, \hat{\mu}_B) = \frac{T'(T, \hat{\mu}_B) - T}{T\hat{\mu}_B^2} \tag{5.25a}$$

$$= \kappa_2^{BB}(T') + \kappa_4^{BB}(T')\hat{\mu}_B^2 + \kappa_6^{BB}(T')\hat{\mu}_B^4 + \ldots \tag{5.25b}$$

and generalized it in a similar way for the other observables

$$\Pi(T, \hat{\mu}_B) = \kappa_2^{ij}(T') + \kappa_4^{ij}(T')\hat{\mu}_B^2 + \kappa_6^{ij}(T')\hat{\mu}_B^4 + \dots, \tag{5.26}$$

which we calculate via lattice simulations. The relatively precisely known function $\chi_2^B(T, 0)$ is first interpolated in temperature. Afterwards, we only need to measure $\chi_1^B(T, \mu_B)/\hat{\mu}_B$ on an ensemble with imaginary μ_B. Equating this to $\chi_2^B(T', 0)$ gives us $T'(T, \mu_B)$. In Section 5.2.5 this procedure is illustrated and generalized for other observables.

Having determined $\Pi(T, \hat{\mu}_B)$ for several imaginary chemical potentials and several lattice spacings for each given temperature, one can perform a polynomial fit in $\hat{\mu}_B^2$ and obtain the expansion coefficients. This can be done separately for each lattice. However, we prefer to combine the $\hat{\mu}_B$ and continuum fits in one two-dimensional fitting procedure. This combined fit is repeated for every temperature, in steps of 5 MeV. In order to estimate the systematic uncertainties associated to our results, we perform a number of analyses at each temperature. There are several ambiguous points that need to be considered. Most obviously, one could choose to include the $\kappa_6^{ij}(T)$ term in the fit or not, or consider the fit of $1/\Pi$ instead. Also the range in imaginary μ_B is arbitrary: we consider Im $\mu_B \leq 2.0$ or Im $\mu_B \leq 2.4$. When different lattice spacings are fitted together in a continuum extrapolation, one selects the bare parameters such that the ensembles correspond to the same physical temperature. This choice is, however, ambiguous too, as the scale setting may be based on various observables. In our case, we consider f_π or w_0 to this purpose. As we mentioned before, $\chi_2^B(T, 0)$ is subject to an interpolation, performed through basis splines. The same is true for $\chi_1^B(T, \hat{\mu}_B)$ at finite chemical potentials. Since the location of the node points is also arbitrary, we include three versions at $\mu_B = 0$ and two at imaginary μ_B. Finally, in the continuum extrapolation the coarsest lattice, $32^3 \times 8$, has either been used or dropped. The listed options can be considered in arbitrary combinations. In total we carry out all 144 fits to perform a continuum extrapolation of $\kappa_2^{ij}(T)$ and $\kappa_4^{ij}(T)$. After dropping the fits with a Q-value below a percent, we use uniform weights to produce histogram out of these (somewhat less than) 144 results for each temperature (see [33, 126] for the usage of Q-values in the Kolmogorov-Smirnov tests). In the plots we show combined errors, where we assume that statistical and systematic errors add up in quadrature. In the top panel of the left side of Fig. 5.6 we show the results of the temperature-by-temperature fit procedure for the parameters $\kappa_2^{BB}(T)$ and $\kappa_4^{BB}(T)$, alongside the corresponding expectations from the HRG model. We find that, within errors, $\kappa_2^{BB}(T)$ has hardly any dependence on the temperature, while $\kappa_4^{BB}(T)$ is everywhere consistent with zero at our current level of precision. Nonetheless, a clear separation of almost one order of magnitude appears between these two coefficients. We also note that good agreement with the HRG results is found up to at least $T = 160\,\text{MeV}$. In the central and bottom panels of the left side of Fig. 5.6 we show our results for the parameters κ_2^{BS}, κ_4^{BS} and κ_2^{SS}, κ_4^{SS} respectively, together with their HRG determinations. While for χ_{11}^{BS} barely any temperature dependence is observed, as in the case of χ_2^B, for χ_2^S a much stronger T-dependence is clearly visible. As in the case of κ_4^{BB}, κ_4^{BS} is consistent with zero throughout the whole temperature range we consider. On the other hand, κ_4^{SS} rises above zero for temperatures $T \gtrsim 220\,\text{MeV}$.

Correlated temperature fits to κ_2^{ij} and κ_4^{ij}

Recall that the error bars in Fig. 5.6 are highly correlated. The correlation is mostly systematic. The apparent 'waves' are often statistically not as significant as it seems at a first glance. For comparison we refer to the direct result on our coarsest lattice in Fig. 5.5, where these 'waves' are absent. Before moving on to calculate thermodynamic observables at finite

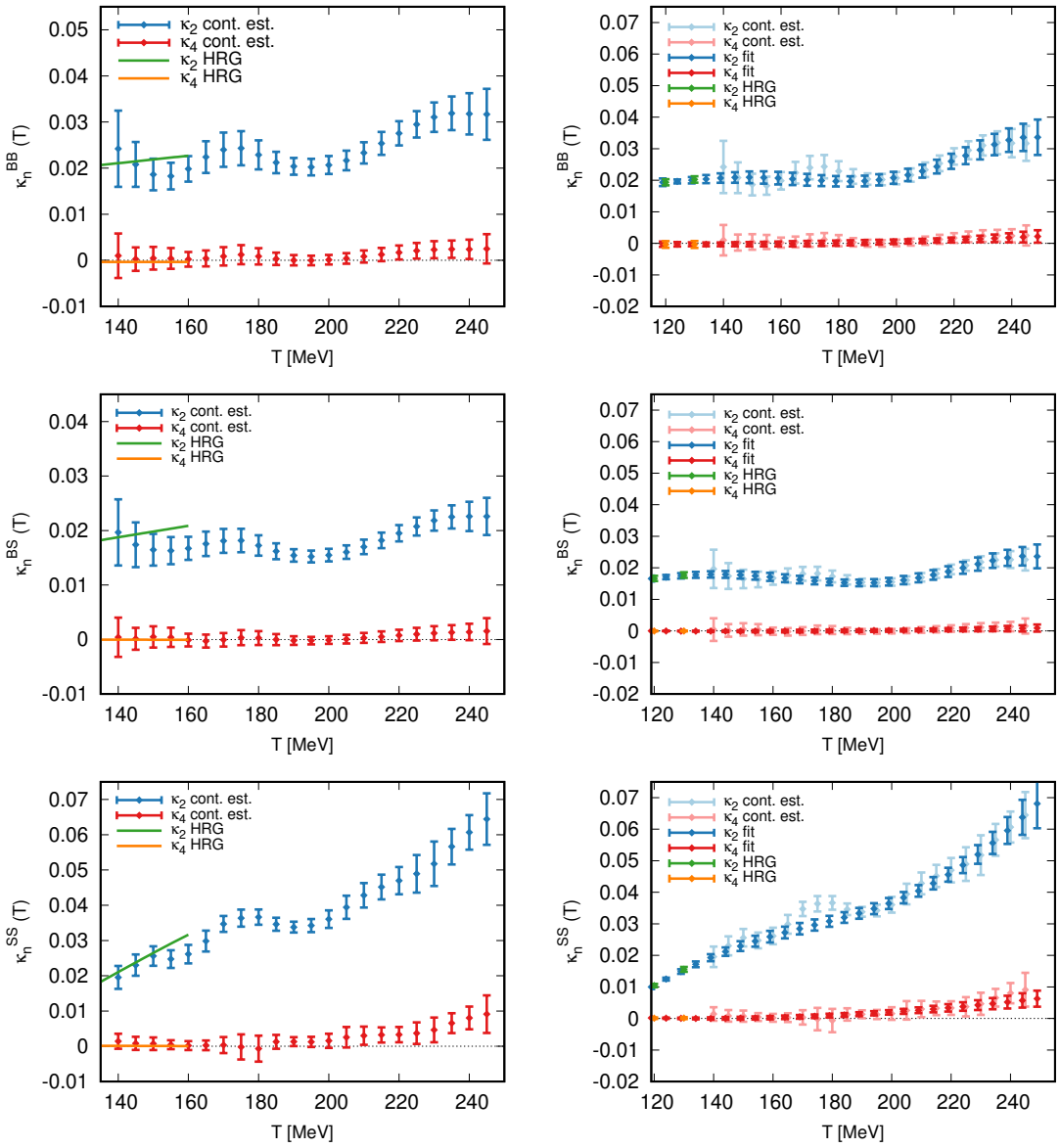

Figure 5.6: Left side: Continuum extrapolated result for the parameters $\kappa_2^{BB}(T)$ and $\kappa_4^{BB}(T)$ (top panel), $\kappa_2^{BS}(T)$ and $\kappa_4^{BS}(T)$ (central panel), and $\kappa_2^{SS}(T)$ and $\kappa_4^{SS}(T)$ (bottom panel). The parameters κ_2^{ij} are shown in blue, and the κ_4^{ij} in red. HRG results for all quantities are shown up to $T = 160\,\mathrm{MeV}$ (in green for κ_2^{ij} and orange for κ_4^{ij}, respectively). Right side: Results of the polynomial fits to the parameters κ_2^{ij} are shown in blue, and the κ_4^{ij} in red. The fitted quantities from the plots of the left side are shown by lighter blue and red points. Due to the lack of points at low T, we continued the data set with HRG points, show as green and orange dots. Though the polynomials do not always follow all "excursions" of the T-by-T result, the reduced χ^2 of the correlated temperature fit is always < 1. This is possible, because the fitted data are highly correlated, coming from both statistical and systematic effects.

real chemical potential, we construct a smoother version of our final results for κ_2^{ij} and κ_4^{ij}, in order to limit the influence of numerical effects on the final observables, but also to obtain the temperature derivatives needed to calculate the entropy density. Thanks to the very mild dependence of the coefficients on the temperature, we perform a polynomial fit of order 5 for the κ_2^{ij}, and of order 2 for the even less T-dependent κ_4^{ij}. Using fourth or sixth order for κ_2^{ij} hardly changes the result. In order to stabilize the low-temperature behavior, we include in the fit two points from the HRG model for $T = 120, 130\,\mathrm{MeV}$, to which we associate an uncertainty of 5% for κ_2^{ij} and of 300% for κ_4^{ij}. The choice of these particular values for the uncertainties is uniquely guided by the necessity of placing a constraint on the low-T behavior, while avoiding to drive the fit too strongly. For this reason, these arbitrary errors are chosen to be smaller, but comparable to the lattice ones. We note that the fits we perform take fully into account the correlations between results at different temperatures, systematic as well as statistical. Thus we encode all errors into the (correlated) errors of the coefficients of a polynomial. On the right side of Fig. 5.6 we show the results of the fits in darker color, with the fitted data in lighter shades. The HRG points included in the fit are shown as well.

5.1.4 Continuum result of $\chi_2^B(T)$ and its temperature derivative

In order to determine the value of thermodynamic quantities at finite real chemical potential, a continuum result for $\chi_2^B(T,0)$ is required in addition to $\kappa_2^{BB}(T)$ and $\kappa_4^{BB}(T)$. For some observables like the entropy, the temperature derivative of $\chi_2^B(T)$ has to be calculated as well. We have divided the temperature range into two parts: the transition region and the higher,

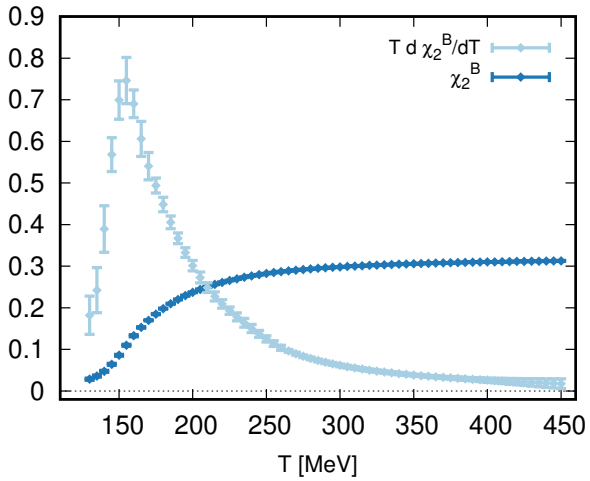

Figure 5.7: Continuum extrapolated $\chi_2^B(T)$ and $Td\chi_2^B(T)/dT$ functions from $N_\tau = 10$, 12 and 16 lattices at $\mu_B = 0$.

near-perturbative temperatures. For the lower temperature part, we interpolate using basis splines the $T \in [130\ \mathrm{MeV}, 300\ \mathrm{MeV}]$ data points. For the quantity $Td\chi_2^B(T)/dT$ we extended the data range with the HRG curve, so that the numerical derivative has a level arm at the lowest temperatures. The basis splines are cubic splines in the given temperature range. We fit the splines in temperature and in $1/N_\tau^2$ in one step. The fitted function in this range is thus:

$$\chi_2^B(T,0;N_\tau) = \sum_{i=1}^{n} \alpha_i b_i(T) + \frac{1}{N_\tau^2} \sum_{i=1}^{n} \beta_i b_i(T)\,, \tag{5.27}$$

where $b_i(t_j) = \delta_{ij}$ and t_j are the knots for the spline with $j = 1 \dots n$. Only the lattices with $N_\tau = 10, 12$ and 16 enter the continuum extrapolation. In the high temperature regime, the smooth monotonic behavior is not well described with cubic splines. Instead we performed a high order polynomial fit in the inverse temperature $1/T$. The known analytical form of the convergence to the Stefan-Boltzmann limit is, of course, not this polynomial. We do not wish to enforce the perturbative behavior at the intermediate temperatures that we describe. Thus, the constant in the $1/T$ description is not exactly the Stefan-Boltzmann limit, and for this reason, we cannot regard this as a basis for an extrapolation. However, this simple approach allows the interpolation and the calculation of the derivative. We used lattice data in the range $T = 180 - 450$ MeV. High- and low-temperature regions overlap and the two fitting methods give consistent results between $T = 200 - 280\,\mathrm{MeV}$ for both quantities. Thus, we simply concatenate the resulting functions at $T = 260\,\mathrm{MeV}$. We show the final version of the $Td\chi_2^B(T,0)/dT$ and $\chi_2^B(T,0)$ functions in Fig. 5.7.

5.1.5 Thermodynamics at real chemical potential

Once $\chi_1^B = n_B$ is determined, we have everything we need to extract the other thermodynamic quantities. The integration constant for the pressure is obviously the pressure itself at $\mu_B = 0$. We note here that, on the lattice, we always deal with dimensionless thermodynamic quantities, which correspond to the physical ones divided by suitable powers of the temperature. For example the dimensionful baryon density is $\chi_1^B = n_B = T^3 \hat{n}_B$ (we will hereafter use the hat to indicate dimensionless quantities). From the baryon density $\hat{n}_B(\hat{\mu}_B, T)$, the pressure is obtained through simple integration:

$$\frac{p(\mu_B, T)}{T^4} = \frac{\log Z}{T^3 V} = \hat{p}(\hat{\mu}_B, T) = \hat{p}(0, T) + \int_0^{\hat{\mu}_B} \mathrm{d}\hat{\mu}'_B \, \hat{n}_B(\hat{\mu}'_B, T). \tag{5.28}$$

The pressure at zero chemical potential is taken from [209]. Now let us derive the expression for the dimensionless entropy density $\hat{s}$ with the thermodynamic relations, which we used for the calculation of the latent heat in Section 4.1.5:

$$\begin{aligned}
\hat{s}(\hat{\mu}_B, T) &= \frac{1}{VT^3} s && \text{(5.29a)}\\
&= -\frac{1}{VT^3} \frac{\partial F}{\partial T} && \text{(5.29b)}\\
&= \frac{1}{VT^3} \left.\frac{\partial}{\partial T} (T \log Z)\right|_{\mu_B} && \text{(5.29c)}\\
&= \frac{1}{VT^3} \left.\frac{\partial}{\partial T} \left(VT^4 \hat{p}\right)\right|_{\mu_B} && \text{(5.29d)}\\
&= T \left.\frac{\partial \hat{p}}{\partial T}\right|_{\mu_B} + 4\hat{p} && \text{(5.29e)}\\
&= 4\hat{p} + T \left.\frac{\partial \hat{p}}{\partial T}\right|_{\hat{\mu}_B} - \hat{\mu}_B n_B && \text{(5.29f)}
\end{aligned}$$

where in the last step we converted the derivative at constant μ_B into a derivative at constant $\hat{\mu}_B$. Using Eqs. (5.4) and (5.28) and the substitution $y = \hat{\mu}_B^2$, we can write the T-derivative

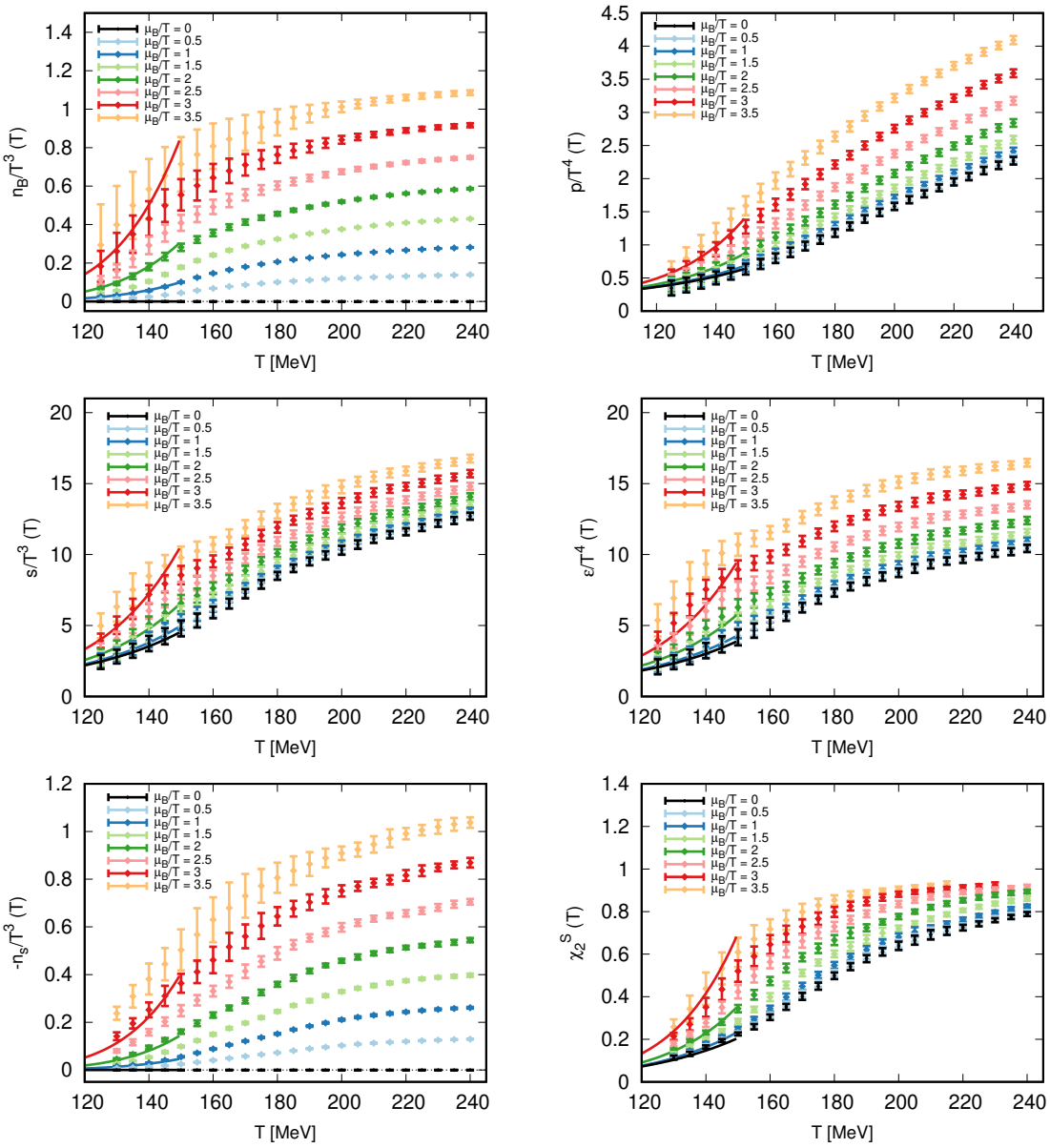

Figure 5.8: Baryon density, pressure, entropy, energy density, strangeness density and χ_2^S at increasing values of $\hat{\mu}_B$. With solid lines we show the results from the HRG model.

of the pressure, which involves the chain rule according to:

$$T\left.\frac{\partial\hat{p}(\hat{\mu}_B,T)}{\partial T}\right|_{\hat{\mu}} = T\left.\frac{\partial\hat{p}(0,T)}{\partial T}\right|_{\hat{\mu}} + \frac{1}{2}\int_0^{\hat{\mu}_B^2} T\left.\frac{d\chi_2^B(T')}{dT'}\right|_{T'=T\left(1+\kappa_2^{BB}y+\kappa_4^{BB}y^2\right)} \times$$
$$\times\left[1+\kappa_2^{BB}y+\kappa_4^{BB}y^2+T\left(\frac{d\kappa_2^{BB}}{dT}y+\frac{d\kappa_4^{BB}}{dT}y^2\right)\right]dy. \tag{5.30}$$

The dimensionless energy density $\hat{\epsilon}$ can be written as

$$\hat{\epsilon}(\hat{\mu}_B,T) = \hat{s}(\hat{\mu}_B,T) - \hat{p}(\hat{\mu}_B,T) + \hat{\mu}_B\hat{n}_B(\hat{\mu}_B,T). \tag{5.31}$$

The various panels of Fig. 5.8 show the baryon density, pressure, entropy, energy density, strangeness density and χ_2^S for $\hat{\mu}_B = 0 - 3.5$. Alongside our results, we show predictions from the HRG model for $T < 150\,\text{MeV}$, which we find in very good agreement with our extrapolation for all observables, at all values of the chemical potential. We also note that in all cases, the observables do not suffer from pathological behavior. The uncertainties are under control for our range of chemical potentials, which highly improves on the results currently achievable via Taylor expansion.

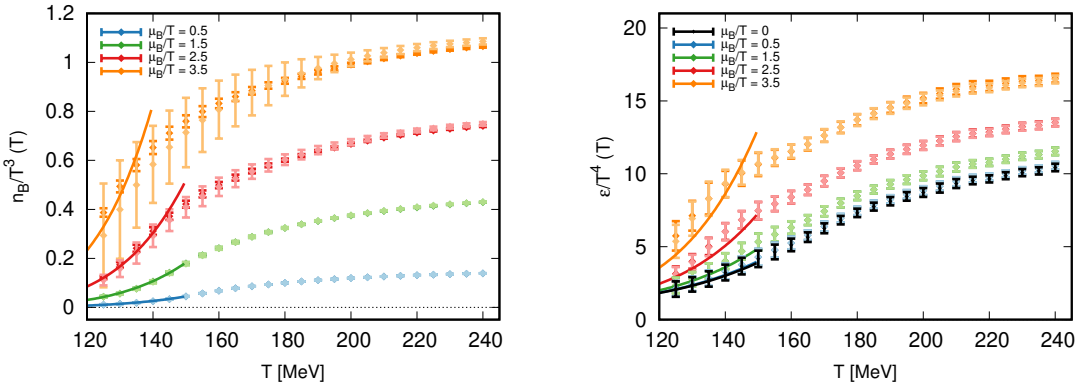

Figure 5.9: Comparison of baryon density (left) and energy density (right) at different values of $\hat{\mu}_B$ in the case where a κ_4^{BB} parameter is used (lighter shades) or omitted (darker shades). The HRG results are shown with solid lines.

We devote the two panels of Fig. 5.9 to the comparison of our results for the baryon density (left) and energy density (right) to the simplified case where κ_4^{BB} is neglected. We can appreciate how the inclusion of the next-to-leading-order parameter came at the cost of an increased uncertainty at larger chemical potential. This does not come unexpected, as we saw from our results that κ_4^{BB} was compatible with zero at all temperatures. In the case of the energy density, which is dominated by the $\mu_B = 0$ contribution, hardly any effect is visible.
We established a novel expansion scheme for the equation of state which is extrapolated to finite and real baryonic chemical potential $\mu_B/T \leq 3.5$ by setting $\mu_Q = 0 = \mu_S$. In the following chapter we extend this approach to the strangeness neutral (and beyond) case.

5.2 Strangeness neutrality and beyond

In the previous Sections we discussed a new expansion scheme for the equation of state extrapolated up to $\mu_B/T \leq 3.5$. Now we extend this approach by taking strangeness neutrality

and the small isospin asymmetry, which are relevant for heavy ion collision experiments, into account. Additionally, the Stefan-Boltzmann limits of the cumulants are included in the expansion scheme to improve its convergence in the high temperature region. Furthermore, we extrapolate the EoS to small non-zero values of the strangeness-to-baryon ratio $R = \langle S\rangle/\langle B\rangle$. While global strangeness neutrality is guaranteed in heavy ion collisions, local fluctuations can be large in the fluid cells used in hydrodynamic simulations. The following Sections are part of our works [144, 219, 220].

5.2.1 Strangeness neutrality

The conditions of heavy ion collisions are encoded in the following equations

$$\langle n_S\rangle = 0, \tag{5.32}$$

$$\frac{\langle n_Q\rangle}{\langle n_B\rangle} = 0.4. \tag{5.33}$$

The first one implies a global strangeness neutrality and the second encodes the slight isospin imbalance of the colliding nuclei (recall Section 3.3). We investigate the cases: 1) $\mu_Q = 0$: Isospin symmetry for which $\frac{\langle n_Q\rangle}{\langle n_B\rangle} = 0.5$ and 2) $\mu_Q \neq 0$: Isospin asymmetry for which $\frac{\langle n_Q\rangle}{\langle n_B\rangle} = 0.4$.
Let us start with

1. $\chi_1^S = 0$, $\chi_1^Q = 0.5\chi_1^B$ and hence $\mu_Q = 0$. By taking the derivative of $\frac{\mathrm{d}}{d\hat{\mu}_B}\langle n_S\rangle = 0$ as described in Section 3.3, we can write

$$\frac{\mathrm{d}\hat{\mu}_S}{\mathrm{d}\hat{\mu}_B} = -\frac{\chi_{11}^{BS}}{\chi_2^S}. \tag{5.34}$$

   Hence, total derivatives with respect to the baryochemical potential read

$$\frac{\mathrm{d}}{\mathrm{d}\hat{\mu}_B} = \frac{\partial}{\partial\hat{\mu}_B} + \frac{\mathrm{d}\hat{\mu}_S}{\mathrm{d}\hat{\mu}_B}\frac{\partial}{\partial\hat{\mu}_S} = \frac{\partial}{\partial\hat{\mu}_B} - \frac{\chi_{11}^{BS}}{\chi_2^S}\frac{\partial}{\partial\hat{\mu}_S}. \tag{5.35}$$

   We denote the total derivatives of the dimensionless pressure with respect to the baryochemical potential along the line $\mu_Q = 0$ and $\chi_1^S = 0$ as:

$$c_n^B(T,\hat{\mu}_B) := \left.\frac{\mathrm{d}^n\hat{p}(T,\hat{\mu}_B)}{\mathrm{d}\hat{\mu}_B^n}\right|_{\substack{\mu_Q=0\\ \chi_1^S=0}}. \tag{5.36}$$

   In this scheme, the leading coefficient

$$c_1^B(T,\hat{\mu}_B) = \chi_1^B - \frac{\chi_{11}^{BS}}{\chi_2^S}\chi_1^S = \chi_1^B, \tag{5.37}$$

   gives the net baryon density.

2. $\chi_1^S = 0$, $0.4\chi_1^B = \chi_1^Q$ and hence $\mu_Q \neq 0$. These conditions define a curve in the μ_B-μ_S-μ_Q space. Along this curve the total derivatives are:

$$\frac{\mathrm{d}}{\mathrm{d}\hat{\mu}_B} = \frac{\partial}{\partial\hat{\mu}_B} + \frac{\mathrm{d}\hat{\mu}_S}{\mathrm{d}\hat{\mu}_B}\frac{\partial}{\partial\hat{\mu}_S} + \frac{\mathrm{d}\hat{\mu}_Q}{\mathrm{d}\hat{\mu}_B}\frac{\partial}{\partial\hat{\mu}_Q}. \tag{5.38}$$

Applying this total derivative to the constraints $\chi_1^S = 0$ and $0.4\chi_1^B = \chi_1^Q$, we get

$$\chi_{11}^{BS} + \chi_{11}^{SQ}\frac{\mathrm{d}\hat{\mu}_Q}{\mathrm{d}\hat{\mu}_B} + \chi_2^S\frac{\mathrm{d}\hat{\mu}_S}{\mathrm{d}\hat{\mu}_B} = 0, \tag{5.39}$$

$$\chi_{11}^{BQ} + \chi_{11}^{SQ}\frac{\mathrm{d}\hat{\mu}_S}{\mathrm{d}\hat{\mu}_B} + \chi_2^Q\frac{\mathrm{d}\hat{\mu}_Q}{\mathrm{d}\hat{\mu}_B} = 0.4\left(\chi_2^B + \chi_{11}^{BS}\frac{\mathrm{d}\hat{\mu}_S}{\mathrm{d}\hat{\mu}_B} + \chi_{11}^{BQ}\frac{\mathrm{d}\hat{\mu}_Q}{\mathrm{d}\hat{\mu}_B}\right) \tag{5.40}$$

Along this line, total derivatives will be denoted by:

$$d_n^B(T,\hat{\mu}_B) \equiv \left.\frac{\mathrm{d}^n\hat{p}(T,\hat{\mu}_B)}{\mathrm{d}\hat{\mu}_B^n}\right|_{\substack{\chi_1^Q=0.4\chi_1^B \\ \chi_1^S=0}}. \tag{5.41}$$

For simplicity, we mostly use the first set of conditions with $\mu_Q = 0$. In Section 5.2.4 we consider the difference between the two schemes in the leading order of the Taylor expansion - i.e. we will calculate $c_2^B(T,0)$ and $d_2^B(T,0)$ and their temperature derivatives.

5.2.2 Formalism

The ansatz of Eq. (5.4) can be generalized to

$$F(T,\hat{\mu}_B) = F(T(1+\kappa_2^F(T)\hat{\mu}_B^2 + \kappa_4^F(T)\hat{\mu}_B^4 + \dots),0), \tag{5.42}$$

where F is some observable of interest, of sigmoid shape in the temperature, such as $\chi_1^B/\hat{\mu}_B$. The superscripts on the κ_n^F denote that the expansion coefficients are different for different observables. Before describing our improved extrapolation ansatz, we note that the ansatz given by Eq. (5.42), introduced for $\mu_S = 0$, would also work at strangeness neutrality. The

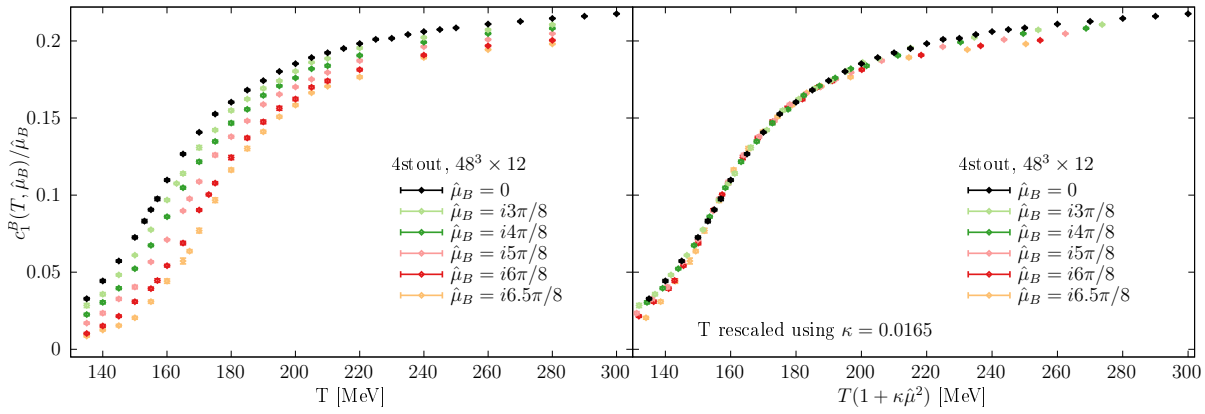

Figure 5.10: Left: The total derivative c_1^B on the strangeness neutral line from our imaginary chemical potential simulations. The data points at $\mu_B = 0$ show the second derivative $\frac{\mathrm{d}^2\hat{p}}{\mathrm{d}\hat{\mu}_B^2}$. Right: Same observables, with the temperature rescaled by a factor $1 + \kappa\hat{\mu}_B^2$.

existence of the approximate scaling variable on the strangeness neutral line is shown in Fig. 5.10 for the quantity c_1^B/μ_B, where on the left panel we show the data points of our simulations for a $48^3 \times 12$ lattice, while on the right panel we show the same data points as a function of a rescaled temperature $T(1 + \kappa\hat{\mu}^2)$. Notice that the collapse plot with a

constant κ does not work quite as well at high temperatures. Indeed, one does not expect an approximate scaling variable outside the crossover range. Our scheme can still incorporate this behavior by the temperature dependence of the κ_n coefficients. In fact, with the ansatz given by Eq. (5.42) the coefficient κ_2 grows at high temperatures.

One shortcoming of this scheme is that the region of applicability is restricted by the Stefan-Boltzmann limit of the right hand side of Eq. (5.42). When the quantity $F(T, \hat{\mu}_B)$ gets larger than its infinite temperature limit at $\mu_B = 0$, the ansatz in Eq. (5.42) must break down. It is easy to address this shortcoming however, using the scheme only for observables F that have an infinite temperature limit that is independent of $\hat{\mu}_B$. Given an observable that does not possess this property, one can easily construct another observable, by simply dividing by its own Stefan-Boltzmann limit:

$$F(T, \hat{\mu}_B) \to \frac{F(T, \hat{\mu}_B)}{\overline{F}(\hat{\mu}_B)}, \tag{5.43}$$

where the Stefan-Boltzmann limits are denoted by (we always use the continuum limits)

$$\overline{F}(\hat{\mu}_B) = \lim_{T\to\infty} F(T, \hat{\mu}_B). \tag{5.44}$$

By using the ansatz from Eq. (5.42) on this Stefan-Boltzmann corrected observable, we arrive at our new scheme, given by

$$\frac{F(T, \hat{\mu}_B)}{\overline{F}(\hat{\mu}_B)} = \frac{F(T'_F, 0)}{\overline{F}(0)}, \tag{5.45}$$

where the temperature on the right hand side is expanded as

$$T'_F = T\left(1 + \lambda_2^F(T)\hat{\mu}_B^2 + \lambda_4^F(T)\hat{\mu}_B^4 + \dots\right). \tag{5.46}$$

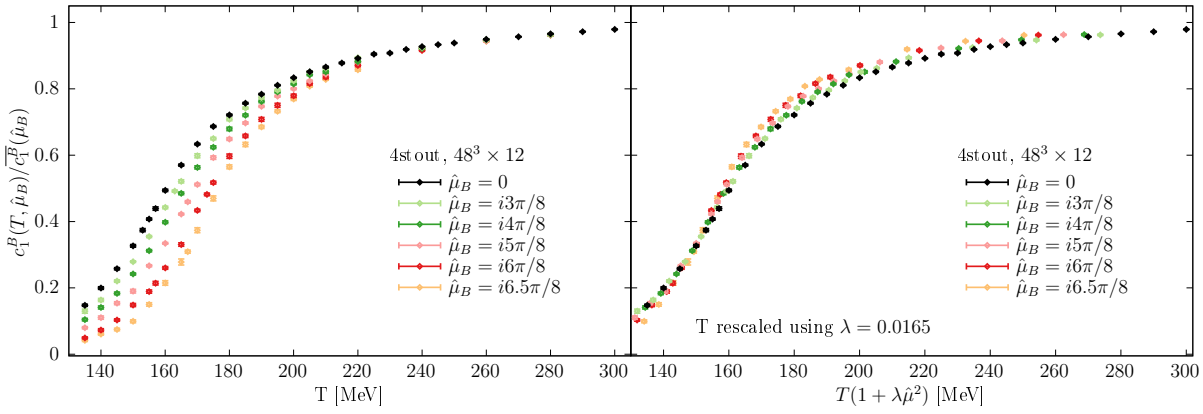

Figure 5.11: Left: The scaled total derivative $c_1^B/\hat{\mu}_B$ on the strangeness neutral line from our imaginary chemical potential simulations, divided by its chemical potential dependent Stefan-Boltzmann limit. The data points at $\mu_B = 0$ show the second derivative c_2^B divided by its Stefan-Boltzmann limit. Right: Same observables, with the temperature rescaled by a factor $1 + \lambda\hat{\mu}_B^2$.

As is shown in Fig. 5.11, this Stefan-Boltzmann correction does not spoil the collapse plot in the approximate scaling variable, meaning that the fast convergence of the scheme in the

crossover region is maintained, with a $\lambda_2(T)$ coefficient that is approximately constant in the crossover range. The limitation at high temperature is however removed. Furthermore, as can be seen on the left panel of Fig. 5.11, the coefficients λ_n must go to zero at high temperatures, as the data points for the different imaginary chemical potentials almost overlap. This is in contrast to the scheme of Eq. (5.42), where κ_2 grows at high temperatures.
In this work, we study three different observables F:

1. First, we study the normalized net baryon density $F = c_1^B/\hat{\mu}_B$. By noticing that $\lim_{\hat{\mu}_B \to 0} \frac{c_1^B(T,\hat{\mu}_B)}{\hat{\mu}_B} = c_2^B(T,0)$, Eq. (5.45) can be written as

$$\frac{c_1^B(T,\hat{\mu}_B)}{\overline{c_1^B}(\hat{\mu}_B)} = \frac{c_2^B(T'_{BB},0)}{\overline{c_2^B}(0)}, \tag{5.47}$$

where the infinite temperature limits of c_1^B and c_2^B are denoted $\overline{c_1^B}$ and $\overline{c_2^B}$ respectively, and

$$T'_{BB} \equiv T(1 + \lambda_2^{BB}(T)\hat{\mu}_B^2 + \lambda_4^{BB}(T)\hat{\mu}_B^4 + \dots). \tag{5.48}$$

The Stefan-Boltzmann limits are :

$$\overline{c_1^B}(\hat{\mu}_B) = \hat{\mu}_B \overline{c_2^B}(0) + \hat{\mu}_B^3 \overline{c_4^B}(0), \tag{5.49}$$

$$\overline{c_2^B}(0) = \frac{2}{9} \qquad \overline{c_4^B}(0) = \frac{4}{27\pi^2}. \tag{5.50}$$

The Stefan-Boltzmann limit denotes the infinite temperature limit and reads in lowest order in perturbation theory for the pressure [221]

$$\frac{p^{\mathrm{SB}}}{T^4} = \frac{19\pi^2}{36} + \sum_{i=u,d,s} \left(\frac{\mu_i^2}{2T^2} + \frac{\mu_i^4}{4\pi^2 T^4} \right). \tag{5.51}$$

Using the transformations Eqs. (3.61) to (3.63) the Stefan-Boltzmann limits of the corresponding observables can be calculated.

2. Second, we study the normalized strangeness chemical potential that is needed to realize the $\chi_1^S \equiv 0$ condition in a grand canonical ensemble: $F = \mathrm{M}(\mathrm{T}, \hat{\mu}_\mathrm{B}) \equiv \frac{\hat{\mu}_\mathrm{S}}{\hat{\mu}_\mathrm{B}}(\mathrm{T}, \hat{\mu}_\mathrm{B})$. Since

$$\lim_{\hat{\mu}_B \to 0} \mathrm{M}(\mathrm{T}, \hat{\mu}_\mathrm{B}) = -\frac{\chi_{11}^{\mathrm{BS}}(\mathrm{T},0)}{\chi_2^{\mathrm{S}}(\mathrm{T},0)} \equiv \mathrm{M}(\mathrm{T},0), \tag{5.52}$$

Eq. (5.45) becomes:

$$\frac{\mathrm{M}(\mathrm{T}, \hat{\mu}_\mathrm{B})}{\overline{\mathrm{M}}(\hat{\mu}_B)} = \frac{\mathrm{M}(\mathrm{T}'_{\mathrm{BS}},0)}{\overline{\mathrm{M}}(0)}, \tag{5.53}$$

with the Stefan Boltzmann limit $\overline{\mathrm{M}}(\hat{\mu}_B) = \lim_{T\to\infty} \mathrm{M}(\mathrm{T}, \hat{\mu}_\mathrm{B})$ and

$$T'_{BS} = T(1 + \lambda_2^{BS}(T)\hat{\mu}_B^2 + \lambda_4^{BS}(T)\hat{\mu}_B^4 + \dots). \tag{5.54}$$

3. Finally, we study $F = \chi_2^S$, and denote its Stefan-Boltzmann limit by $\overline{\chi_2^S}$. For this observable, Eq. (5.45) reads:

$$\frac{\chi_2^S(T,\hat{\mu}_B)}{\overline{\chi_2^S}(\hat{\mu}_B)} = \frac{\chi_2^S(T'_{SS},0)}{\overline{\chi_2^S}(0)}, \tag{5.55}$$

where

$$T'_{SS} = T(1 + \lambda_2^{SS}(T)\hat{\mu}_B^2 + \lambda_4^{SS}(T)\hat{\mu}_B^4 + \dots). \tag{5.56}$$

Note that, at strangeness neutrality, the Stefan-Boltzmann limits of M and χ_2^S are independent of $\hat{\mu}_B$,

$$\overline{\mathrm{M}}(\hat{\mu}_B) = \hat{\mu}_B \overline{\mathrm{M}}(0)\,, \qquad \overline{\chi_2^S}(\hat{\mu}_B) = 1\,, \tag{5.57}$$

thus $\kappa_n^{BS} = \lambda_n^{BS}$ and $\kappa_n^{SS} = \lambda_n^{SS}$.

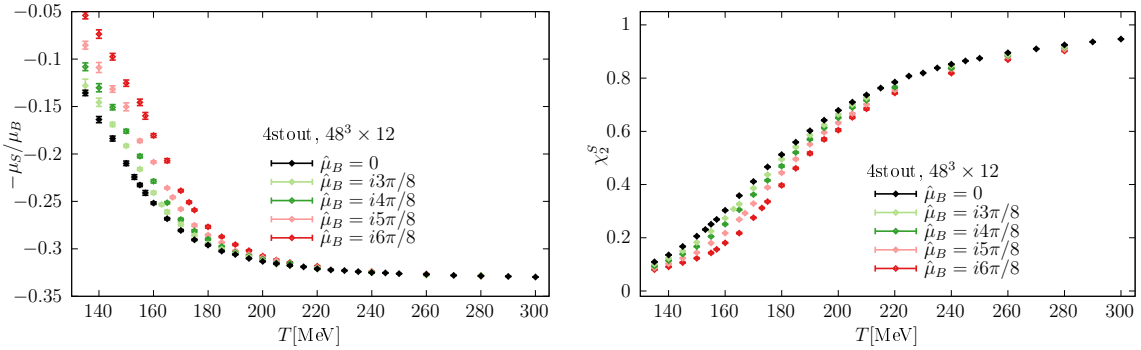

Figure 5.12: The strangeness to baryon chemical potential ratio (left panel) and the strangeness susceptibility (right panel) at simulated imaginary baryochemical potentials on our $48^3 \times 12$ ensembles.

We show the lattice data for M and χ_2^S on our $48^3 \times 12$ ensembles in Fig. 5.12.

5.2.3 Simulation details

The simulation setup is similar as the one described in Section 5.1.2, but not completely identical. For the scale setting we use again either the pion decay constant $f_\pi = 130.41$ MeV or the Wilson flow based $w_0 = 0.1725$ fm scale [152]. We use lattices of temporal extent $N_\tau = 8, 10, 12$ and 16 to perform a continuum limit. The spatial volume is given by the aspect ratio of $LT = 4$. We performed simulations for imaginary baryochemical potentials given by $\mathrm{Im}\,\hat{\mu}_B \frac{8}{\pi} = 0, 3, 4, 5, 6, 6.5$. In addition, for the $N_\tau = 12$ lattices we also have data at $\mathrm{Im}\,\hat{\mu}_B \frac{8}{\pi} = 5.5$. Strangeness neutrality was enforced on our imaginary chemical potential ensembles via the procedure discussed in [33, 156].

5.2.4 Continuum result of c_2^B, d_2^B and their temperature derivatives

In contrast to the previous project, we take strangeness neutrality into account and hence deal with c_2^B or d_2^B instead of χ_2^B. Similarly as described in Section 5.1.4, we need the continuum extrapolation and their temperature derivative at $\mu_B = 0$ for thermodynamic quantities such as entropy or energy density. The analysis is similar as the one described in Section 5.1.4 with slight changes: We concatenate the resulting functions at $T = 250$ MeV this time and the known Stefan-Boltzmann limit is not enforced in the constant term of the polynomial fit in $1/T$. Hence, the fitted value of the constant is not equal to the known infinite temperature limit, and our fit only allows for interpolation in the range where we have lattice data. The region where the two ansätze overlap give consistent results in the temperature range between 200 MeV and 280 MeV for both c_2^B and its T derivative. Final results for $c_2^B(T, 0)$ and its logarithmic temperature derivative are shown in Fig. 5.13.

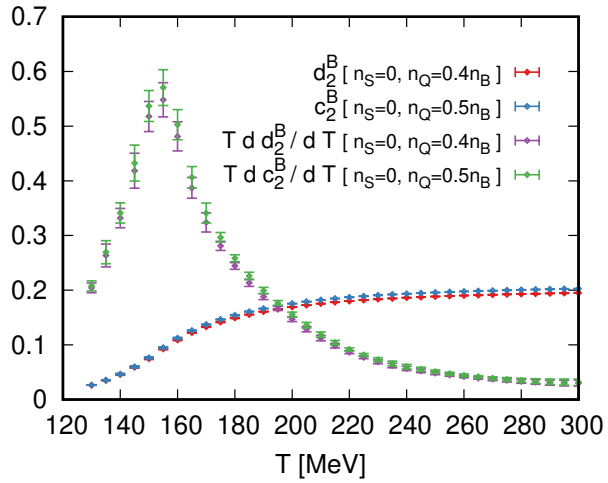

Figure 5.13: $c_2^B(T, \hat{\mu}_B = 0)$, $d_2^B(T, \hat{\mu}_B = 0)$ and their logarithmic temperature derivatives in the continuum limit, as extrapolated from our $N_\tau = 10, 12$ and 16 lattices.

We also performed the same analysis for $d_2^B(T, 0)$, corresponding to $\chi_Q = 0.4\chi_B$. The results for this quantity and its temperature derivative are also shown in Fig. 5.13. At high temperatures, there is a small but statistically significant difference between d_2^B and c_2^B. The difference of these Taylor coefficients leads to a small difference between the leading order chemical potential dependence in these two cases for high temperatures. The next corrections, corresponding to the λ_n^{BB} coefficients of our resummation scheme, would probably also slightly differ in the two cases, but our lattice results are not yet precise enough to detect this difference. Therefore, we go on with the $\mu_Q = 0$ setting for simplicity.

5.2.5 The coefficients λ_2^{ij} and λ_4^{ij}

We follow a similar strategy as described in Section 5.1.3 to obtain the coefficients λ_2^{ij} and λ_4^{ij}. Hence let us briefly discuss the main aspects of the analysis to avoid repetitions.
We can define the quantity

$$\Pi(T, \hat{\mu}_B, N_t) = \frac{T'(T, \hat{\mu}_B, N_t) - T}{T\hat{\mu}_B} \tag{5.58a}$$

$$= \lambda_2^{ij} + \lambda_4^{ij}\hat{\mu}_B^2 + \lambda_6^{ij}\hat{\mu}_B^4 + \dots \tag{5.58b}$$

which allows us to calculate the coefficients in the following way.

1. Denoting by A either one of the observables c_1^B, $\mathrm{M} = \frac{\mu_S}{\mu_B}$ or χ_2^S and calling B one of c_2^B, $-\frac{\chi_{11}^{BS}}{\chi_2^S}$ or χ_2^S respectively, and denoting the corresponding Stefan-Boltzmann corrected observables by $\tilde{A} = A/\overline{A}$ and $\tilde{B} = B/\overline{B}$ respectively, our extrapolation ansatz is defined as
$$\tilde{A}(T, \hat{\mu}_B) = \tilde{B}(T', 0). \tag{5.59}$$

2. Spline interpolations are performed for $\tilde{A}$ at finite imaginary μ_B and for $\tilde{B}$ at $\mu_B = 0$. Matching both observables for several temperatures T and imaginary μ_B defines $T'(T, \mu_B)$. This procedure is illustrated in Fig. 5.14.

3. The $T'(T, \mu_B)$ values are used for the proxy $\Pi(T, \hat{\mu}_B, N_t)$ which determines the coefficients λ_2^{ij} and λ_4^{ij}.

4. Continuum extrapolation of Π follows the ansatz

$$\Pi(T, \hat{\mu}_B, N_t) = \lambda_2^A + \lambda_4^A \hat{\mu}_B^2 + \lambda_6^A \hat{\mu}_B^4 + \frac{1}{N_t^2}\left(\alpha^A + \beta^A \hat{\mu}_B^2 + \gamma^A \hat{\mu}_B^4\right), \tag{5.60}$$

where we either fix $\lambda_6^A = \gamma^A = 0$ or leave both as free parameters in the fit.

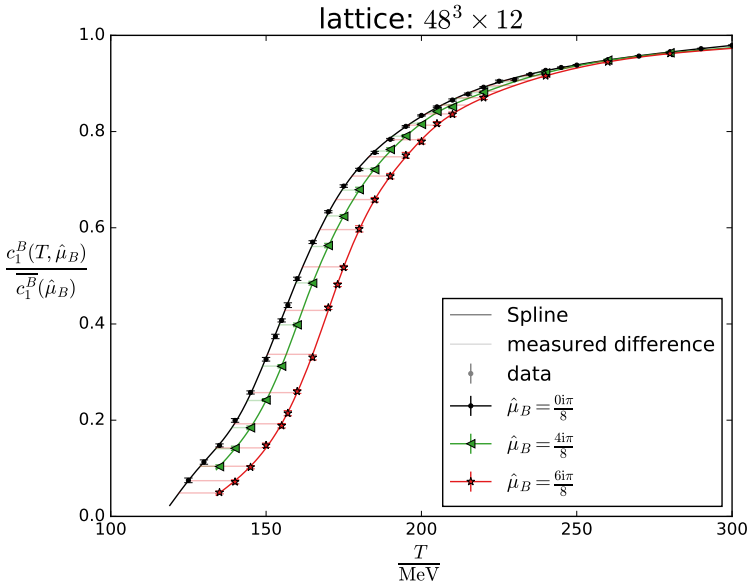

Figure 5.14: Illustration of the rescaled temperatures T'_{BB} determination by spline fits to the data at zero and imaginary baryochemical potential. In this case, the $\mu_B = 0$ data correspond to $c_2^B(T, 0)$.

The different choices in the analysis procedure include:

- 3 different sets of spline node points at μ_B=0
- 2 different sets of spline node points at finite imaginary μ_B
- w_0 or f_π based scale setting
- 2 different chemical potential ranges in the global fit: $\hat{\mu}_B \leq 5.5$ or $\hat{\mu}_B \leq 6.5$
- 2 functions for the chemical potential dependence of the global fit: linear or parabola
- including the coarsest lattice, $N_\tau = 8$, or not, in the continuum extrapolation.

This amounts to a total of $96 = 3 \times 2^5$ fits entering the systematic error estimation. As described in Section 5.1.3, we perform a correlated polynomial temperature fit for λ_2^{ij} and λ_4^{ij} to obtain the temperature derivatives needed for the calculation of e.g. the entropy. Results are shown in Fig. 5.15. In contrast to our previous approach (right side of Fig. 5.15) which does not take the Stefan-Boltzmann correction into account (recall Section 5.1), the coefficients λ_2 (except λ_2^{SS}) tend to zero within error bars at the higher end of our temperature

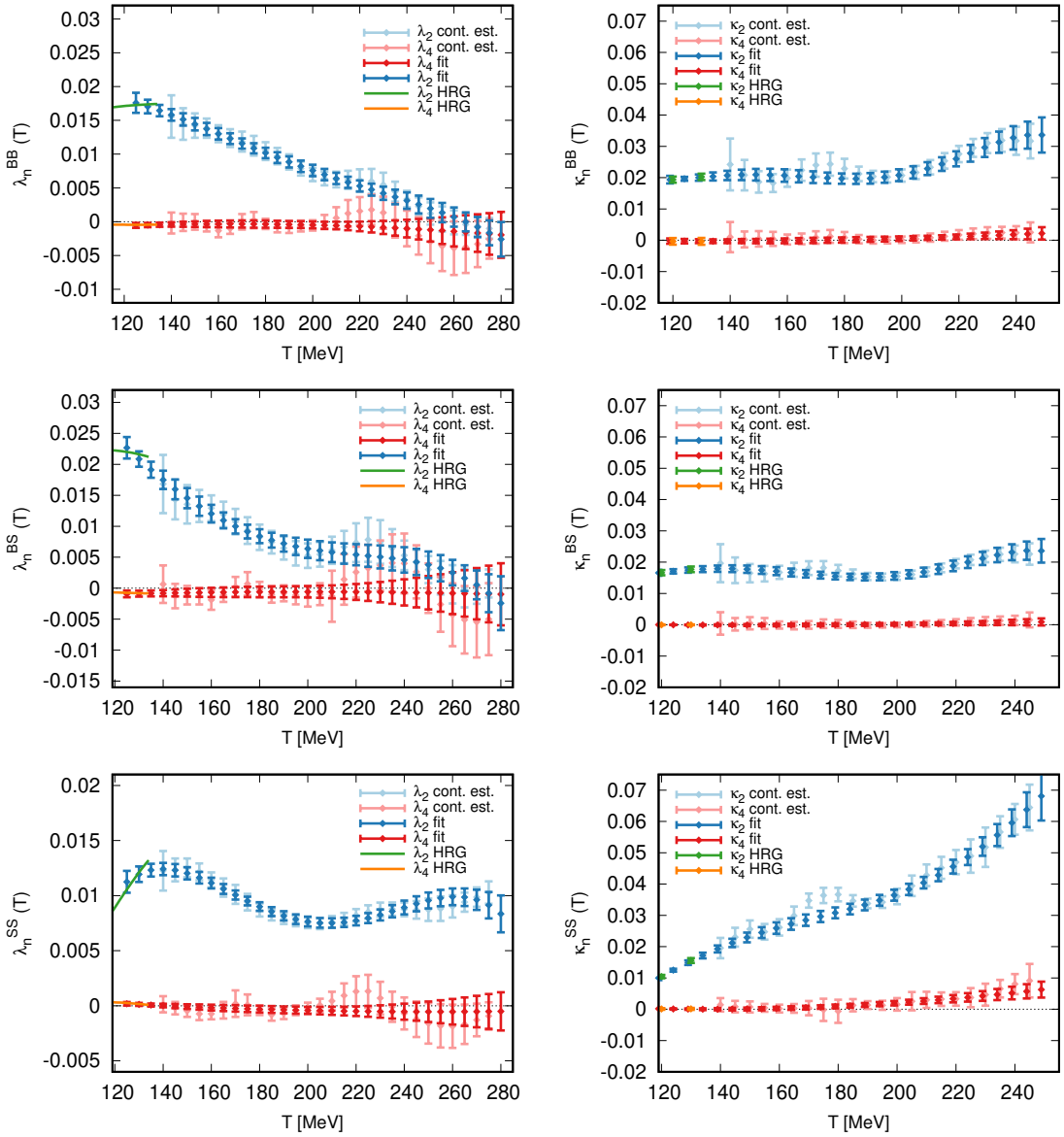

Figure 5.15: Left side: λ_n^{BB} (top panel), λ_n^{BS} (middle panel) and λ_n^{SS} (bottom panel) in the continuum. They indicate our Stefan-Boltzmann corrected approach. Also shown are the fits used to estimate the temperature derivative of these coefficients, as well as predictions of the HRG model, which we use to constrain the fits at low temperatures. On the right side are the plots of Fig. 5.6 (right side), $\kappa_n^{BB}(T)$ (top panel), $\kappa_n^{BS}(T)$ (central panel) and $\kappa_n^{SS}(T)$ and (bottom panel). They correspond to the approach which is not Stefan-Boltzmann corrected.

range, as expected. Furthermore, all of the λ_2 and κ_2 coefficients are approximately constant in the crossover range, as is expected from the existence of the approximate scaling variable (be aware of the different ranges of the y-axis). The λ_2^{SS} is still non-zero, as the strangeness susceptibility χ_2^S tends to its Stefan-Boltzmann limit more slowly, due to the larger strange quark mass.

5.2.6 Thermodynamics at real chemical potential

We follow the calculations of Section 5.1.5 to obtain the pressure, energy density and entropy. The major difference is the strangeness neutrality condition, so the equations have to be

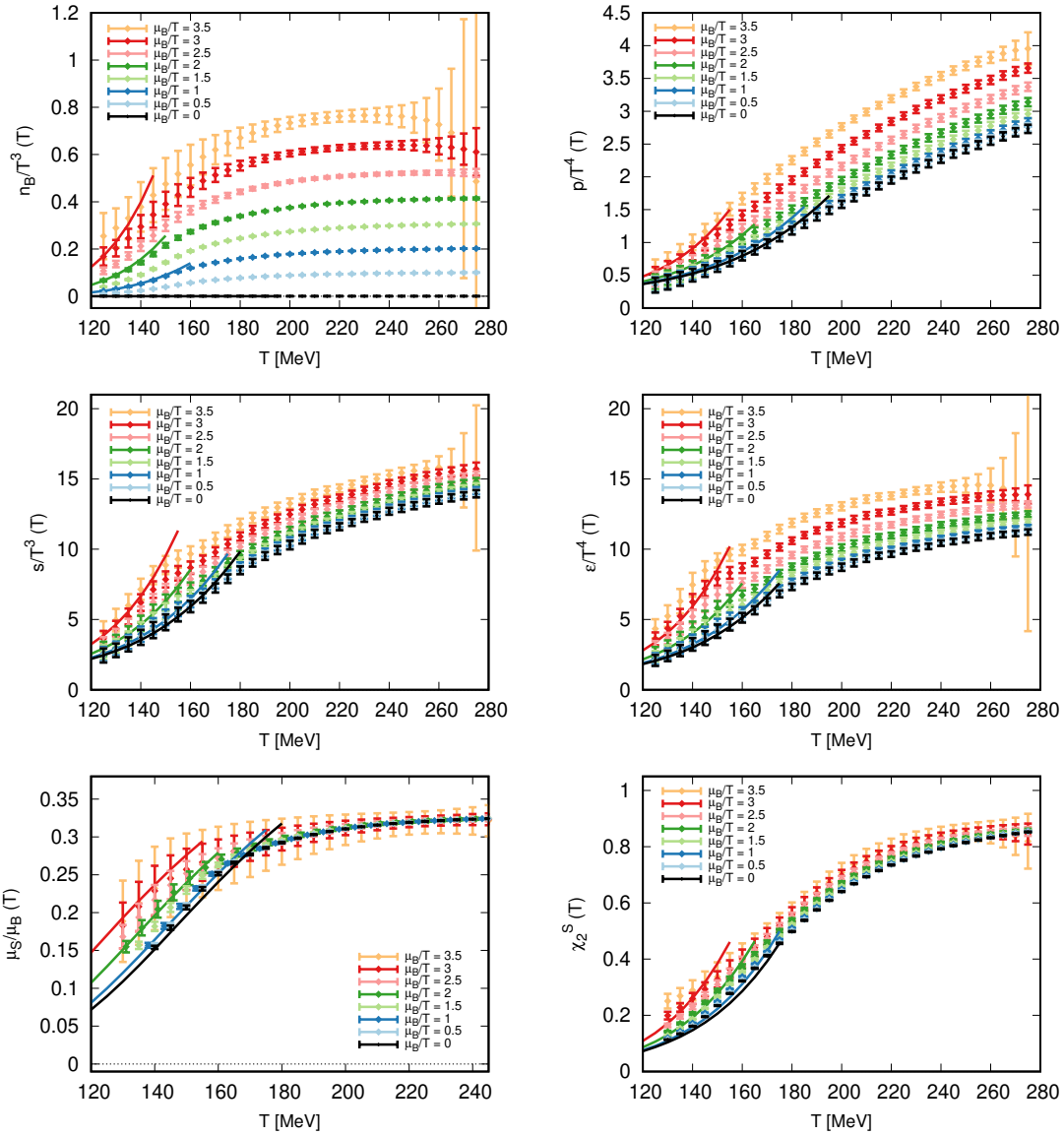

Figure 5.16: The dimensionless baryon density (top left panel), pressure (top right panel), entropy (middle left panel), energy density (middle right panel), strangeness chemical potential to baryochemical potential ratio (bottom left panel) and strangeness susceptibility (bottom right panel) as functions of temperature at different values of the real chemical potential. The solid lines always show the predictions of the hadron resonance gas model for the corresponding temperature.

slightly changed. For the pressure, we calculate the following integral

$$\frac{p(T,\hat{\mu}_B)}{T^4} = \frac{p(T,0)}{T^4} + \int_0^{\hat{\mu}_B} c_1^B(T,\hat{\mu}'_B)\mathrm{d}\hat{\mu}'_B, \tag{5.61}$$

with

$$c_1^B(T,\hat{\mu}_B) = c_2^B(T',0)\frac{\overline{c_1^B}(\hat{\mu}_B)}{\overline{c_2^B}(0)}, \tag{5.62}$$

As before, the pressure at zero chemical potential is taken from [209]. For the entropy (recall the derivation of Eq. (5.29f))

$$\hat{s}(\hat{\mu_B},T) = 4\hat{p} + T\frac{\partial\hat{p}}{\partial T}\bigg|_{\hat{\mu}_B} - \hat{\mu}_B\chi_1^B, \tag{5.63}$$

we need the temperature derivative of the pressure again - but this time along the strangeness neutral line, leading to

$$\begin{aligned} T\left.\frac{\partial\hat{p}(T,\hat{\mu}_B)}{\partial T}\right|_{\hat{\mu}} &= T\frac{\partial\hat{p}(T,0)}{\partial T} + \frac{1}{2}\int_0^{\hat{\mu}_B^2} T\left.\frac{\mathrm{d}c_2^B(T',0)}{\mathrm{d}T'}\right|_{T'=T\left(1+\lambda_2^{BB}y+\lambda_4^{BB}y^2\right)} \times \\ &\times\left[1+\lambda_2^{BB}y+\lambda_4^{BB}y^2+T\left(\frac{\mathrm{d}\lambda_2^{BB}}{dT}y+\frac{\mathrm{d}\lambda_4^{BB}}{dT}y^2\right)\right]dy. \end{aligned} \tag{5.64}$$

The continuum estimates of the dimensionless baryon number, pressure, entropy density, energy density, μ_S/μ_B ratio and strangeness susceptibility - as computed from the expansion coefficients up to order λ_4^{ij} - are shown in the various panels of Fig. 5.16. Even with the inclusion of the λ_4^{ij} coefficients, the statistical errors of our results stay well under control in the chemical potential range we study. Similarly to our previous results for the $\mu_Q = \mu_S = 0$ case (see Fig. 5.8) none of the observables display the pathological oscillations typical of truncated Taylor expansions.

5.2.7 Beyond strangeness neutrality

So far we extrapolated the pressure and the corresponding thermodynamic quantities along the strangeness neutral line. These results can be used to perform extrapolations to small values of the strangeness density, slightly off the $\chi_1^S = 0$ line. Let us denote the value of the dimensionless strange quark chemical potential that solves $\chi_1^S = 0$ at fixed T and $\hat{\mu}_B$ as $\hat{\mu}_S^*$. Still considering a fixed $\hat{\mu}_B$ and T, but changing $\hat{\mu}_S$ slightly from the strangeness neutral choice by a small amount

$$\Delta\hat{\mu}_S \equiv \hat{\mu}_S - \hat{\mu}_S^\star, \tag{5.65}$$

the dimensionless strangeness and baryon densities read at leading order in $\Delta\hat{\mu}_S$

$$\chi_1^S(\hat{\mu}_S) \approx \chi_2^S(\hat{\mu}_S^\star)\Delta\hat{\mu}_S, \tag{5.66}$$

$$\chi_1^B(\hat{\mu}_S) \approx \chi_1^B(\hat{\mu}_S^\star) + \chi_{11}^{BS}(\hat{\mu}_S^\star)\Delta\hat{\mu}_S, \tag{5.67}$$

We perform the extrapolation beyond strangeness neutrality in terms of the strangeness-to-baryon ratio

$$R = \frac{\chi_1^S}{\chi_1^B} = \frac{\chi_2^S(\hat{\mu}_S^\star)\Delta\hat{\mu}_S}{\chi_1^B(\hat{\mu}_S^\star)\Delta\hat{\mu}_S + \chi_{11}^{BS}(\hat{\mu}_S^\star)}, \tag{5.68}$$

which can be inverted to obtain

$$\Delta\hat{\mu}_S = \frac{R\chi_1^B(\hat{\mu}_S^\star)}{\chi_2^S(\hat{\mu}_S^\star) - R\chi_{11}^{BS}(\hat{\mu}_S^\star)}. \tag{5.69}$$

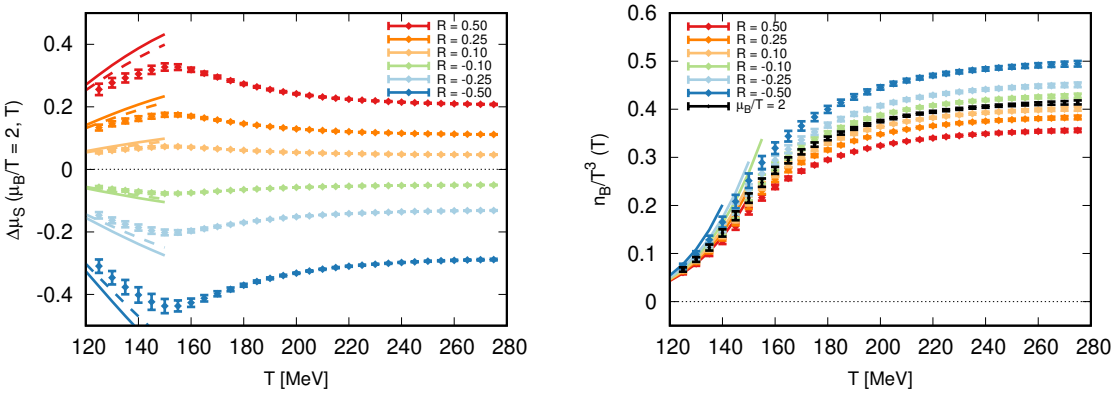

Figure 5.17: Left: Shift of the strangeness chemical potential as a function of the temperature at $\hat{\mu}_B = 2$, at various values of the strangeness-to-baryon ratio $R = \chi_1^S/\chi_1^B$. The solid lines show the exact solution of $R = \chi_1^S/\chi_1^B$ HRG, while the dashed lines show the evaluation of the approximation of Eq. (5.69) in the HRG model. Right: Dimensionless baryon density as a function of the temperature at $\hat{\mu}_B = 2$, for various values of the strangeness-to-baryon $R = \chi_1^S/\chi_1^B$.

Then, we simply note that

$$\begin{aligned} -\frac{\chi_{11}^{BS}}{\chi_2^S} &= \frac{\mathrm{d}\hat{\mu}_S}{\mathrm{d}\hat{\mu}_B} \\ &= \frac{\mathrm{d}}{\mathrm{d}\hat{\mu}_B}\left[\hat{\mu}_B f_{BS}(T'_{BS}(T,\hat{\mu}_B))\right] \\ &= \hat{\mu}_B\left[f_{BS}(T'_{BS}) + \frac{\partial f_{BS}(T'_{BS}(T,\hat{\mu}_B))}{\partial\hat{\mu}_B}\right], \end{aligned} \tag{5.70}$$

where we used the shorthand notation $f_{BS}(T) \equiv \mathrm{M(T,0)} = -\frac{\chi_{11}^{\mathrm{BS}}}{\chi_2^{\mathrm{S}}}(\mathrm{T}, \hat{\mu}_{\mathrm{B}} = 0)$. The quantity $\Delta\hat{\mu}_S$ is shown for $\hat{\mu}_B = 2$ as a function of temperature for various value of R in the left panel Fig. 5.17. Substituting Eq. (5.69) into Eq. (5.67) we obtain - to leading order in R

$$\frac{\chi_1^B(T, \hat{\mu}_B, R)}{\chi_1^B(T, \hat{\mu}_B, R=0)} \approx 1 + R\frac{\chi_{11}^{BS}(T, \hat{\mu}_B, R=0)}{\chi_2^S(T, \hat{\mu}_B, R=0)}, \tag{5.71}$$

where all quantities on the right hand side are along the strangeness neutral line. Results for the dimensionless baryon density at $\hat{\mu}_B = 2$ for several values of R are presented on the right panel of Fig. 5.17.

6 Finite volume effects of the QCD crossover at finite density

The thermal transition of QCD for physical quark masses and vanishing chemical potential is an analytic crossover [12]. Finite size scaling using aspect ratios $LT = 4, 5, 6$ specified the transition as analytic since the peak of the chiral susceptibility basically shows no or a mild volume dependence. Further studies of the EoS demonstrated that the main driver of uncertainties are not finite volume effects, but instead cut-off effects which lead to taste-violation in the case of staggered quarks [141]. Especially the observation that there is basically no volume dependence in the transition region contributed to the unspoken common standard in the community to choose $LT = 4$ to study the thermal properties of QCD (as we did in the last Chapter). Nevertheless finite volume effects play a crucial role phenomenologically and theoretically. The fireball produced in heavy-ion collisions is of finite size and if the crossover turns into a real transition, volume effects get more and more severe. Furthermore, the study of finite volume effects is important for reweighting methods which are up to now restricted to smaller physical volumes (see e.g. [175,222]). Recent studies employing phase [223] ($LT = 2$) or sign reweighting [224] ($LT \approx 2.7$) use small volumes to reduce the overlap problem. One motivation of the following Section is to identify physical observables with milder finite volume effects, which can then later be calculated up to higher chemical potentials with such reweighting methods. Moreover, the calculation of higher-order (baryon) fluctuations which are essential to reconstruct the EoS, is challenging on large volumes. The central limit theorem dictates that for large volumes the high order baryon fluctuations (beyond 2^{nd} order) are suppressed due to the ideal underlying Gaussian distribution [225, 226]. In the following Section we investigate finite volume effects of observables related to the chiral and deconfinement analytic transition at finite density. Therefore, we use again simulations at imaginary chemical potential and investigate the strength and width of the transition on $N_t = 12$. The following Sections are part of our works [227, 228].

6.1 Simulation details

The lattice setup is similar to the one used in Chapter 5: We use a tree-level Symanzik improved gauge action and four steps of stout smearing in the staggered fermion action. The quark masses are tuned such that the pion and kaon masses are equal to 135 MeV and 495 MeV. The scale is set with the pion decay constant $f_\pi = 130.41$ MeV. We use lattices with $N_\tau = 12$ timeslices. We use several physical volumes, with the number of spatial sites $N_s = 20, 24, 28, 32, 40, 48$ and 64 for the $\mu_B = 0$ simulations. For three of the spatial volumes ($N_s = 32, 40$ and 48) we also simulate at a purely imaginary chemical potential, with $\frac{\mu_B}{T}\frac{8}{\pi} = 3, 4, 5, 6, 6.5$ and 7. Throughout this Section, we always use a strangeness chemical potential μ_S tuned in such a way that the expectation value of strangeness is equal to zero.

6.2 Chiral observables

To investigate the chiral aspects of the QCD crossover we calculate the chiral condensate $\left\langle \bar{\psi}\psi \right\rangle$ and the chiral susceptibility χ defined respectively as:

$$\langle \bar{\psi}\psi \rangle = \frac{T}{V}\frac{\partial \log Z}{\partial m_{ud}}, \qquad \chi = \frac{T}{V}\frac{\partial^2 \log Z}{\partial m_{ud}^2}. \tag{6.1}$$

In the limit of zero quark masses $\langle \bar{\psi}\psi \rangle$ is a true order parameter of the chiral phase transition. In terms of the the discretized (massive) Dirac operator for the up and down quarks M_{ud}, the chiral condensate is written as

$$\langle \bar{\psi}\psi \rangle = \frac{1}{2}\frac{T}{V}\left\langle \mathrm{Tr}\, M_{ud}^{-1} \right\rangle, \tag{6.2}$$

where $\langle \dots \rangle$ stands for the expectation value over the gauge fields and the factor $\frac{1}{2}$ appears due to staggered rooting. In lattice language, the order parameter is then proportional to the trace $\mathrm{Tr}\, M_{ud}^{-1}$. We will also study the disconnected part of the chiral susceptibility, defined as

$$\chi_{\mathrm{disc}} = \frac{1}{4}\frac{T}{V}\left(\left\langle \left(\mathrm{Tr}\, M_{ud}^{-1} \right)^2 \right\rangle - \left\langle \mathrm{Tr}\, M_{ud}^{-1} \right\rangle^2 \right), \tag{6.3}$$

where the factor of 1/4 is present - again - due to staggered rooting. This is essentially the variance of $\mathrm{Tr}\, M_{ud}^{-1}$ in the lattice QCD language. The disconnected susceptibility can also be defined as a cross-derivative:

$$\chi_{\mathrm{disc}} = \frac{T}{V}\left(\frac{\partial^2}{\partial m_u \partial m_d} \log Z \right)_{m_u = m_d}, \tag{6.4}$$

thus, it is a legitimate physical observable. We study both the full and disconnected susceptibilities, because they may be sensitive in different ways to the distinct critical points present in the 3 dimensional QCD phase diagram spanned by the variables T, μ_B^2 and m_{ud}. The condensate and the susceptibilities contain both multiplicative and additive UV divergences. One possible definition of UV finite condensate and susceptibility is given by the following renormalization

$$\langle \bar{\psi}\psi \rangle^R = \frac{m_{ud}}{f_\pi^4}\left[\langle \bar{\psi}\psi \rangle_{T=0} - \langle \bar{\psi}\psi \rangle_T \right], \tag{6.5}$$

$$\chi^R = \frac{m_{ud}^2}{f_\pi^4}\left[\chi_{T=0} - \chi_T \right], \tag{6.6}$$

$$\chi^R_{\mathrm{disc}} = \frac{m_{ud}^2}{f_\pi^4}\left[\chi_{\mathrm{disc,T=0}} - \chi_{\mathrm{disc,T}} \right], \tag{6.7}$$

where the division by f_π^4 is there to ensure the quantities $\langle \bar{\psi}\psi \rangle^R, \chi^R$ and χ^R_{disc} are dimensionless. The chiral condensate should vanish in the high temperature region due to the (approximate) restoration of chiral symmetry. Defining the renormalized condensate according to Eq. (6.5) leads to the opposite behavior.

The peak position of either the full or disconnected susceptibilities can be used to define the chiral crossover temperature. Similarly, the maximal value of either of these susceptibilities can be used to study the strength of the crossover transition, as they both diverge in the presence of true critical behavior. In the left panel of Fig. 6.1 the renormalized chiral condensate as a function of the temperatures is presented. The right panel shows the full and disconnected chiral susceptibility, where the latter takes on smaller values compared to the full susceptibility in the transition region at fixed volume.

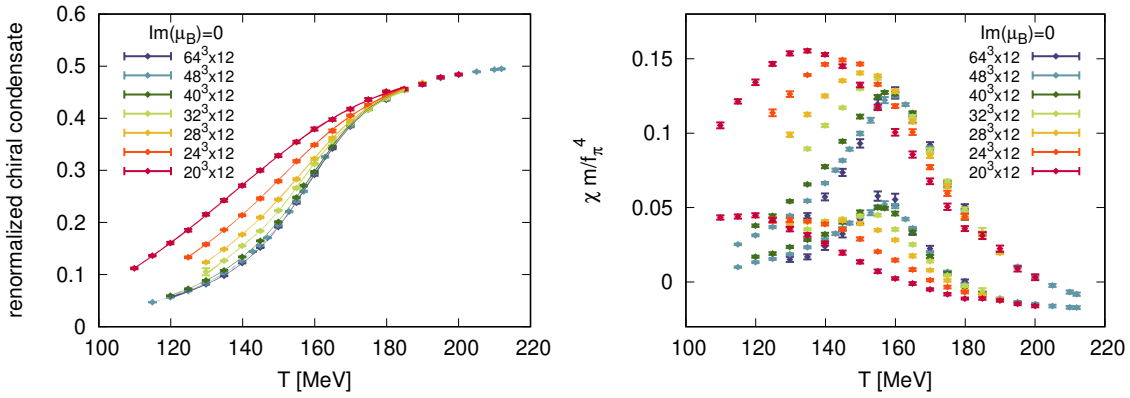

Figure 6.1: Left panel: The renormalized chiral condensate as a function of temperature for different spatial volumes. Right panel: The renormalized full and disconnected chiral susceptibility as a function of temperature for different spatial volumes. The full susceptibility is always higher compared to the disconnected one at fixed volume in the transition region.

6.3 Deconfinement observables

As discussed in Section 2.3 the Polyakov loop can be used to probe the spontaneous breaking of the center symmetry. Its expectation value is related to the quark free energy F_Q and hence sensitive to deconfinement. We can define the free energy and the static quark entropy S_Q according to [39]

$$F_Q = -T \log \left(\frac{1}{V} \sum_{\vec{x}} | \langle P(\vec{x}) \rangle_T | \right) + T_0 \log \left(\frac{1}{V} \sum_{\vec{x}} | \langle P(\vec{x}) \rangle_{T_0} | \right), \tag{6.8}$$

$$S_Q = -\frac{\partial F_Q}{\partial T}. \tag{6.9}$$

T_0 is a reference temperature, and the second term in the definition of F_Q is needed to remove

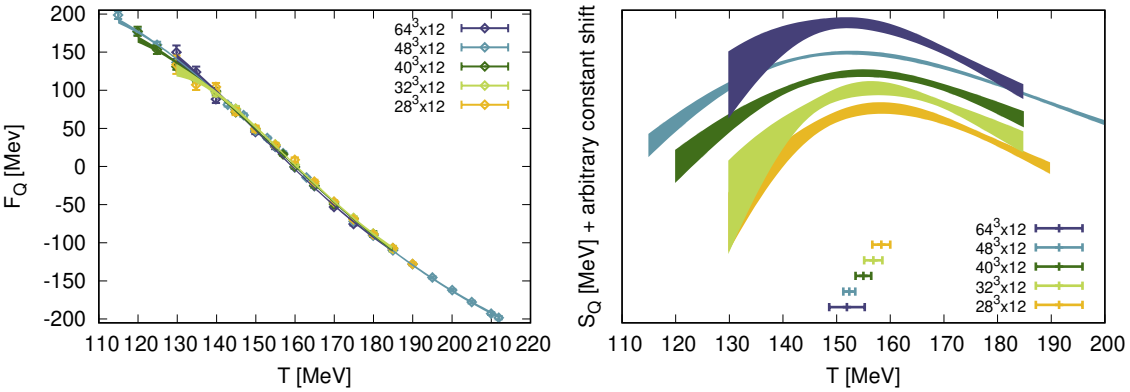

Figure 6.2: Left panel: The static quark free energy as a function of temperature for different spatial volumes. Right panel: The static quark entropy as a function of temperature for different spatial volumes. In order for the curves not to overlap, they were shifted by arbitrary amounts in the vertical direction. The horizontal datapoints located on the bottom show the associated transition temperature. Both panels show results at $\mu = 0$.

the additive divergence in the free energy. The value of the reference temperature T_0, together with Eq. (6.8) defines a renormalization scheme for the static quark free energy. In practice, we interpolate F_Q in β provided by $32^3 \times 8$, $40^3 \times 10$, $48^3 \times 12$, $64^3 \times 16$ and $80^3 \times 20$ at fixed T_0. The entropy S_Q is estimated by interpolating the lattice results for $F_Q(T)$ and differentiating the interpolating function. For the interpolation we use a second order-by second order rational function fit. For pure gauge theory, where a true first order deconfinement phase transition is present, the static quark free energy is infinite in the confined phase (i.e. the Polyakov loop is zero). For full QCD, this is no longer the case. Nevertheless, one can use the peak of $S_Q(T)$ (the inflection point of $F_Q(T)$) to define a crossover temperature. In Fig. 6.2 we show results for F_Q and S_Q for several different volumes.

6.4 Vanishing chemical potential

The key feature of a crossover transition is basically no or a very mild volume dependence of the observables and hence the absence of discontinuities or divergences up to the infinite volume limit. In the opposite direction, i.e. decreasing the volume, the behavior is not so clear.

6.4.1 Chiral condensate

Chiral perturbation theory (chiral PT) predicts an exponential dependence of the chiral condensate as a function of the spatial extension N_x. The leading asymptotic behavior of the condensate at $T = 0$ takes on the form [229]

$$\langle \bar{\psi}\psi \rangle \sim \frac{\sqrt{m_\pi}}{F_\pi^2} \frac{e^{-m_\pi N_x}}{(2\pi N_x)^{3/2}}. \tag{6.10}$$

In Fig. 6.3 we fit this prediction to the chiral condensate values which are obtained via a spline interpolation at fixed $T = 140$ MeV for all lattices. The blue curve is the fit function

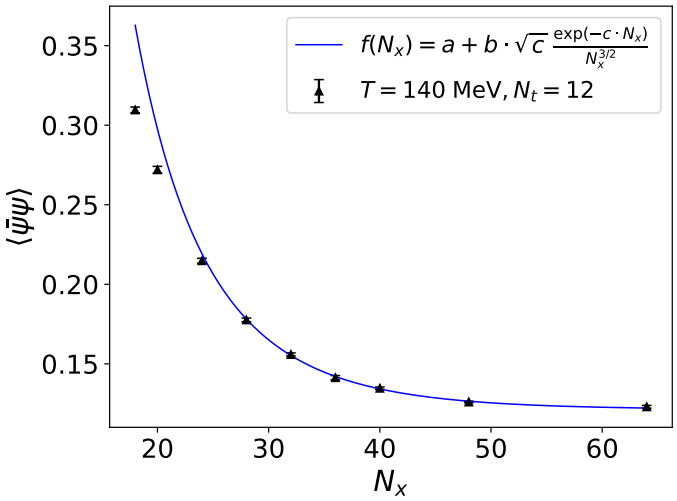

Figure 6.3: Chiral condensate at a fixed temperature $T = 140$ MeV for every lattice with $N_t = 12$ as a function of the spatial extension N_x. The blue curve is a fit inspired by chiral PT Eq. (6.10) in the range of $N_x \in [28, 64]$.

$f(N_x)$ as shown in the legend and provides $\chi^2/\text{ndof} = 1.03$. The coefficient c is m_π according to Eq. (6.10) and reads $c = 131 \pm 10$ MeV. This remarkable agreement with the pion mass is only true for $N_x \geq 28$. One reason for this lies in the fact that the transition temperature for $18^3 \times 12$ and $20^3 \times 12$ is below $T = 140$ MeV as shown in Fig. 6.5 on the lower left panel. Hence the system tends to be deconfined and cannot be described by chiral PT Eq. (6.10).

6.4.2 The transition temperature T_c defined by χ_{full}

An analytic crossover transition does not provide a unique transition temperature. Instead, different observables might lead to different results depending on their exact definition (see [230] for a detailed discussion). To investigate the volume dependence of the transition temperature, we restrict the following analysis on T_c defined by the peak of the full chiral susceptibility. The full chiral susceptibility is expressed as a function of the chiral condensate. The advantage is that $\chi(\langle\bar{\psi}\psi\rangle)$ has a simpler form compared to $\chi(T)$ and can be fitted more precisely with a low order polynomial. Together with the corresponding $\langle\bar{\psi}\psi\rangle_c$ for which χ takes on its maximum value, the transition temperature can be read off from $\langle\bar{\psi}\psi\rangle(T)$ via spline interpolation. This procedure allows us to calculate precisely the proxy δT for the width of the transition defined as

$$\delta T = \langle\bar{\psi}\psi\rangle^{-1}\left(\langle\bar{\psi}\psi\rangle_c + \frac{\Delta\langle\bar{\psi}\psi\rangle}{2}\right) - \langle\bar{\psi}\psi\rangle^{-1}\left(\langle\bar{\psi}\psi\rangle_c - \frac{\Delta\langle\bar{\psi}\psi\rangle}{2}\right), \tag{6.11}$$

$$\Delta\langle\bar{\psi}\psi\rangle = \sqrt{-\chi_{\max}\left(\frac{\mathrm{d}^2\chi}{\mathrm{d}\langle\bar{\psi}\psi\rangle^2}\bigg|_{\langle\bar{\psi}\psi\rangle_c}\right)^{-1}}. \tag{6.12}$$

More details can be found in [33] and my Master thesis [126]. For a broad range of aspect

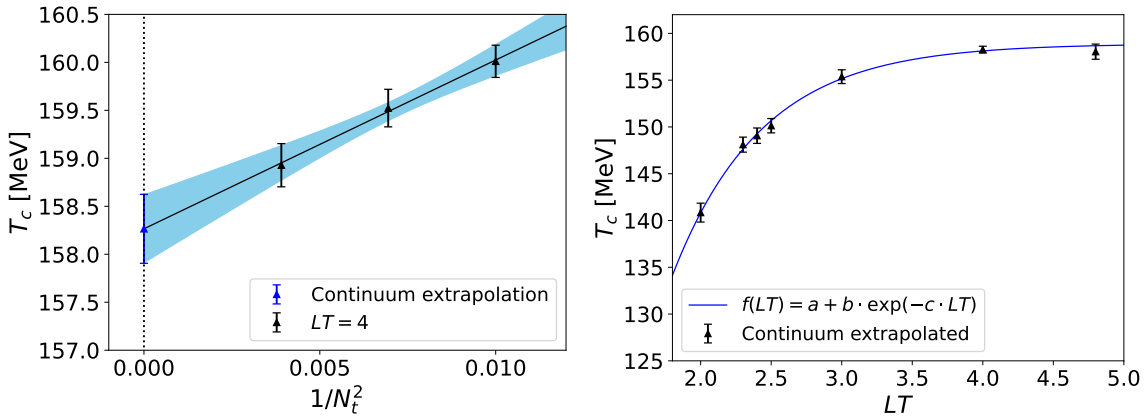

Figure 6.4: Left: Exemplary continuum extrapolation of T_c at aspect ratio $LT = 4$. Right: Continuum extrapolated T_c as a function of the aspect ratio LT and additional infinite volume extrapolation via an exponential fit.

ratios we can now perform a continuum extrapolation as exemplary demonstrated on the left panel of Fig. 6.4. The continuum extrapolated results of the transition temperature for each aspect ratio are shown on the right panel. Again, we observe an exponential dependence which allows us to obtain the infinite volume limit of the continuum extrapolated transition temperatures

$$T_c(N_t \to \infty, LT \to \infty) = 158.9 \pm 0.6 \text{ MeV}. \tag{6.13}$$

The error is purely statistical whereby two different polynomial fits of order 3,4 for the peak determination are used and combined. The exponential dependence on the volume is not limited to T_c. As demonstrated in Fig. 6.5, the peak of the full susceptibility $\chi_{\max}$ and the width of the transition δT Eq. (6.11) indicate a similar behavior. The lower left and lower right panel show T_c as function of N_x and the box size L respectively. The box size can be obtained by

$$L = N_x \cdot a = \frac{N_x}{N_t \cdot T_c}, \tag{6.14}$$

and multiplied with the appropriate factor to get a result in fm. The idea is to keep the box size constant and to vary the lattice geometry at fixed temporal extension.

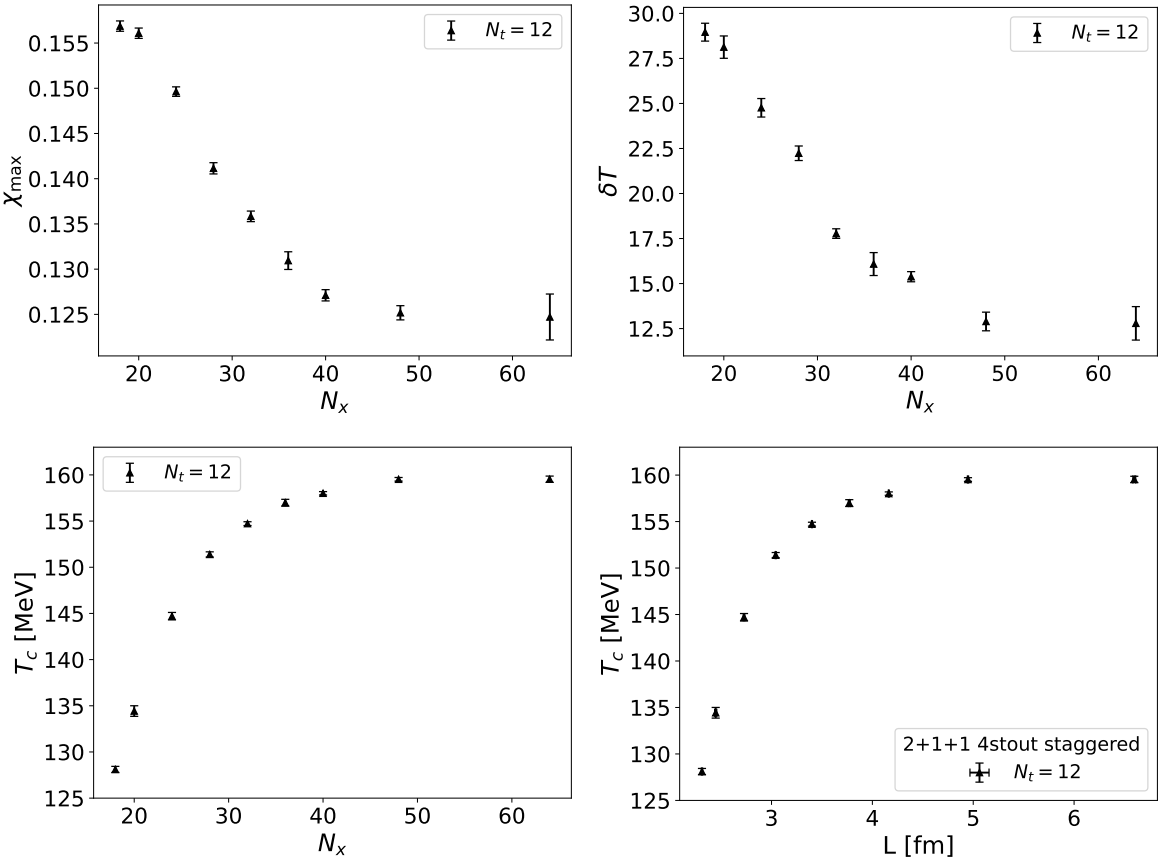

Figure 6.5: Volume dependence of $\chi_{\max}$ (upper left), δT (upper right) and T_c (lower left) as functions of N_x. The lattice geometry is converted in the box size L in fm (lower right).

The peak of the susceptibility (upper left panel) decreases and stays nearly constant if $N_x \gtrapprox 40$ ($LT \gtrapprox 3.3$) which is a clear sign of a crossover. It confirms the common standard to use $LT = 4$ in QCD thermodynamics to be close to the infinite volume limit. In the opposite direction, the peak increases significantly as the volume is further decreased.

6.4.3 Crossover temperatures defined by different observables

We are now in a position to compare the deconfinement and chiral symmetry related definitions of the crossover temperature. We show the different values of T_c defined as the peak of $\chi^R(T)$, the peak of $\chi^R_{disc}(T)$ as well as the peak of $S_Q(T)$ in Fig. 6.6. For comparison, we also

show curves where the chiral condensate or the static quark free energy are constant, with the constant chosen to be the infinite volume value at the crossover temperature defined via the full chiral susceptibility.

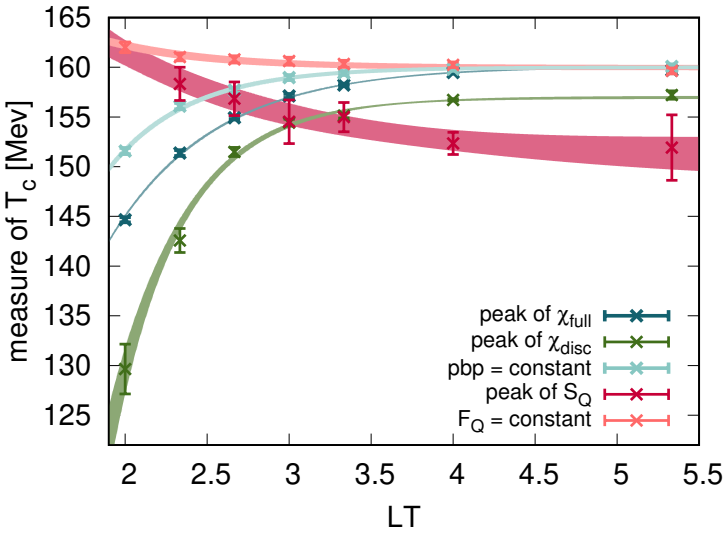

Figure 6.6: Five different definitions of the transition temperature as functions of the simulation volume, labeled by the aspect ratio $LT = N_x/N_t$. The purple and cyan points refer to the peak position of the full and disconnected chiral susceptibility, respectively. In addition, we show the temperature where the chiral condensate is constant (blue). In all cases, the infinite volume value is approached from below. The two other measures of T_c come from the Polyakov loop, either keeping a constant value for F_Q (pink), or determining the maximum of the static quark entropy S_Q (purple). In these both cases, the infinite volume limit is approached from above. The fixed values of the chiral condensate and F_Q have been set such that these match the infinite volume limit at the maximum of the full chiral susceptibility.

Fig. 6.6 establishes an ordering of the different crossover temperatures in the infinite volume limit:

$$T_c^{(S_Q)} < T_c^{(\chi^R_{disc})} < T_c^{\chi^R}. \tag{6.15}$$

The differences between the definitions are small, amounting only to a few MeV. The identification of such an ordering had never been possible in existing literature, due to larger error bars. Furthermore, we see a different volume dependence of the different crossover temperatures. Namely, the two chiral definitions lead to a T_c that is monotonically increasing with the physical volume, while the deconfinement definition leads to a T_c that is monotonically decreasing with the volume. This means that at small enough volumes, the ordering changes, and the definition of T_c based on the static quark entropy becomes the largest. We also note that finite volume effects on the deconfinement based definition of T_c appear to be smaller. Even on the smallest lattice, with aspect ratio $LT = 2$, the deconfinement based definition gives a result of around 160 MeV, which is quite close to the infinite volume value, and is much larger than the chiral symmetry based definitions.

6.5 Imaginary chemical potential

Our extrapolation method to real μ_B is based on the observation of an approximate data collapse [33]. The chiral susceptibility as a function of the chiral condensate is a curve that is almost independent of the imaginary chemical potential. In [33] we demonstrated this for the full susceptibility. Here, we show it both for χ_{full} and χ_{disc} in Fig. 6.7 where both susceptibilities are shown as functions of the condensate for several imaginary chemical potentials, for two different volumes.

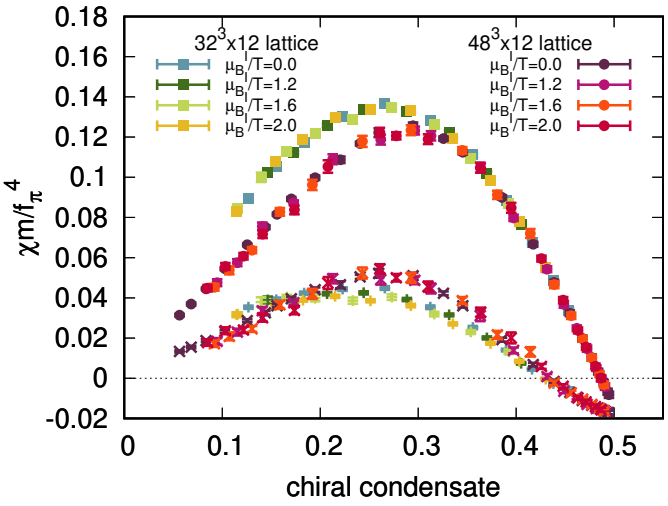

Figure 6.7: The full (filled symbols) and disconnected (crosses) chiral susceptibilities as a function of the condensate for two different volumes and several values of the imaginary chemical potential.

The collapse curves for both susceptibilities are approximately independent of the imaginary chemical potential, they significantly depend on the volume. Similarly to the procedure described in Section 6.4.2, the analysis steps are:

1. Determine the renormalized (full or disconnected) susceptibility as a function of the condensate for several values of the imaginary baryochemical potential.

2. Find the peak position in the susceptibility as a function of the condensate for each value of $\mathrm{Im}\,\mu_B/T$ with a low order polynomial fit.

3. Use an interpolation of the condensate as a function of T to convert the peak position from the condensate value to the temperature for each $\mathrm{Im}\,\mu_B/T$.

4. Perform a fit of $T_c(\mathrm{Im}\,\mu_B/T_c)$, and use the fit to extrapolate the crossover temperature from $\mu_B^2 \leq 0$ to $\mu_B^2 > 0$.

If instead of the chiral condensate, one attempts to show the chiral suscpetibility as a function of the static quark free energy F_Q, the collapse is less accurate. This is shown in Fig. 6.8, where the left panel shows χ_{full} as a function of F_Q for several imaginary chemical potentials on our $48^3 \times 12$ lattices. For the calculation of the crossover temperature defined with S_Q, we simply use the same rational function fit of $F_Q(T)$ that we used for the $\mu_B = 0$ case. The

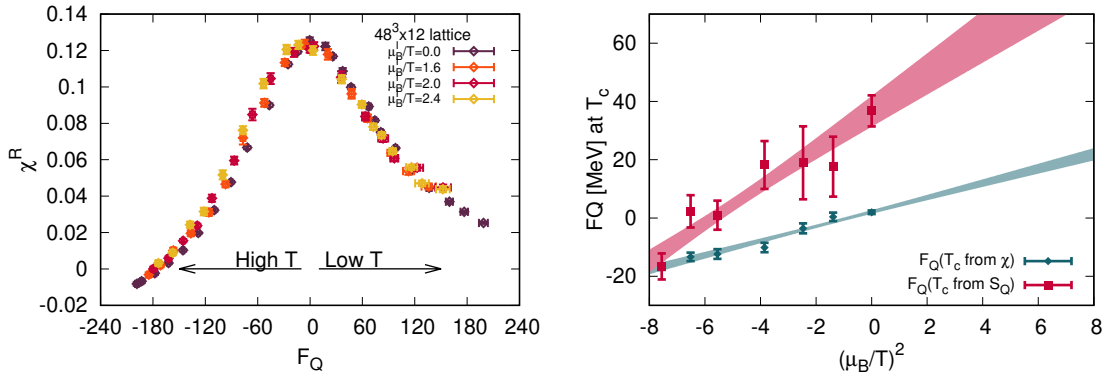

Figure 6.8: Left: The full chiral susceptibility as a function of the static quark free energy. Right: The value of F_Q at the chiral crossover temperature (defined via the peak of the full chiral susceptibility or the static quark entropy) as a function of $\hat{\mu}_B^2$.

right panel shows the value of $F_Q(T_c)$ right at the transition temperature which is defined by either χ_{full} or S_Q as a function of $\hat{\mu}_B^2$. The bands indicate linear extrapolations in $\hat{\mu}_B^2$.

6.6 Phase diagram at finite and real density

Now let us turn to the volume dependence of the phase diagram. We show the crossover temperature, defined via the peak position of the full and disconnected chiral condensates, as well as the static quark entropy as a function of μ_B^2/T^2 in the left panel of Fig. 6.9 in a fixed volume, on our $48^3 \times 12$ lattices. We see that not only $T_c(\mu_B = 0)$, but also the chemical potential dependence is different for the different definitions. At larger imaginary chemical potentials, the three definitions come closer to each other, which might be due to the presence of the Roberge-Weiss critical endpoint. In the near vicinity of such a critical

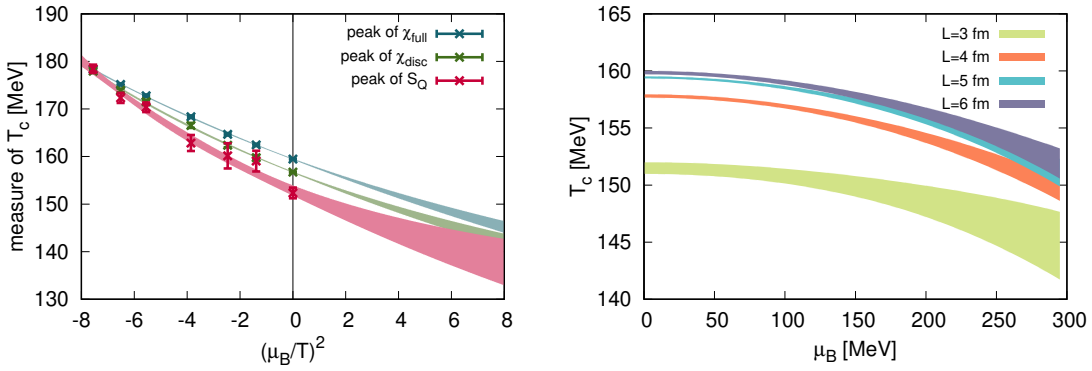

Figure 6.9: Left: Extrapolation of the crossover temperature as a function of μ_B^2/T^2 using the three different definitions discussed in the main text on our $48^3 \times 12$ lattices. Right: Crossover temperature defined via the peak of χ_{full} for different lattice volumes, fixed in fm.

point, the crossover transition should get narrower, and we thus expect different definitions of the crossover temperature to converge towards each other. This is exactly what we observe.

Here, we note that in the strangeness neutral setting employed in the present paper, the Roberge-Weiss transition is not located at $\mathrm{Im}\,\mu_B/T = \pi$, but at a slightly larger value [231].

6.7 Strength of the crossover at finite density

A very interesting question, with more phenomenological implications, is whether the crossover line turns into a line of first order transitions at a critical endpoint at some real value of the baryochemical potential μ_B. If it does, it is expected that the crossover transition becomes narrower and stronger at larger μ_B, at least in the vicinity of the critical endpoint. Here, we discuss some measures of the width or strength of the transition as functions of μ_B for small chemical potentials. In Fig. 6.10 we present the values of S_Q, χ^R and χ^R_{disc} at the crossover temperature as functions of μ_B^2/T^2, for two different physical volumes, where the bands show linear extrapolations in μ_B^2/T^2. All three quantities should diverge at the crit-

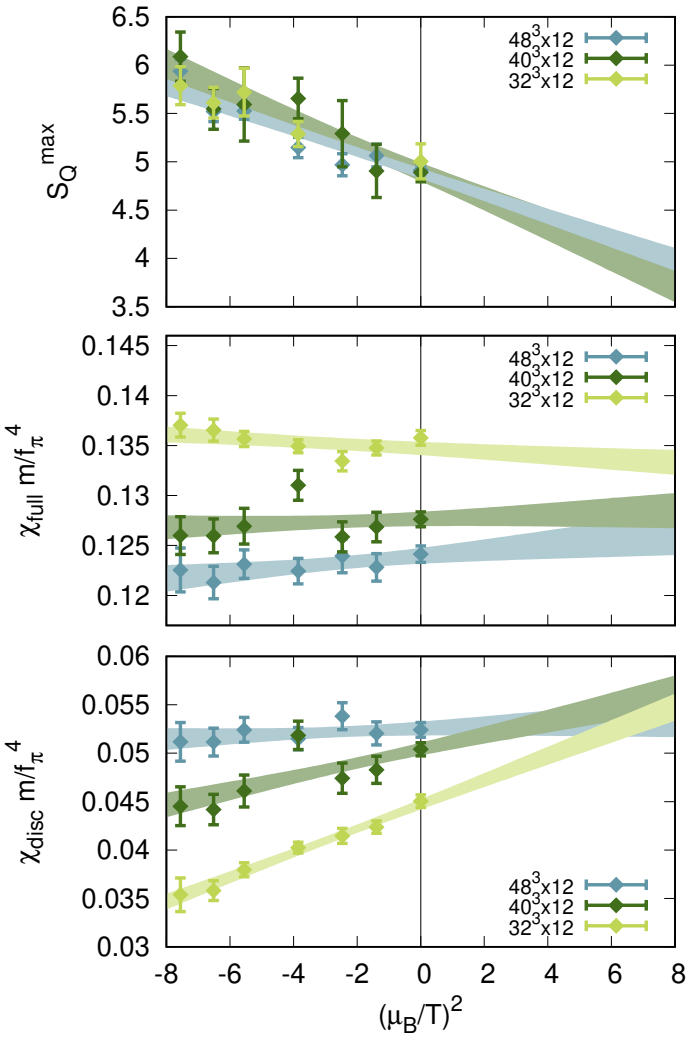

Figure 6.10: Extrapolation of the maximal value of χ^R, χ^R_{disc} and S_Q together with linear extrapolations in μ_B^2 for three different volumes.

ical endpoint in the infinite volume limit. Thus, with increasing volume, one expects these

quantities to grow in the vicinity of the critical endpoint. The only one of these quantities showing a rise at larger μ_B^2 is χ^R_{disc}, while χ^R remains approximately constant up to our largest volume, and S_Q decreases with increasing μ_B^2. From the behavior of χ^R_{disc} alone, one might be tempted to conclude that the crossover transition gets stronger at larger μ_B, which would be a signal of the coveted critical endpoint. However, the lack of a similar behavior in the other two quantities - S_Q and χ^R makes the interpretation of the physical picture uncertain. Furthermore, we once again see that the deconfinement related quantity (S_Q) has milder finite volume effects than the quantities related to chiral symmetry restoration (χ^R and χ^R_{disc}). The disconnected susceptibility shows an interesting behavior: an increasing trend with increasing μ_B^2, especially for the two lower volumes. If the expected QCD critical endpoint exists, such a behavior could be due to the critical region shrinking with increasing physical volume (E.g. a smaller volume is more tolerant to the mistuning of the parameters of a system, and criticality can be observable from farther away.). Due to the lack of such a signal in χ^R and S_Q, we would be cautious about making such an interpretation, but the behavior of χ^R_{disc} certainly is suggestive and warrants further investigation.

7 Outlook

Exploring QCD under extreme conditions is not just an academic pleasure for particle physicists. It provides us key insights to the evolution and structure of the cosmos; from the properties of deconfined matter to the potential emergence of exotic phases like color superconductivity in neutron stars. Therefore, mapping the phases of strongly interacting matter is essential for enhancing our understanding of the universe and bridges the smallest scales of quarks and gluons to cosmic phenomena.

One essential result presented in this thesis is the EoS from first principles up to $\hat{\mu}_B \leq 3.5$ covering the chemical potential range of the current colliders LHC and RHIC. It enables hydrodynamic simulations at small and vanishing strangeness for the temperatures 130 MeV $\leq T \leq$ 280 MeV. The new-generation facilities like FAIR or NICA explore further regions of the QCD phase diagram and demand theoretical predictions at higher chemical potentials. Moreover, gravitational wave astronomy offers a new possibility to study the EoS through the mergers of neutron stars at even higher densities. A serious challenge for lattice QCD research lies in providing accurate results under such conditions, where direct simulations at finite density are hindered by the sign problem resulting from the complex action. Recently, the authors of [232] showed that the rooting procedure of the complex quark determinant at finite μ_B in the staggered fermion formalism can cause unphysical lattice artifacts. Minimally doubled fermions, such as Karsten-Wilczek quarks [233, 234], provide a promising alternative. These formulations include a rooting-free quark determinant for degenerate flavors and preserve a remnant of chiral symmetry. Various improvement strategies, especially with focus on renormalization, are still under investigation [235, 236].

QCD under extreme conditions can exhibit critical behavior as demonstrated in lattice simulations for high magnetic fields [237] or observed for nuclear matter in the case of the nuclear liquid-gas transition (recall Section 2.6). Simulations in the vicinity of real phase transitions face the problem of (super-)critical slowing down, causing high computational costs. We could demonstrate the effective application of parallel tempering to mitigate supercritical slowing down in a pure gauge theory, achieving the first per-mill accurate result in lattice QCD thermodynamics for the transition temperature. Furthermore, we applied this technique to dynamic simulations to determine the critical quark masses in a three flavor theory. Continuum extrapolated results are still missing but remain desirable, possibly requiring innovative algorithmic strategies beyond the traditional HMC algorithm.

Exploring QCD in the parameter space of temperature, mass, chemical potential or magnetic field can potentially enable the extrapolation of critical surfaces to conditions which are relevant for heavy-ion collisions or neutron star mergers. Form the lattice perspective, increasing the statistics with the extrapolation techniques at hand is probably not sufficient

to disclose the secret of the existence of a critical endpoint in the T-μ_B plane. To summarize: One of the primary goals for the lattice QCD community is and remains mitigating the sign problem to obtain reliable results at finite density.

Bibliography

[1] E. W. Kolb and M. S. Turner, *The Early Universe*, vol. 69. 1990.

[2] S. Weinberg, "A Model of Leptons," *Phys. Rev. Lett.*, vol. 19, pp. 1264–1266, 1967.

[3] A. Salam, "Weak and Electromagnetic Interactions," *Conf. Proc. C*, vol. 680519, pp. 367–377, 1968.

[4] S. L. Glashow, "Partial Symmetries of Weak Interactions," *Nucl. Phys.*, vol. 22, pp. 579–588, 1961.

[5] F. Csikor, Z. Fodor, and J. Heitger, "Endpoint of the hot electroweak phase transition," *Phys. Rev. Lett.*, vol. 82, pp. 21–24, 1999.

[6] M. D'Onofrio, K. Rummukainen, and A. Tranberg, "Sphaleron Rate in the Minimal Standard Model," *Phys. Rev. Lett.*, vol. 113, no. 14, p. 141602, 2014.

[7] F. Englert and R. Brout, "Broken Symmetry and the Mass of Gauge Vector Mesons," *Phys. Rev. Lett.*, vol. 13, pp. 321–323, 1964.

[8] P. W. Higgs, "Broken Symmetries and the Masses of Gauge Bosons," *Phys. Rev. Lett.*, vol. 13, pp. 508–509, 1964.

[9] G. S. Guralnik, C. R. Hagen, and T. W. B. Kibble, "Global Conservation Laws and Massless Particles," *Phys. Rev. Lett.*, vol. 13, pp. 585–587, 1964.

[10] D. J. Gross and F. Wilczek, "Ultraviolet Behavior of Nonabelian Gauge Theories," *Phys. Rev. Lett.*, vol. 30, pp. 1343–1346, 1973.

[11] H. D. Politzer, "Reliable Perturbative Results for Strong Interactions?," *Phys. Rev. Lett.*, vol. 30, pp. 1346–1349, 1973.

[12] Y. Aoki, G. Endrodi, Z. Fodor, S. D. Katz, and K. K. Szabo, "The Order of the quantum chromodynamics transition predicted by the standard model of particle physics," *Nature*, vol. 443, pp. 675–678, 2006.

[13] D. Schwarz, "The first second of the universe," *Annalen Phys.*, vol. 12, pp. 220–270, 2003.

[14] E. Annala, T. Gorda, A. Kurkela, J. Nättilä, and A. Vuorinen, "Evidence for quark-matter cores in massive neutron stars," *Nature Phys.*, vol. 16, no. 9, pp. 907–910, 2020.

[15] B. P. Abbott *et al.*, "GW170817: Observation of Gravitational Waves from a Binary Neutron Star Inspiral," *Phys. Rev. Lett.*, vol. 119, no. 16, p. 161101, 2017.

[16] U. W. Heinz and M. Jacob, "Evidence for a new state of matter: An Assessment of the results from the CERN lead beam program," 1 2000.

[17] I. Arsene *et al.*, "Quark gluon plasma and color glass condensate at RHIC? The Perspective from the BRAHMS experiment," *Nucl. Phys. A*, vol. 757, pp. 1–27, 2005.

[18] K. G. Wilson and M. E. Fisher, "Critical exponents in 3.99 dimensions," *Phys. Rev. Lett.*, vol. 28, pp. 240–243, 1972.

[19] K. G. Wilson and J. B. Kogut, "The Renormalization group and the epsilon expansion," *Phys. Rept.*, vol. 12, pp. 75–199, 1974.

[20] K. G. Wilson, "The Renormalization Group: Critical Phenomena and the Kondo Problem," *Rev. Mod. Phys.*, vol. 47, p. 773, 1975.

[21] A. Pelissetto and E. Vicari, "Critical phenomena and renormalization group theory," *Phys. Rept.*, vol. 368, pp. 549–727, 2002.

[22] G. 't Hooft and M. J. G. Veltman, "Regularization and Renormalization of Gauge Fields," *Nucl. Phys. B*, vol. 44, pp. 189–213, 1972.

[23] H. Yukawa, "On the Interaction of Elementary Particles I," *Proc. Phys. Math. Soc. Jap.*, vol. 17, pp. 48–57, 1935.

[24] M. Gell-Mann, "A Schematic Model of Baryons and Mesons," *Phys. Lett.*, vol. 8, pp. 214–215, 1964.

[25] M. E. Peskin and D. V. Schroeder, *An Introduction to quantum field theory*. Reading, USA: Addison-Wesley, 1995.

[26] S. Weinberg, *The quantum theory of fields. Vol. 2: Modern applications*. Cambridge University Press, 8 2013.

[27] T.-P. Cheng and L.-F. Li, *Gauge Theory of Elementary Particle Physics*. Oxford, UK: Oxford University Press, 1984.

[28] L. H. Ryder, *Quantum Field Theory*. Cambridge University Press, 6 1996.

[29] A. Deur, S. J. Brodsky, and G. F. de Teramond, "The QCD Running Coupling," *Nucl. Phys.*, vol. 90, p. 1, 2016.

[30] M. Tanabashi *et al.*, "Review of Particle Physics," *Phys. Rev. D*, vol. 98, no. 3, p. 030001, 2018.

[31] K. G. Wilson, "Confinement of Quarks," *Phys. Rev. D*, vol. 10, pp. 2445–2459, 1974.

[32] R. Hagedorn, "Statistical thermodynamics of strong interactions at high-energies," *Nuovo Cim. Suppl.*, vol. 3, pp. 147–186, 1965.

[33] S. Borsanyi, Z. Fodor, J. N. Guenther, R. Kara, S. D. Katz, P. Parotto, A. Pasztor, C. Ratti, and K. K. Szabo, "QCD Crossover at Finite Chemical Potential from Lattice Simulations," *Phys. Rev. Lett.*, vol. 125, no. 5, p. 052001, 2020.

[34] A. Andronic, P. Braun-Munzinger, K. Redlich, and J. Stachel, "Decoding the phase structure of QCD via particle production at high energy," *Nature*, vol. 561, no. 7723, pp. 321–330, 2018.

[35] G. 't Hooft, "A Property of Electric and Magnetic Flux in Nonabelian Gauge Theories," *Nucl. Phys. B*, vol. 153, pp. 141–160, 1979.

[36] G. 't Hooft, "On the Phase Transition Towards Permanent Quark Confinement," *Nucl. Phys. B*, vol. 138, pp. 1–25, 1978.

[37] C. Ratti and R. Bellwied, *The Deconfinement Transition of QCD: Theory Meets Experiment*, vol. 981 of *Lecture Notes in Physics*. 6 2021.

[38] C. Gattringer and C. Lang, "Quantum chromodynamics on the lattice," *Lect. Notes Phys.*, vol. 788, pp. 1–343, 2010.

[39] L. D. McLerran and B. Svetitsky, "Quark Liberation at High Temperature: A Monte Carlo Study of SU(2) Gauge Theory," *Phys. Rev. D*, vol. 24, p. 450, 1981.

[40] S. Borsanyi, K. R., Z. Fodor, D. A. Godzieba, P. Parotto, and D. Sexty, "Precision study of the continuum SU(3) Yang-Mills theory: How to use parallel tempering to improve on supercritical slowing down for first order phase transitions," *Phys. Rev. D*, vol. 105, no. 7, p. 074513, 2022.

[41] C. S. Wu, E. Ambler, R. W. Hayward, D. D. Hoppes, and R. P. Hudson, "Experimental Test of Parity Conservation in β Decay," *Phys. Rev.*, vol. 105, pp. 1413–1414, 1957.

[42] A. Bzdak, S. Esumi, V. Koch, J. Liao, M. Stephanov, and N. Xu, "Mapping the Phases of Quantum Chromodynamics with Beam Energy Scan," *Phys. Rept.*, vol. 853, pp. 1–87, 2020.

[43] M. Gell-Mann, "The Eightfold Way: A Theory of strong interaction symmetry," 3 1961.

[44] Y. Ne'eman, "Derivation of strong interactions from a gauge invariance," *Nucl. Phys.*, vol. 26, pp. 222–229, 1961.

[45] C. Vafa and E. Witten, "Restrictions on Symmetry Breaking in Vector-Like Gauge Theories," *Nucl. Phys. B*, vol. 234, pp. 173–188, 1984.

[46] V. Koch, "Aspects of chiral symmetry," *Int. J. Mod. Phys. E*, vol. 6, pp. 203–250, 1997.

[47] M. D. Schwartz, *Quantum Field Theory and the Standard Model*. Cambridge University Press, 3 2014.

[48] M. Gell-Mann, R. J. Oakes, and B. Renner, "Behavior of current divergences under SU(3) x SU(3)," *Phys. Rev.*, vol. 175, pp. 2195–2199, 1968.

[49] S. Weinberg, "Precise relations between the spectra of vector and axial vector mesons," *Phys. Rev. Lett.*, vol. 18, pp. 507–509, 1967.

[50] D. Diakonov, "Instantons at work," *Prog. Part. Nucl. Phys.*, vol. 51, pp. 173–222, 2003.

[51] T. Schäfer and E. V. Shuryak, "Instantons in QCD," *Rev. Mod. Phys.*, vol. 70, pp. 323–426, 1998.

[52] C. G. Callan, Jr., R. F. Dashen, and D. J. Gross, "Toward a Theory of the Strong Interactions," *Phys. Rev. D*, vol. 17, p. 2717, 1978.

[53] S. L. Adler, "Axial vector vertex in spinor electrodynamics," *Phys. Rev.*, vol. 177, pp. 2426–2438, 1969.

[54] J. S. Bell and R. Jackiw, "A PCAC puzzle: $\pi^0 \to \gamma\gamma$ in the σ model," *Nuovo Cim. A*, vol. 60, pp. 47–61, 1969.

[55] M. Veltman, "Theoretical aspects of high energy neutrino interactions," *Proc. R. Soc. Lond.*, vol. 301, 1967.

[56] D. G. Sutherland, "Current algebra and some nonstrong mesonic decays," *Nucl. Phys. B*, vol. 2, pp. 433–440, 1967.

[57] K. Fujikawa, "Path Integral Measure for Gauge Invariant Fermion Theories," *Phys. Rev. Lett.*, vol. 42, pp. 1195–1198, 1979.

[58] B. L. Ioffe, "Axial anomaly in quantum electro- and chromodynamics and the structure of the vacuum in quantum chromodynamics," *Usp. Fiz. Nauk*, vol. 178, p. 647, 2008.

[59] T. Banks and A. Casher, "Chiral Symmetry Breaking in Confining Theories," *Nucl. Phys. B*, vol. 169, pp. 103–125, 1980.

[60] E. Witten, "Current Algebra Theorems for the U(1) Goldstone Boson," *Nucl. Phys. B*, vol. 156, pp. 269–283, 1979.

[61] G. Veneziano, "U(1) Without Instantons," *Nucl. Phys. B*, vol. 159, pp. 213–224, 1979.

[62] R. D. Peccei, "The Strong CP problem and axions," *Lect. Notes Phys.*, vol. 741, pp. 3–17, 2008.

[63] S. Aoki, Y. Aoki, H. Fukaya, S. Hashimoto, C. Rohrhofer, and K. Suzuki, "Role of the axial U(1) anomaly in the chiral susceptibility of QCD at high temperature," *PTEP*, vol. 2022, no. 2, p. 023B05, 2022.

[64] H. T. Ding, S. T. Li, S. Mukherjee, A. Tomiya, X. D. Wang, and Y. Zhang, "Correlated Dirac Eigenvalues and Axial Anomaly in Chiral Symmetric QCD," *Phys. Rev. Lett.*, vol. 126, no. 8, p. 082001, 2021.

[65] F. R. Brown, F. P. Butler, H. Chen, N. H. Christ, Z.-h. Dong, W. Schaffer, L. I. Unger, and A. Vaccarino, "On the existence of a phase transition for QCD with three light quarks," *Phys. Rev. Lett.*, vol. 65, pp. 2491–2494, 1990.

[66] A. M. Polyakov, "Thermal Properties of Gauge Fields and Quark Liberation," *Phys. Lett. B*, vol. 72, pp. 477–480, 1978.

[67] L. Susskind, "Lattice Models of Quark Confinement at High Temperature," *Phys. Rev. D*, vol. 20, pp. 2610–2618, 1979.

[68] B. Svetitsky and L. G. Yaffe, "Critical Behavior at Finite Temperature Confinement Transitions," *Nucl. Phys. B*, vol. 210, pp. 423–447, 1982.

[69] L. G. Yaffe and B. Svetitsky, "First Order Phase Transition in the SU(3) Gauge Theory at Finite Temperature," *Phys. Rev. D*, vol. 26, p. 963, 1982.

[70] J. B. Kogut, M. Stone, H. W. Wyld, W. R. Gibbs, J. Shigemitsu, S. H. Shenker, and D. K. Sinclair, "Deconfinement and Chiral Symmetry Restoration at Finite Temperatures in SU(2) and SU(3) Gauge Theories," *Phys. Rev. Lett.*, vol. 50, p. 393, 1983.

[71] K. Kajantie, C. Montonen, and E. Pietarinen, "Phase Transition of SU(3) Gauge Theory at Finite Temperature," *Z. Phys. C*, vol. 9, p. 253, 1981.

[72] P. Bacilieri *et al.*, "On the Order of the Deconfining Phase Transition in Pure Gauge QCD," *Phys. Rev. Lett.*, vol. 61, pp. 1545–1548, 1988.

[73] A. Ukawa, "QCD PHASE TRANSITIONS AT FINITE TEMPERATURES," *Nucl. Phys. B Proc. Suppl.*, vol. 17, pp. 118–136, 1990.

[74] G. Boyd, J. Engels, F. Karsch, E. Laermann, C. Legeland, M. Lutgemeier, and B. Petersson, "Thermodynamics of SU(3) lattice gauge theory," *Nucl. Phys. B*, vol. 469, pp. 419–444, 1996.

[75] M. Shirogane, S. Ejiri, R. Iwami, K. Kanaya, M. Kitazawa, H. Suzuki, Y. Taniguchi, and T. Umeda, "Latent heat and pressure gap at the first-order deconfining phase transition of SU(3) Yang-Mills theory using the small flow-time expansion method," *PTEP*, vol. 2021, no. 1, p. 013B08, 2021.

[76] M. Shirogane, S. Ejiri, R. Iwami, K. Kanaya, and M. Kitazawa, "Latent heat at the first order phase transition point of SU(3) gauge theory," *Phys. Rev. D*, vol. 94, no. 1, p. 014506, 2016.

[77] B. Lucini, M. Teper, and U. Wenger, "Properties of the deconfining phase transition in SU(N) gauge theories," *JHEP*, vol. 02, p. 033, 2005.

[78] S. Gavin, A. Gocksch, and R. D. Pisarski, "QCD and the chiral critical point," *Phys. Rev. D*, vol. 49, pp. R3079–R3082, 1994.

[79] F. Karsch and S. Stickan, "The Three-dimensional, three state Potts model in an external field," *Phys. Lett. B*, vol. 488, pp. 319–325, 2000.

[80] K. Kashiwa, R. D. Pisarski, and V. V. Skokov, "Critical endpoint for deconfinement in matrix and other effective models," *Phys. Rev. D*, vol. 85, p. 114029, 2012.

[81] C. S. Fischer, J. Luecker, and J. M. Pawlowski, "Phase structure of QCD for heavy quarks," *Phys. Rev. D*, vol. 91, no. 1, p. 014024, 2015.

[82] S. Ejiri, S. Itagaki, R. Iwami, K. Kanaya, M. Kitazawa, A. Kiyohara, M. Shirogane, and T. Umeda, "End point of the first-order phase transition of QCD in the heavy quark region by reweighting from quenched QCD," *Phys. Rev. D*, vol. 101, no. 5, p. 054505, 2020.

[83] A. Kiyohara, M. Kitazawa, S. Ejiri, and K. Kanaya, "Finite-size scaling around the critical point in the heavy quark region of QCD," *Phys. Rev. D*, vol. 104, no. 11, p. 114509, 2021.

[84] F. Cuteri, O. Philipsen, A. Schön, and A. Sciarra, "Deconfinement critical point of lattice QCD with N_f=2 Wilson fermions," *Phys. Rev. D*, vol. 103, no. 1, p. 014513, 2021.

[85] S. Borsanyi, Z. Fodor, J. N. Guenther, R. Kara, P. Parotto, A. Pasztor, and D. Sexty, "The upper right corner of the Columbia plot with staggered fermions," *PoS*, vol. LATTICE2021, p. 496, 2022.

[86] F. Cuteri, O. Philipsen, and A. Sciarra, "On the order of the QCD chiral phase transition for different numbers of quark flavours," *JHEP*, vol. 11, p. 141, 2021.

[87] J. S. Schwinger, "A Theory of the Fundamental Interactions," *Annals Phys.*, vol. 2, pp. 407–434, 1957.

[88] M. Gell-Mann and M. Levy, "The axial vector current in beta decay," *Nuovo Cim.*, vol. 16, p. 705, 1960.

[89] R. D. Pisarski and F. Wilczek, "Remarks on the Chiral Phase Transition in Chromodynamics," *Phys. Rev. D*, vol. 29, pp. 338–341, 1984.

[90] P. Bak, S. Krinsky, and D. Mukamel, "First-Order Transitions, Symmetry, and the epsilon Expansion," *Phys. Rev. Lett.*, vol. 36, pp. 52–55, 1976.

[91] G. Fejos, "Second-order chiral phase transition in three-flavor quantum chromodynamics?," *Phys. Rev. D*, vol. 105, no. 7, p. L071506, 2022.

[92] M. Grahl and D. H. Rischke, "Functional renormalization group study of the two-flavor linear sigma model in the presence of the axial anomaly," *Phys. Rev. D*, vol. 88, no. 5, p. 056014, 2013.

[93] F. Wilczek, "Application of the renormalization group to a second order QCD phase transition," *Int. J. Mod. Phys. A*, vol. 7, pp. 3911–3925, 1992. [Erratum: Int.J.Mod.Phys.A 7, 6951 (1992)].

[94] K. Rajagopal and F. Wilczek, "Static and dynamic critical phenomena at a second order QCD phase transition," *Nucl. Phys. B*, vol. 399, pp. 395–425, 1993.

[95] A. Pelissetto and E. Vicari, "Relevance of the axial anomaly at the finite-temperature chiral transition in QCD," *Phys. Rev. D*, vol. 88, no. 10, p. 105018, 2013.

[96] J. Braun, M. Leonhardt, J. M. Pawlowski, and D. Rosenblüh, "Chiral and effective $U(1)_{\mathrm{A}}$ symmetry restoration in QCD," 12 2020.

[97] O. Philipsen, "Lattice Constraints on the QCD Chiral Phase Transition at Finite Temperature and Baryon Density," *Symmetry*, vol. 13, no. 11, p. 2079, 2021.

[98] F. Karsch, E. Laermann, and C. Schmidt, "The Chiral critical point in three-flavor QCD," *Phys. Lett. B*, vol. 520, pp. 41–49, 2001.

[99] Y. Iwasaki, K. Kanaya, S. Kaya, S. Sakai, and T. Yoshie, "Finite temperature transitions in lattice QCD with Wilson quarks: Chiral transitions and the influence of the strange quark," *Phys. Rev. D*, vol. 54, pp. 7010–7031, 1996.

[100] X.-Y. Jin, Y. Kuramashi, Y. Nakamura, S. Takeda, and A. Ukawa, "Critical endpoint of the finite temperature phase transition for three flavor QCD," *Phys. Rev. D*, vol. 91, no. 1, p. 014508, 2015.

[101] A. Bazavov, H. T. Ding, P. Hegde, F. Karsch, E. Laermann, S. Mukherjee, P. Petreczky, and C. Schmidt, "Chiral phase structure of three flavor QCD at vanishing baryon number density," *Phys. Rev. D*, vol. 95, no. 7, p. 074505, 2017.

[102] C. Bonati, P. de Forcrand, M. D'Elia, O. Philipsen, and F. Sanfilippo, "Chiral phase transition in two-flavor QCD from an imaginary chemical potential," *Phys. Rev. D*, vol. 90, no. 7, p. 074030, 2014.

[103] O. Philipsen and C. Pinke, "The $N_f = 2$ QCD chiral phase transition with Wilson fermions at zero and imaginary chemical potential," *Phys. Rev. D*, vol. 93, no. 11, p. 114507, 2016.

[104] H. T. Ding *et al.*, "Chiral Phase Transition Temperature in (2+1)-Flavor QCD," *Phys. Rev. Lett.*, vol. 123, no. 6, p. 062002, 2019.

[105] F. Cuteri, O. Philipsen, and A. Sciarra, "QCD chiral phase transition from noninteger numbers of flavors," *Phys. Rev. D*, vol. 97, no. 11, p. 114511, 2018.

[106] Y. Kuramashi, Y. Nakamura, H. Ohno, and S. Takeda, "Nature of the phase transition for finite temperature $N_{\rm f} = 3$ QCD with nonperturbatively O(a) improved Wilson fermions at $N_{\rm t} = 12$," *Phys. Rev. D*, vol. 101, no. 5, p. 054509, 2020.

[107] A. Bazavov *et al.*, "Skewness, kurtosis, and the fifth and sixth order cumulants of net baryon-number distributions from lattice QCD confront high-statistics STAR data," *Phys. Rev. D*, vol. 101, no. 7, p. 074502, 2020.

[108] P. Alba, W. Alberico, R. Bellwied, M. Bluhm, V. Mantovani Sarti, M. Nahrgang, and C. Ratti, "Freeze-out conditions from net-proton and net-charge fluctuations at RHIC," *Phys. Lett. B*, vol. 738, pp. 305–310, 2014.

[109] S. Borsanyi, Z. Fodor, S. D. Katz, S. Krieg, C. Ratti, and K. K. Szabo, "Freeze-out parameters: lattice meets experiment," *Phys. Rev. Lett.*, vol. 111, p. 062005, 2013.

[110] P. Braun-Munzinger, J. Stachel, and C. Wetterich, "Chemical freezeout and the QCD phase transition temperature," *Phys. Lett. B*, vol. 596, pp. 61–69, 2004.

[111] A. M. Halasz, A. D. Jackson, R. E. Shrock, M. A. Stephanov, and J. J. M. Verbaarschot, "On the phase diagram of QCD," *Phys. Rev. D*, vol. 58, p. 096007, 1998.

[112] G. Sauer, H. Chandra, and U. Mosel, "Thermal properties of nuclei," *Nucl. Phys. A*, vol. 264, pp. 221–243, 1976.

[113] O. Savchuk, V. Vovchenko, R. V. Poberezhnyuk, M. I. Gorenstein, and H. Stoecker, "Traces of the nuclear liquid-gas phase transition in the analytic properties of hot QCD," *Phys. Rev. C*, vol. 101, no. 3, p. 035205, 2020.

[114] M. Fromm, J. Langelage, S. Lottini, M. Neuman, and O. Philipsen, "Onset Transition to Cold Nuclear Matter from Lattice QCD with Heavy Quarks," *Phys. Rev. Lett.*, vol. 110, no. 12, p. 122001, 2013.

[115] J. Pochodzalla *et al.*, "Probing the nuclear liquid - gas phase transition," *Phys. Rev. Lett.*, vol. 75, pp. 1040–1043, 1995.

[116] V. A. Karnaukhov *et al.*, "Critical temperature for the nuclear liquid gas phase transition," *Phys. Rev. C*, vol. 67, p. 011601, 2003.

[117] J. B. Elliott, P. T. Lake, L. G. Moretto, and L. Phair, "Determination of the coexistence curve, critical temperature, density, and pressure of bulk nuclear matter from fragment emission data," *Phys. Rev. C*, vol. 87, no. 5, p. 054622, 2013.

[118] E. R. Most, L. J. Papenfort, V. Dexheimer, M. Hanauske, S. Schramm, H. Stöcker, and L. Rezzolla, "Signatures of quark-hadron phase transitions in general-relativistic neutron-star mergers," *Phys. Rev. Lett.*, vol. 122, no. 6, p. 061101, 2019.

[119] A. Bauswein, N.-U. F. Bastian, D. B. Blaschke, K. Chatziioannou, J. A. Clark, T. Fischer, and M. Oertel, "Identifying a first-order phase transition in neutron star mergers through gravitational waves," *Phys. Rev. Lett.*, vol. 122, no. 6, p. 061102, 2019.

[120] M. G. Alford, K. Rajagopal, and F. Wilczek, "QCD at finite baryon density: Nucleon droplets and color superconductivity," *Phys. Lett. B*, vol. 422, pp. 247–256, 1998.

[121] M. G. Alford, A. Schmitt, K. Rajagopal, and T. Schäfer, "Color superconductivity in dense quark matter," *Rev. Mod. Phys.*, vol. 80, pp. 1455–1515, 2008.

[122] O. Scavenius, A. Mocsy, I. N. Mishustin, and D. H. Rischke, "Chiral phase transition within effective models with constituent quarks," *Phys. Rev. C*, vol. 64, p. 045202, 2001.

[123] M. Creutz, "Confinement and the Critical Dimensionality of Space-Time," *Phys. Rev. Lett.*, vol. 43, pp. 553–556, 1979. [Erratum: Phys.Rev.Lett. 43, 890 (1979)].

[124] M. Creutz, "Monte Carlo Study of Quantized SU(2) Gauge Theory," *Phys. Rev. D*, vol. 21, pp. 2308–2315, 1980.

[125] M. Laine and A. Vuorinen, *Basics of Thermal Field Theory*, vol. 925. Springer, 2016.

[126] R. Kara, *The QCD crossover at small chemical potential.* 2020.

[127] C. Hoelbling, "Lattice QCD: concepts, techniques and some results," *Acta Phys. Polon. B*, vol. 45, no. 12, p. 2143, 2014.

[128] O. Philipsen, "The QCD equation of state from the lattice," *Prog. Part. Nucl. Phys.*, vol. 70, pp. 55–107, 2013.

[129] K. Symanzik, "Continuum Limit and Improved Action in Lattice Theories. 1. Principles and φ^4 Theory," *Nucl. Phys. B*, vol. 226, pp. 187–204, 1983.

[130] M. Luscher and P. Weisz, "Computation of the Action for On-Shell Improved Lattice Gauge Theories at Weak Coupling," *Phys. Lett. B*, vol. 158, pp. 250–254, 1985.

[131] H. B. Nielsen and M. Ninomiya, "Absence of Neutrinos on a Lattice. 1. Proof by Homotopy Theory," *Nucl. Phys. B*, vol. 185, p. 20, 1981. [Erratum: Nucl.Phys.B 195, 541 (1982)].

[132] H. B. Nielsen and M. Ninomiya, "Absence of Neutrinos on a Lattice. 2. Intuitive Topological Proof," *Nucl. Phys. B*, vol. 193, pp. 173–194, 1981.

[133] H. B. Nielsen and M. Ninomiya, "No Go Theorem for Regularizing Chiral Fermions," *Phys. Lett. B*, vol. 105, pp. 219–223, 1981.

[134] A. Bazavov *et al.*, "Nonperturbative QCD Simulations with 2+1 Flavors of Improved Staggered Quarks," *Rev. Mod. Phys.*, vol. 82, pp. 1349–1417, 2010.

[135] J. B. Kogut and L. Susskind, "Hamiltonian Formulation of Wilson's Lattice Gauge Theories," *Phys. Rev. D*, vol. 11, pp. 395–408, 1975.

[136] H. J. Rothe, *Lattice Gauge Theories : An Introduction (Fourth Edition)*, vol. 43. World Scientific Publishing Company, 2012.

[137] S. R. Sharpe, "Rooted staggered fermions: Good, bad or ugly?," *PoS*, vol. LAT2006, p. 022, 2006.

[138] S. Borsanyi, S. Durr, Z. Fodor, C. Hoelbling, S. D. Katz, S. Krieg, D. Nogradi, K. K. Szabo, B. C. Toth, and N. Trombitas, "QCD thermodynamics with continuum extrapolated Wilson fermions I," *JHEP*, vol. 08, p. 126, 2012.

[139] S. Borsanyi, S. Durr, Z. Fodor, C. Holbling, S. D. Katz, S. Krieg, D. Nogradi, K. K. Szabo, B. C. Toth, and N. Trombitas, "QCD thermodynamics with continuum extrapolated Wilson fermions II," *Phys. Rev. D*, vol. 92, no. 1, p. 014505, 2015.

[140] Y. Aoki, S. Borsanyi, S. Durr, Z. Fodor, S. D. Katz, S. Krieg, and K. K. Szabo, "The QCD transition temperature: results with physical masses in the continuum limit II.," *JHEP*, vol. 06, p. 088, 2009.

[141] S. Borsanyi, G. Endrodi, Z. Fodor, A. Jakovac, S. D. Katz, S. Krieg, C. Ratti, and K. K. Szabo, "The QCD equation of state with dynamical quarks," *JHEP*, vol. 11, p. 077, 2010.

[142] C. Morningstar and M. J. Peardon, "Analytic smearing of SU(3) link variables in lattice QCD," *Phys. Rev. D*, vol. 69, p. 054501, 2004.

[143] S. Borsányi, Z. Fodor, J. N. Guenther, R. Kara, S. D. Katz, P. Parotto, A. Pásztor, C. Ratti, and K. K. Szabó, "Lattice QCD equation of state at finite chemical potential from an alternative expansion scheme," *Phys. Rev. Lett.*, vol. 126, no. 23, p. 232001, 2021.

[144] S. Borsanyi, J. N. Guenther, R. Kara, Z. Fodor, P. Parotto, A. Pasztor, C. Ratti, and K. K. Szabo, "Resummed lattice QCD equation of state at finite baryon density: Strangeness neutrality and beyond," *Phys. Rev. D*, vol. 105, no. 11, p. 114504, 2022.

[145] M. Albanese *et al.*, "Glueball Masses and String Tension in Lattice QCD," *Phys. Lett. B*, vol. 192, pp. 163–169, 1987.

[146] A. Hasenfratz and F. Knechtli, "Flavor symmetry and the static potential with hypercubic blocking," *Phys. Rev. D*, vol. 64, p. 034504, 2001.

[147] S. Capitani, S. Durr, and C. Hoelbling, "Rationale for UV-filtered clover fermions," *JHEP*, vol. 11, p. 028, 2006.

[148] S. Borsányi, Z. Fodor, J. N. Guenther, S. D. Katz, P. Parotto, A. Pásztor, D. Pesznyák, K. K. Szabó, and C. H. Wong, "Continuum extrapolated high order baryon fluctuations," 12 2023.

[149] E. Follana, Q. Mason, C. Davies, K. Hornbostel, G. P. Lepage, J. Shigemitsu, H. Trottier, and K. Wong, "Highly improved staggered quarks on the lattice, with applications to charm physics," *Phys. Rev. D*, vol. 75, p. 054502, 2007.

[150] P. de Forcrand *et al.*, "Renormalization group flow of SU(3) gauge theory," 6 1998.

[151] M. Lüscher, "Properties and uses of the Wilson flow in lattice QCD," *JHEP*, vol. 08, p. 071, 2010. [Erratum: JHEP 03, 092 (2014)].

[152] S. Borsányi, S. Dürr, Z. Fodor, C. Hoelbling, S. D. Katz, S. Krieg, T. Kurth, L. Lellouch, T. Lippert, and C. McNeile, "High-precision scale setting in lattice QCD," *JHEP*, vol. 09, p. 010, 2012.

[153] S. Borsanyi *et al.*, "Leading hadronic contribution to the muon magnetic moment from lattice QCD," *Nature*, vol. 593, no. 7857, pp. 51–55, 2021.

[154] P. Hasenfratz and F. Karsch, "Chemical Potential on the Lattice," *Phys. Lett. B*, vol. 125, pp. 308–310, 1983.

[155] R. Bellwied, S. Borsanyi, Z. Fodor, S. D. Katz, A. Pasztor, C. Ratti, and K. K. Szabo, "Fluctuations and correlations in high temperature QCD," *Phys. Rev. D*, vol. 92, no. 11, p. 114505, 2015.

[156] R. Bellwied, S. Borsanyi, Z. Fodor, J. Günther, S. D. Katz, C. Ratti, and K. K. Szabo, "The QCD phase diagram from analytic continuation," *Phys. Lett. B*, vol. 751, pp. 559–564, 2015.

[157] C. R. Allton, S. Ejiri, S. J. Hands, O. Kaczmarek, F. Karsch, E. Laermann, C. Schmidt, and L. Scorzato, "The QCD thermal phase transition in the presence of a small chemical potential," *Phys. Rev. D*, vol. 66, p. 074507, 2002.

[158] A. Bazavov *et al.*, "Chiral crossover in QCD at zero and non-zero chemical potentials," *Phys. Lett. B*, vol. 795, pp. 15–21, 2019.

[159] Z. Fodor, S. D. Katz, and C. Schmidt, "The Density of states method at non-zero chemical potential," *JHEP*, vol. 03, p. 121, 2007.

[160] A. Alexandru, G. Basar, and P. Bedaque, "Monte Carlo algorithm for simulating fermions on Lefschetz thimbles," *Phys. Rev. D*, vol. 93, no. 1, p. 014504, 2016.

[161] D. Sexty, "Simulating full QCD at nonzero density using the complex Langevin equation," *Phys. Lett. B*, vol. 729, pp. 108–111, 2014.

[162] E. Seiler, D. Sexty, and I.-O. Stamatescu, "Complex Langevin: Correctness criteria, boundary terms, and spectrum," *Phys. Rev. D*, vol. 109, no. 1, p. 014509, 2024.

[163] G. Aarts *et al.*, "Phase Transitions in Particle Physics: Results and Perspectives from Lattice Quantum Chromo-Dynamics," *Prog. Part. Nucl. Phys.*, vol. 133, p. 104070, 2023.

[164] A. Pasztor, "The QCD phase diagram at finite temperature and density - a lattice perspective," *PoS*, vol. LATTICE2023, p. 108, 2024.

[165] F. Knechtli, M. Günther, and M. Peardon, *Lattice Quantum Chromodynamics: Practical Essentials*. SpringerBriefs in Physics, Springer Netherlands, 2016.

[166] N. Cabibbo and E. Marinari, "A New Method for Updating SU(N) Matrices in Computer Simulations of Gauge Theories," *Phys. Lett. B*, vol. 119, pp. 387–390, 1982.

[167] A. D. Kennedy and B. J. Pendleton, "Improved Heat Bath Method for Monte Carlo Calculations in Lattice Gauge Theories," *Phys. Lett. B*, vol. 156, pp. 393–399, 1985.

[168] S. Borsanyi, Z. Fodor, D. A. Godzieba, R. Kara, P. Parotto, D. Sexty, and R. Vig, "Topological features of the deconfinement transition," *Phys. Rev. D*, vol. 107, no. 5, p. 054514, 2023.

[169] E. Marinari and G. Parisi, "Simulated tempering: A New Monte Carlo scheme," *EPL*, vol. 19, pp. 451–458, 1992.

[170] K. Hukushima and K. Nemoto, "Exchange monte carlo method and application to spin glass simulations," *Journal of the Physical Society of Japan*, vol. 65, no. 6, pp. 1604–1608, 1996.

[171] R. H. Swendsen and J.-S. Wang, "Replica monte carlo simulation of spin-glasses," *Phys. Rev. Lett.*, vol. 57, pp. 2607–2609, Nov 1986.

[172] B. Joo, B. Pendleton, S. M. Pickles, Z. Sroczynski, A. C. Irving, and J. C. Sexton, "Parallel tempering in lattice QCD with O(a)-improved Wilson fermions," *Phys. Rev. D*, vol. 59, p. 114501, 1999.

[173] E.-M. Ilgenfritz, W. Kerler, M. Muller-Preussker, and H. Stuben, "Parallel tempering in full QCD with Wilson fermions," *Phys. Rev. D*, vol. 65, p. 094506, 2002.

[174] S. Borsanyi and D. Sexty, "Topological susceptibility of pure gauge theory using Density of States," *Phys. Lett. B*, vol. 815, p. 136148, 2021.

[175] Z. Fodor and S. D. Katz, "Critical point of QCD at finite T and mu, lattice results for physical quark masses," *JHEP*, vol. 04, p. 050, 2004.

[176] M. E. J. Newman and G. T. Barkema, *Monte Carlo methods in statistical physics*. Oxford: Clarendon Press, 1999.

[177] A. M. Ferrenberg and R. H. Swendsen, "New monte carlo technique for studying phase transitions," *Phys. Rev. Lett.*, vol. 61, pp. 2635–2638, Dec 1988.

[178] A. M. Ferrenberg and R. H. Swendsen, "Optimized monte carlo data analysis," *Phys. Rev. Lett.*, vol. 63, pp. 1195–1198, Sep 1989.

[179] M. Schmelling, "Averaging correlated data," *Phys. Scripta*, vol. 51, pp. 676–679, 1995.

[180] S. Duane, A. D. Kennedy, B. J. Pendleton, and D. Roweth, "Hybrid Monte Carlo," *Phys. Lett. B*, vol. 195, pp. 216–222, 1987.

[181] A. D. Kennedy, I. Horvath, and S. Sint, "A New exact method for dynamical fermion computations with nonlocal actions," *Nucl. Phys. B Proc. Suppl.*, vol. 73, pp. 834–836, 1999.

[182] M. Luscher, "Computational Strategies in Lattice QCD," in *Les Houches Summer School: Session 93: Modern perspectives in lattice QCD: Quantum field theory and high performance computing*, pp. 331–399, 2 2010.

[183] M. A. Clark, "The Rational Hybrid Monte Carlo Algorithm," *PoS*, vol. LAT2006, p. 004, 2006.

[184] A. Frommer, B. Nockel, S. Gusken, T. Lippert, and K. Schilling, "Many masses on one stroke: Economic computation of quark propagators," *Int. J. Mod. Phys. C*, vol. 6, pp. 627–638, 1995.

[185] M. A. Clark and A. D. Kennedy, "The RHMC algorithm for two flavors of dynamical staggered fermions," *Nucl. Phys. B Proc. Suppl.*, vol. 129, pp. 850–852, 2004.

[186] M. A. Clark and A. D. Kennedy, "Accelerating dynamical fermion computations using the rational hybrid Monte Carlo (RHMC) algorithm with multiple pseudofermion fields," *Phys. Rev. Lett.*, vol. 98, p. 051601, 2007.

[187] M. Fromm, J. Langelage, S. Lottini, and O. Philipsen, "The QCD deconfinement transition for heavy quarks and all baryon chemical potentials," *JHEP*, vol. 01, p. 042, 2012.

[188] G. Aarts, F. Attanasio, B. Jäger, and D. Sexty, "The QCD phase diagram in the limit of heavy quarks using complex Langevin dynamics," *JHEP*, vol. 09, p. 087, 2016.

[189] S. Aoki, G. Boyd, R. Burkhalter, S. Ejiri, M. Fukugita, S. Hashimoto, Y. Iwasaki, K. Kanaya, T. Kaneko, Y. Kuramashi, K. Nagai, M. Okawa, H. P. Shanahan, A. Ukawa, and T. Yoshié, "Quenched light hadron spectrum," *Phys. Rev. Lett.*, vol. 84, pp. 238–241, Jan 2000.

[190] B. Beinlich, F. Karsch, E. Laermann, and A. Peikert, "String tension and thermodynamics with tree level and tadpole improved actions," *Eur. Phys. J. C*, vol. 6, pp. 133–140, 1999.

[191] S. Borsanyi, G. Endrodi, Z. Fodor, S. D. Katz, and K. K. Szabo, "Precision SU(3) lattice thermodynamics for a large temperature range," *JHEP*, vol. 07, p. 056, 2012.

[192] R. Kara, S. Borsanyi, Z. Fodor, D. A. Godzieba, P. Parotto, and D. Sexty, "Parallel tempering algorithm applied to the deconfinement transition of quenched QCD," *PoS*, vol. LATTICE2022, p. 178, 2023.

[193] Z. Fodor, K. Holland, J. Kuti, S. Mondal, D. Nogradi, and C. H. Wong, "The lattice gradient flow at tree-level and its improvement," *JHEP*, vol. 09, p. 018, 2014.

[194] P. Petreczky, H.-P. Schadler, and S. Sharma, "The topological susceptibility in finite temperature QCD and axion cosmology," *Phys. Lett. B*, vol. 762, pp. 498–505, 2016.

[195] S. Borsanyi *et al.*, "Calculation of the axion mass based on high-temperature lattice quantum chromodynamics," *Nature*, vol. 539, no. 7627, pp. 69–71, 2016.

[196] M. D'Elia and F. Negro, "Phase diagram of Yang-Mills theories in the presence of a θ term," *Phys. Rev. D*, vol. 88, no. 3, p. 034503, 2013.

[197] H. Panagopoulos and E. Vicari, "The 4D SU(3) gauge theory with an imaginary θ term," *JHEP*, vol. 11, p. 119, 2011.

[198] F. Rennecke, "Higher topological charge and the QCD vacuum," *Phys. Rev. Res.*, vol. 2, no. 3, p. 033359, 2020.

[199] C. Bonanno, M. D'Elia, and L. Verzichelli, "The θ-dependence of the SU(N) critical temperature at large N," *JHEP*, vol. 02, p. 156, 2024.

[200] R. A. Vig, S. Borsányi, Z. Fodor, D. Godzieba, R. Kara, P. Parotto, and D. Sexty, "Topological features of the deconfinement transition in the SU(3) Yang-Mills theory," *PoS*, vol. LATTICE2022, p. 194, 2023.

[201] G. D. Moore, "Improved Hamiltonian for Minkowski Yang-Mills theory," *Nucl. Phys. B*, vol. 480, pp. 689–728, 1996.

[202] P. de Forcrand, M. Garcia Perez, and I.-O. Stamatescu, "Topology of the SU(2) vacuum: A Lattice study using improved cooling," *Nucl. Phys. B*, vol. 499, pp. 409–449, 1997.

[203] S. O. Bilson-Thompson, D. B. Leinweber, and A. G. Williams, "Highly improved lattice field strength tensor," *Annals Phys.*, vol. 304, pp. 1–21, 2003.

[204] S. Durr, Z. Fodor, C. Hoelbling, and T. Kurth, "Precision study of the SU(3) topological susceptibility in the continuum," *JHEP*, vol. 04, p. 055, 2007.

[205] R. Sommer, "Scale setting in lattice QCD," *PoS*, vol. LATTICE2013, p. 015, 2014.

[206] M. D'Elia and F. Negro, "θ dependence of the deconfinement temperature in Yang-Mills theories," *Phys. Rev. Lett.*, vol. 109, p. 072001, 2012.

[207] P. Romatschke, "New Developments in Relativistic Viscous Hydrodynamics," *Int. J. Mod. Phys. E*, vol. 19, pp. 1–53, 2010.

[208] S. Pratt, E. Sangaline, P. Sorensen, and H. Wang, "Constraining the Eq. of State of Super-Hadronic Matter from Heavy-Ion Collisions," *Phys. Rev. Lett.*, vol. 114, p. 202301, 2015.

[209] S. Borsanyi, Z. Fodor, C. Hoelbling, S. D. Katz, S. Krieg, and K. K. Szabo, "Full result for the QCD equation of state with 2+1 flavors," *Phys. Lett. B*, vol. 730, pp. 99–104, 2014.

[210] A. Bazavov *et al.*, "Equation of state in (2+1)-flavor QCD," *Phys. Rev. D*, vol. 90, p. 094503, 2014.

[211] G. S. Bali, F. Bruckmann, G. Endrődi, S. D. Katz, and A. Schäfer, "The QCD equation of state in background magnetic fields," *JHEP*, vol. 08, p. 177, 2014.

[212] S. Borsanyi, G. Endrodi, Z. Fodor, S. D. Katz, S. Krieg, C. Ratti, and K. K. Szabo, "QCD equation of state at nonzero chemical potential: continuum results with physical quark masses at order mu^2," *JHEP*, vol. 08, p. 053, 2012.

[213] A. Bazavov *et al.*, "The QCD Equation of State to $\mathcal{O}(\mu_B^6)$ from Lattice QCD," *Phys. Rev. D*, vol. 95, no. 5, p. 054504, 2017.

[214] P. Parotto, S. Borsányi, Z. Fodor, J. N. Guenther, R. Kara, S. D. Katz, A. Pásztor, C. Ratti, and K. K. Szabó, "Finite chemical potential equation of state for QCD from an alternative expansion scheme," *EPJ Web Conf.*, vol. 259, p. 10015, 2022.

[215] P. Parotto, S. Borsanyi, Z. Fodor, J. N. Guenther, R. Kara, S. D. Katz, A. Pasztor, C. Ratti, and K. K. Szabo, "Equation of state of QCD at finite chemical potential from an alternative expansion scheme," *PoS*, vol. LATTICE2021, p. 460, 2022.

[216] R. Bellwied, S. Borsanyi, Z. Fodor, J. N. Guenther, J. Noronha-Hostler, P. Parotto, A. Pasztor, C. Ratti, and J. M. Stafford, "Off-diagonal correlators of conserved charges from lattice QCD and how to relate them to experiment," *Phys. Rev. D*, vol. 101, no. 3, p. 034506, 2020.

[217] J. Noronha-Hostler, P. Parotto, C. Ratti, and J. M. Stafford, "Lattice-based equation of state at finite baryon number, electric charge and strangeness chemical potentials," *Phys. Rev. C*, vol. 100, no. 6, p. 064910, 2019.

[218] S. Borsanyi, Z. Fodor, J. N. Guenther, S. K. Katz, K. K. Szabo, A. Pasztor, I. Portillo, and C. Ratti, "Higher order fluctuations and correlations of conserved charges from lattice QCD," *JHEP*, vol. 10, p. 205, 2018.

[219] J. N. Guenther *et al.*, "Resummed lattice QCD equation of state at finite baryon density: strangeness neutrality and beyond," *PoS*, vol. LATTICE2022, p. 150, 2023.

[220] P. Parotto, S. Borsányi, Z. Fodor, J. N. Guenther, R. Kara, A. Pásztor, C. Ratti, and K. K. Szabó, "Lattice QCD equation of state at finite chemical potential from an alternative resummation: Strangeness neutrality and beyond," *EPJ Web Conf.*, vol. 276, p. 01014, 2023.

[221] J. I. Kapusta, *Finite Temperature Field Theory*. Cambridge Monographs on Mathematical Physics, Cambridge: Cambridge University Press, 1989.

[222] Z. Fodor and S. D. Katz, "A New method to study lattice QCD at finite temperature and chemical potential," *Phys. Lett. B*, vol. 534, pp. 87–92, 2002.

[223] S. Borsanyi, Z. Fodor, M. Giordano, J. N. Guenther, S. D. Katz, A. Pasztor, and C. H. Wong, "Equation of state of a hot-and-dense quark gluon plasma: Lattice simulations at real μB vs extrapolations," *Phys. Rev. D*, vol. 107, no. 9, p. L091503, 2023.

[224] S. Borsanyi, Z. Fodor, M. Giordano, S. D. Katz, D. Nogradi, A. Pasztor, and C. H. Wong, "Lattice simulations of the QCD chiral transition at real baryon density," *Phys. Rev. D*, vol. 105, no. 5, p. L051506, 2022.

[225] J. N. Guenther, R. Bellwied, S. Borsanyi, Z. Fodor, S. D. Katz, A. Pasztor, C. Ratti, and K. K. Szabó, "The QCD equation of state at finite density from analytical continuation," *Nucl. Phys. A*, vol. 967, pp. 720–723, 2017.

[226] X. An, G. Basar, M. Stephanov, and H.-U. Yee, "Non-Gaussian fluctuation dynamics in relativistic fluids," *Phys. Rev. C*, vol. 108, no. 3, p. 034910, 2023.

[227] S. Borsányi, Z. Fodor, J. N. Guenther, R. Kara, P. Parotto, A. Pásztor, and C. H. Wong, "Finite volume effects near the chiral crossover," 1 2024.

[228] S. Borsanyi, Z. Fodor, J. N. Guenther, R. Kara, P. Parotto, A. Pasztor, L. Pirelli, and C. H. Wong, "Chiral and deconfinement properties of the QCD crossover have a different volume and baryochemical potential dependence," 5 2024.

[229] P. Adhikari and B. C. Tiburzi, "QCD thermodynamics and neutral pion in a uniform magnetic field: Finite volume effects," *Phys. Rev. D*, vol. 107, no. 9, p. 094504, 2023.

[230] S. Borsanyi, Z. Fodor, C. Hoelbling, S. D. Katz, S. Krieg, C. Ratti, and K. K. Szabo, "Is there still any T_c mystery in lattice QCD? Results with physical masses in the continuum limit III," *JHEP*, vol. 09, p. 073, 2010.

[231] C. Bonati, M. D'Elia, M. Mariti, M. Mesiti, F. Negro, and F. Sanfilippo, "Curvature of the chiral pseudocritical line in QCD," *Phys. Rev. D*, vol. 90, no. 11, p. 114025, 2014.

[232] S. Borsanyi, Z. Fodor, M. Giordano, J. N. Guenther, S. D. Katz, A. Pasztor, and C. H. Wong, "Can rooted staggered fermions describe nonzero baryon density at low temperatures?," *Phys. Rev. D*, vol. 109, no. 5, p. 054509, 2024.

[233] L. H. Karsten, "Lattice Fermions in Euclidean Space-time," *Phys. Lett. B*, vol. 104, pp. 315–319, 1981.

[234] F. Wilczek, "Lattice fermions," *Phys. Rev. Lett.*, vol. 59, pp. 2397–2400, Nov 1987.

[235] R. A. Vig, S. Borsanyi, Z. Fodor, D. Godzieba, P. Parotto, and C. H. Wong, "First dynamical simulations with minimally doubled fermions," in *40th International Symposium on Lattice Field Theory*, 1 2024.

[236] D. A. Godzieba, S. Borsanyi, Z. Fodor, P. Parotto, R. A. Vig, and C. H. Wong, "Renormalization of Karsten-Wilczek Quarks on a Staggered Background," 1 2024.

[237] M. D'Elia, L. Maio, F. Sanfilippo, and A. Stanzione, "Phase diagram of QCD in a magnetic background," *Phys. Rev. D*, vol. 105, no. 3, p. 034511, 2022.

Acknowledgements

First, I want to thank my advisor Szabolcs Borsányi for his full and steady trust in my capabilities and the opportunity to contribute to such fascinating projects. His enthusiasm, positive and energetic attitude to tackle fundamental problems has been and will be very inspiring and exemplary for me.

I am very grateful to Paolo Parotto for his great support and friendship over the past years. I have learned a lot from you; personally, academically and through your clever advice on how to become a professional.

I want to thank all the members of the Wuppertal-Budapest collaboration for providing such a smoothly running working group. I also enjoyed to work with Dénes Sexty who came up with clever ideas to improve numerical stability of the correlated multiple-histogram program.

Special thanks to Saskia Faulmann and Paolo Parotto for your comments on this manuscript.

Thanks to my friends and family for their steady support over the last years. I thank my long-term friend from the early school days Daniel Wanken for our frequent and controversial discussions about industry, politics and especially our personal growth.

Finally, I thank my girlfriend Hannah. I cannot appreciate you enough; for your patience, your inspiring happiness and being my help in my darkest moments.